2023

Rankine Cycle Investigation on Meeting Power and Thermal Requirements of High-Speed Aircraft

Jacob J. Spark
Wright State University

RANKINE CYCLE INVESTIGATION ON MEETING POWER AND THERMAL REQUIRMENTS OF HIGH-SPEED AIRCRAFT

A thesis submitted in partial fulfillment of the
requirements for the degree of
Master of Science in Mechanical Engineering

By:

JACOB J. SPARK
B.S.M.E., Wright State University, 2021

2023
Wright State University

WRIGHT STATE UNIVERSITY

COLLEGE OF GRADUATE PROGRAMS AND HONORS STUDIES

December 9, 2022

I HEREBY RECOMMEND THAT THE THESIS PREPARED UNDER MY SUPERVISION BY Jacob J. Spark ENTITLED Rankine Cycle Investigation on Meeting Power and Thermal Requirements of High-Speed Aircraft BE ACCEPTED IN PARTIAL FULFILLMENT OF THE REQUIREMENTS FOR THE DEGREE OF Master of Science in Mechanical Engineering.

_____

Mitch Wolff, Ph.D.
Thesis Director

_____

Raghavan Srinivasan, Ph.D., P.E.
Chair, Mechanical and Materials
Engineering Department

Committee on Final Examination:

_____

Abdeel Roman, Ph.D.

_____

José Camberos, Ph.D., P.E.

_____

Mitch Wolff, Ph.D.

_____

Shu Schiller, Ph.D.
Interim Dean
College of Graduate Programs & Honor Studies

ABSTRACT

Spark, Jacob J., M.S.M.E., Department of Mechanical and Materials Engineering, Wright State University, 2023. Rankine Cycle Investigation on Meeting Power and Thermal Requirements of High-Speed Aircraft.

This work is investigating a dual mode Rankine cycle for aircraft applications, specifically meeting vehicle thermal and power requirements. This multiconfigurational approach allows the Thermal Management System (TMS) to be controlled based on aircraft needs. In this design, waste heat is removed from critical areas of the aircraft (e.g., propulsion, structure, subsystems) using the fuel as a heat sink. Hot fuel is then forced through a heat exchanger actively boiling water. The vapor byproduct is fed to a turbine coupled to a generator, providing power. The low-pressure steam is then condensed using cold fuel drawn from its tank; however, when additional cooling is needed, this steam is exhausted instead.

Methods used are a blend of empirical and theoretical studies where a small-scale experimental rig is used to validate component models. MATLAB/Simulink software is used to capture their individual performance within the steady state and transient reschemes. With model fidelity established, scaling is used to assess the feasibility of the dual mode Rankine cycle. Using steady state results accuracy of modeled components was assessed based on root-mean-squared-error (RMSE). The single-phase heat exchanger showed the least error at 0.8%. Tube-in-tube and corrugated plate evaporators resulted in an RMSE of 14.2% and 1.0%, respectively. Evaporator transients were also analyzed, and predicted time constants led the experimental results showing a mean error of 13.8%, for the tube-in-tube evaporator and 82% for the corrugated plate evaporator. The scroll expanders performance represented the power capabilities of the system. Model results showed a RMSE of 10.1% and second law efficiency RMSE of 0.15%. With increased confidence in component models, a vehicle scaling was performed predicting system performance during two operating modes. During high-heat mode, thermal efficiency was 6.51% and second law efficiencies was 63.7%. During reduced-heat mode, thermal efficiency was 8.92% and second law efficiencies was 68.8%.

DISCLAMIER

The views expressed are those of the authors and do not reflect the official guidance or position of the United States Government, the Department of Defense or of the United States Air Force. Statement from DoD: The Appearance of external hyperlinks does not constitute endorsement by the United States Department of Defense (DoD) of the linked websites, of the information, products, or services contained therein. The DoD does not exercise any editorial, security, or other control over the information you may find at these locations.

Table of Contents

ABSTRACT iii

DISCLAMIER iv

List of Figures vii

LIST OF TABLES x

ACKNOWLEDGEMENTS xiii

1. Introduction 1

1.1 Motivation 1

1.2 Problem 1

1.3 Approach 1

1.4 Thesis Organization 2

2. Background 3

2.1 Material Development: 3

2.2 Propulsion Design: 4

2.3 Thermal Management System: 8

2.3.1 Heat Sink 8

2.3.2 Insulative 8

2.3.3 Ablative 9

2.3.3 Active TMS 9

2.4 Power Generation: 21

3. Methodology 24

3.1 Innovative Solution 24

3.1.1 Rankine Cycle 24

3.1.2 Dual-Mode Rankine Cycle for Aircraft Applications 25

3.2 Experimental System 26

3.2.1 System Description 27

IV. Model Development 34

4.1 Heat Exchanger Modeling Strategies 34

4.2 Oil Cooler Modeling 41

4.3 Evaporator Steady State Analysis 48

4.3.1 Tube-in-Tube 48

4.3.2 Corrugated-Plate Analysis 60
4.4 Evaporator Transient Analysis 69
4.3 Scroll Modeling 76
4.3.1 Scroll Pressure Mapping 78
4.3.2 Isentropic Efficiency Mapping 81
4.3.3 Mechanical Efficiency Mapping 85
V. Vehicle Level Modeling 87
VI. Conclusion 98
References 100
Appendix A 104
Appendix B 105
Appendix C 109
Appendix D 109

List of Figures

FIGURE 1: MATERIAL PROPERTIES OF VARIOUS AEROSPACE STRUCTURAL MATERIALS [1] 3
FIGURE 2: X-51 AND BOOST ASSIST ROCKET SHOWING EXTERIOR MATERIALS [2] 4
FIGURE 3: SPECIFIC ENGINE IMPULSE FOR VARIOUS PROPULSION ENGINES AT VARYING MACH NUMBER WITH TWO DIFFERENT FUEL CONFIGURATIONS [26]. 5
FIGURE 4: CONFIGURATION MODES OF A TURBINE-BASED COMBINED CYCLE ENGINE, WITH $\mathrm{MACH} < 4$ **(A)** AND $\mathrm{MACH} > 4$ **(B)** [32]. 6
FIGURE 5: **(A)** SHOCK TRAINS WITHIN THE INLET AND ISOLATOR OF A RAMJET AND **(B)** THROUGHOUT THE ENTIRE SCRAMJET [2]. 7
FIGURE 6: BASIC PASSIVE TMS CONCEPTS [1] 8
FIGURE 7: STRUCTURAL INTERIOR OF ABLATIVE COATING SHOWING THE ENDOTHERMIC ABLATIVE PROCESS DURING HIGH THERMAL HEATING, ADAPTED FROM RICCIO [25]. 9
FIGURE 8: BASIC CONCEPTS FOR ACTIVE TMS [1]. 10
FIGURE 9: STANTON NUMBERS FOR COMPRESSIBLE FLOW OVER A FLAT PLATE [48]. 11
FIGURE 10: NORMALIZED TEMPERATURE DISTRIBUTION TAKEN THROUGH THE CENTERLINE OF A COOLING JET SHOWING THE INJECTION OF COOLANT INTO THE BOUNDARY LAYER [28]. 12
FIGURE 11: PROGRESSION OF THERMAL CAPABILITIES SHOWING TEMPERATURE LIMITS OF STRUCTURAL MATERIAL (NI-BASED SUPERALLOY) AND THERMAL BASED COATINGS (TBC) WITH ENHANCED CAPABILITY FILM COOLING OFFERS [33]. 13
FIGURE 12: GENERAL RECTANGULAR SCRAMJET COOLING CHANNEL [4]. 14
FIGURE 13: PROGRESSION OF SPECIFIC ENTHALPY OF JP-7 WITH INCREASING TEMPERATURE [6]. 15
FIGURE 14: COOLANT REQUIREMENTS FOR A HYDROGEN POWERED SCRAMJET ENGINE [42]. 17
FIGURE 15: PROGRESSION OF THE OPTIMAL COOLANT FLOW RATE FOR NICKEL 210 CHANNEL-FIN AND PIN-FIN CONCEPTS UTILIZING AN INLET PRESSURE OF 3000 PSI [3]. 18
FIGURE 16: COOLANT FLOW ROUTING SCHEME FOR THREE DIFFERENT CONFIGURATIONS USING A SET INLET PRESSURE AND TEMPERATURE OF $3000\ \mathrm{PSI}\ 100°\mathrm{R}$ AND CONSTANT HEATING RATES FOR THE INLET, COMBUSTOR, AND NOZZLE [3]. 19
FIGURE 17: TMS SCHEME FOR A SCRAMJET ENGINE INCORPORATING REGENERATIVE COOLING AND FILM COOLING [4]. 20
FIGURE 18: WALL TEMPERATURE WITHIN A SCRAMJET ENGINE USING A BULK FLOW TEMPERATURE OF $1930\ \mathrm{K}$ [4]. 20
FIGURE 19: COMBINED TMS AND POWER GENERATION DIAGRAM UTILIZING EXPANDED THERMALLY CRACKED FUEL [5]. 21
FIGURE 20: INFLUENCE OF TEMPERATURE AND MASS FLOW RATE ON POTENTIAL POWER GENERATION OF RP-3, REFERENCING ISENTROPIC ENTHALPY [5]. 22
FIGURE 21: RANKINE CYCLE COMPONENT DIAGRAM (A) AND T-S DIAGRAM, (B) REPRESENTING THE IDEALIZED FLUID STATES USED TO DEFINE ACTUAL SYSTEM PERFORMANCE [6]. 24
FIGURE 22: THERMAL MANAGEMENT DIAGRAM, INCORPORATING THE DUAL MODE RANKINE CYCLE WHERE FUEL IS USED AS A HEAT SINK BEFORE BEING BURNED IN THE COMBUSTOR, ADAPTED FROM [9]. 25
FIGURE 23: DIAGRAM REPRESENTING RIG COMPONENTS AND FLUID FLOW PROCESSES, ADAPTED FROM [9]. 27

FIGURE 24: EXPERIMENTAL RIG REPLICATING THE OPEN CYCLE OF THE RANKINE CYCLE SYSTEM. 28
FIGURE 25: ILLUSTRATION OF SCROLL EXPANDERS INNER GEOMETRY [29]. 30
FIGURE 26: DIAGRAM SHOWING THE ORBITAL MOTION OF THE SCROLL EXPANDER TRACED BY A VIRTUAL CIRCLE [30]. 30
FIGURE 27: EXPERIMENTAL SYSTEM SHOWING THE NEWLY INSTALLED EVAPORATOR AND OIL COOLER. 32
FIGURE 28: DISCRETIZED HEAT EXCHANGER GEOMETRY FOR THE FINITE CONTROL VOLUME (A) AND MOVING BOUNDARY (B) MODELS INCLUDING PARAMETERS ASSOCIATED WITH MASS AND ENERGY CONSERVATION [8]. 35
FIGURE 29: OVERALL HEAT TRANSFER COEFFICIENT FOR DIFFERENT HEAT EXCHANGER DESIGNS [11]. 38
FIGURE 30: HEAT EXCHANGER NODES, REFERENCING THE LOCATION OF THE WATER SIDE PHASE BOUNDARY WHERE VARIATION IN HEAT TRANSFER EXIST [9] 39
FIGURE 31: AMHX GEOMETRY (A) AND CROSS-SECTION (B) 42
FIGURE 32: HEAT TRANSFER THROUGH A PIPE REFERENCING THE THERMAL RESISTANCE CONCEPT [11]. 43
FIGURE 33: VARIATIONS IN OIL SIDE HEATING THROUGH CHANGES IN FLOW RATE AND TEMPERATURE, PLOTTED AS A FUNCTION OF REYNOLDS NUMBER (A) AND DYNAMIC VISCOSITY (B). 45
FIGURE 34: CURVE FIT USED FOR OIL COOLER MODEL DEVELOPMENT. 46
FIGURE 35: SIMSCAPE OIL COOLER EVALUATION MODEL 47
FIGURE 36: PERFORMANCE ASSESSMENT OF THE MODELED OIL COOLER 48
FIGURE 37: GEOMETRY OF A MODEL AS-00528, TUBE-IN-TUBE HEAT EXCHANGER PRODUCED BY EXERGY LLC (UNITS IN INCHES) 49
FIGURE 38: NUMERICAL HEAT FLUX COMPARISON USING THE SIMULINK MB HEAT EXCHANGER MODEL OVERLAYED WITH EMPIRICAL RESULTS. 51
FIGURE 39: DIAGRAM OF HELICAL COILED TUBE (A) AND CROSS-SECTION SHOWING INDUCED SECONDARY FLOW (B) [11]. 52
FIGURE 40: HEATING COMPARISON FOR THE SUBCOOLED LAMINAR FLOW (A) AND TURBULENT SUPERHEATED VAPOR (B). 54
FIGURE 41: HEATING COMPARISON BETWEEN CAVALLINI AND ZECCHIN (1974) AND MATHUR (1976) CORRELATIONS WITH $G = 49.1$ KG/M2 S AND $Psat = 1$ ATM. 55
FIGURE 42: HEATING WITHIN THE TUBE-IN-TUBE OIL COOLER WITH VARIED MEAN OIL TEMPERATURE AND FLOW RATE FROM $32 \rightarrow 150°C$ AND $1 \rightarrow 7$ L/MIN, RESPECTIVELY. 57
FIGURE 43: HEATING COMPARISONS FOR THE EVAPORATOR ANNULUS USING TYPICAL SYSTEM OPERATIONS WITH $Toil = 80 \rightarrow 200$ °C AND $Goil = 323$ KG/M2/S. 58
FIGURE 44: PERFORMANCE ASSESSMENT OF THE TUBE-IN-TUBE EVAPORATOR MODEL 59
FIGURE 45: CORRUGATED PLATE HEAT TRANSFER CONCEPT [45]. 60
FIGURE 46: GEOMETRY OF A PLATE HEAT EXCHANGER WITH A SCALED CROSS SECTION [29]. 61
FIGURE 47: TRADITIONAL WILSON PLOT, ADAPTED FROM [20] 62
FIGURE 48: WILSON PLOT METHOD APPLIED TO OIL-SIDE OF THE CPHX. 64
FIGURE 49: TWO-PHASE HEATING WITHIN THE CP HX 67
FIGURE 50: SIMSCAPE MODEL SHOWING A SINGLE CELL OF THE FINITE VOLUME CPHX MODEL. 68
FIGURE 51: PERFORMANCE OF THE CORRUGATED PLATE EVAPORATOR MODEL 69
FIGURE 52: LOG-INCOMPLETE RESPONSE FROM A GENERIC DATA SET [44]. 71
FIGURE 53: GENERAL DATA SET WITH ERROR (A), AND INCOMPLETE RESPONSE WITH ERROR (B) [44]. 72

Figure 54: Log-Incomplete response from experimental and numerical results..... 72
Figure 55: TTHX model transient evaluation using a ramp response. 73
Figure 56: Comparative response of the TTHX by decreasing water flow rate. 74
Figure 57: Experimental and numerical response of the CPHX through an increase in water flow rate. 75
Figure 58: Experimental and numerical results through a decrease in water flow rate. 76
Figure 59: Simulink evaporator and scroll expander evaluation model. 77
Figure 60: Scroll working process flowchart. 77
Figure 61: Stodola's cone of steam weights showing property relation contours, adapted from [23]. 78
Figure 62: Stodola's ellipse showing relationships between fluid properties for a turbine [24]. 79
Figure 63: Proportionality constant, K determined for a range of scroll speeds. 80
Figure 64: Off design performance evaluation of the Stodola's ellipse relation 81
Figure 65: H-S Mollier diagram, comparing the isentropic process with the actual expansion. 82
Figure 66: Tabulated isentropic efficiencies for the scroll expander at various speeds. 83
Figure 67: Enthalpy diagram comparing the experimental and numerical results. 84
Figure 68: Mechanical efficiencies of the scroll expander (a) and predominate trends (b). 85
Figure 69: Scroll expander performance comparing numerical and empirical results. 86
Figure 70: Component diagram of the Rankine cycle system during closed configuration 87
Figure 71: Vehicle level model investigating system performance using scaled input parameters. 89
Figure 72: Response of the experimental system to an applied step input overlayed with the representative first-order transfer function..... 91
Figure 73: Evaporator inlet properties and temperature limits (a) and fuel flow rate and heating within the first cooling channel. 93
Figure 74: Evaporator inlet temperatures and thermal limits (a) water flow rates before and after modifications (b). 95
Figure 75: Scroll properties and power scaled requirements (a) and water flow rate (b) 96

List of Tables

Table 1: Theoretically derived Nusselt numbers for fully developed flow through a concentric annulus with one wall insulated and the other held at constant temperature [11]. 50
Table 2: Mapped isentropic efficiency as a function of pressure ratio and rotational speed..... 83
Table 3: Mapped mechanical efficiency as a function of pressure ratio and scroll speed..... 86
Table 4: High-speed aircraft relations comparing parameters between flight situations..... 88
Table 5: Input model parameters defined using scaled ratios from Table 4..... 90
Table 6: Transfer functions developed based on empirical data, Figure 72..... 92
Table 7: Isentropic and thermal efficiencies of the system using a vehicle scaled evaluation..... 97

Acronyms and Symbols

AFRL	=	Air Force Research Laboratory
FCV	=	Finite Control Volume
MB	=	Moving Boundary
NTU	=	Number of transfer units
ORC	=	Organic Rankine Cycle
RC	=	Regenerative Cooling
RCC	=	Recooling Cycle
TMS	=	Thermal Management System
TBCC	=	Turbine Based Combined Cycle
ΔP	=	Pressure difference
ΔT	=	Temperature difference
δ	=	Curvature ratio
ε	=	Heat exchanger effectiveness
η_{Carnot}	=	Carnot efficiency
η_{iso}	=	Isentropic efficiency
η_{mech}	=	Mechanical efficiency
θ	=	Normalized temperature profile
ϕ	=	Variable Parameter
ω	=	Rotational velocity
ρ_e	=	Exit density
ρ_f	=	Film density
τ	=	Time constant
ν	=	Kinematic viscosity
μ	=	Dynamic viscosity
A	=	Area
C	=	Heat capacity rate
C_H	=	Local heating coefficient
C_{min}	=	Minimum heat capacity rate
C_{max}	=	Maximum heat capacity rate
C_p	=	Specific heat at constant pressure
C_r	=	Heat capacity rate ratio
D_h	=	Hydraulic diameter
De	=	Dean number
F_{th}	=	Thrust force
e	=	emissivity
f	=	friction factor
g_0	=	Gravity at sea level
h_1	=	Inner film coefficient
h_2	=	Outer film coefficient
h_{aw}	=	Adiabatic wall enthalpy

h_{in}	=	Inlet enthalpy
h_{ls}	=	Enthalpy of condensation
h_{out}	=	Outlet enthalpy
h_{vs}	=	Enthalpy of evaporation
h_w	=	Wall enthalpy
I_{sp}	=	Specific impulse
k	=	Thermal Conductivity
L	=	Heat exchanger length
L_{2p}	=	Length of two-phase control volume
L_{sc}	=	Length of subcooled control volume
L_{sh}	=	Length of superheated control volume
$\dot{m}$	=	Mass flow rate
M	=	Blowing ratio
Nu	=	Nusselt number
Pr	=	Prandtl number
$\dot{q}_c$	=	Convective heat transfer
$\dot{q}_r$	=	Radiative heat transfer
$\dot{q}_w$	=	Local aerodynamic heating
$\dot{Q}_{loss}$	=	Heat transfer loss
$\dot{Q}_{max}$	=	Maximum heat transfer
$\dot{Q}_{2p}$	=	Heat transfer in two-phase region
$\dot{Q}_{sc}$	=	Heat transfer in subcooled region
$\dot{Q}_{sh}$	=	Heat transfer in superheated region
R_1	=	Inner convective resistance
R_2	=	Outer convective resistance
R_{ov}	=	Overall resistance
R_w	=	Resistance of the wall
Re	=	Reynolds number
Re_{LO}	=	Reynolds number liquid only
T_{aw}	=	Adiabatic wall temperature
T_c	=	Coolant temperature
T_h	=	Hot side temperature
T_{in}	=	Inlet temperature
T_{out}	=	Outlet temperature
T_w	=	Wall temperature
T_∞	=	Freestream temperature
U	=	Overall heat transfer coefficient
u_e	=	Velocity at edge of bound
u_∞	=	Velocity at freestream
v_e	=	Exhaust velocity
$\dot{W}$	=	Power generation
X_{tt}	=	Martinelli Parameter
Z	=	Log-Incomplete response

ACKNOWLEDGEMENTS

Partial support for this project was supplied by the Dayton Area Graduate Studies Institute. The U.S. Government is authorized to reproduce and distribute reprints for Governmental purposes notwithstanding any copyright notation thereon. The views and conclusions contained herein are those of the authors and should not be interpreted as necessarily representing the official policies or endorsements, either expressed or implied, of Air Force Research Laboratory or the U.S. Government.

1. Introduction

1.1 Motivation

One of the most revolutionary aircraft of its time, the SR-71 blackbird, is a Mach 3+ reconnaissance vehicle and remains the fastest air-breathing crewed vehicle to date. Interestingly, its speed is not limited by the thrust of its engines but instead by the thermal limits of the material. Back in 1947, before the sound barrier was exceeded, reducing drag and increasing thrust was a key focus area. However, providing adequate thrust to reach higher speeds is no longer the most significant problem. Instead, designing a vehicle that can withstand the harsh temperatures and heat loads has become the dominant issue. This is the ideology that governs aircraft design as they enter the realm of high-speed flight [48].

Throughout the years mitigating heat loads has been achieved in a variety of ways, where advances in material science have led to structures that have been able to withstand temperatures exceeding $16{,}000°C$ such as the case for the galileo space probe where an ablative coating was used to entered Jupiter's atmosphere at a healthy clip of $48\ \mathrm{km/s}$ [4848484848]. However, projects such as these are expensive and there is a push for the development of an inexpensive vehicle design that has the capability of long-range flight, incorporating a range of speeds up to the high-speed realm [4]. This is a challenging task where the aircrafts volume and weight must be minimized whilst maintaining a structure that can withstand the harsh thermal environment. Engine efficiency is also a primary concern where air-breathing engines are often preferred, not requiring the use of oxidizer like conventional rockets. However, at these speeds traditional jet engines are not operable and engineers must turn to ramjets or even supersonic combustion ramjets (scramjets) for the air-breathing propulsion system.

1.2 Problem

Unlike conventional jet engines, ramjets have no moving parts and rely on aircraft speed to provide adequate compression. Thus, traditional methods of a shaft driven generator cannot be employed and alternative forms of power generation must be pursued. In addition, at these operational speeds, extreme temperatures are experienced at critical areas of the vehicle, such as near the leading edge of the wing, at the engine inlet or cowl, and the engine housing itself, placing strain on the thermal management system (TMS). This problem is further compounded with advances in fight avionics, radar, and other technologies that impose greater thermal loads on the vehicle. Therefore, developing a TMS that can endure the challenges associated with modern high-speed flight is crucial to vehicle design.

1.3 Approach

Possible areas of interest are the thermal management and power generation requirements of the aircraft. One solution potentially meeting both requirements is a Rankine cycle system. This approach provides cooling using traditional methods of fuel heat sink, where fuel is forced through channels, removing heat from critical areas of the vehicle. However, fuel is also used as a heat source, producing high-pressure steam in the evaporator. The vapor is then used for power generation, reducing fluid enthalpy through the production of mechanical

work. This not only enhances cooling by utilizing the enthalpy of vaporization but also enables the production of power using a shaft driven generator coupled to a steam turbine.

To investigate the Rankine cycle system, an experimental system was developed, incorporating the individual components, and capturing their interactions. This was paired with a numerical investigation using the mathematical modeling language of MATLAB/Simscape. This software was chosen primarily due to its extensive library subsets and its ability to develop custom models. This provided the required toolset to develop component models representing the experimental system. Characterization techniques included mapping component performance with mathematical equations. These results were encoded in component blocks and evaluated through steady-state and transient operations. With increased confidence in these models, a vehicle-level scaled evaluation was performed, assessing dual mode Rankine cycle performance.

1.4 Thesis Organization

This thesis is divided into six chapters. Chapter 2 discusses challenges associated with high-speed flight, specifically thermal management, and power generation aspects in addition to potential solutions. Chapter 3 describes the methodology behind the dual-mode Rankine cycle and its applicability to meet high-speed aircraft requirements. Chapter 4 describes modeling strategies specific to heat exchangers and characterization methods for system components used for experimental modeling. Chapter 5 incorporates vehicle level modeling and discusses governing system requirements specific to flight situations. Lastly, Chapter 6 summarizes results with conclusions and recommendations.

2. Background

2.1 Material Development:

In hypersonic flight, aerodynamic heating tends to govern vehicle design presenting constraints on flight dynamics such as lift-to-drag due to material limitations []. This is primarily because heat flux is proportional to the inverse square of the leading-edge radius, shown in Eqn. 1. Thus, to reduce heat loads the leading-edge radius is increased which in turn increases drag.

$$q_w \propto \frac{1}{\sqrt{R}} \tag{1}$$

Therefore, there exists a large potential for more advanced materials that can withstand these extreme heat loads and temperatures without substantially increasing drag. However, by understanding the flow properties at these speeds, present day materials still show promise for high-speed flight. A notable material, titanium (used for the SR-71 airframe) offers superior specific strength and lower thermal expansion than aluminum alloys. Silica, a ceramic used on the space shuttle orbiter, is another. This material can be weaved into flexible glass fiber blankets offering superior thermal resistance during reentry. Silica can also be combined with boron forming borosilicate offering superior emissivity and, like most ceramics, offers high thermal resistance, Figure 1.

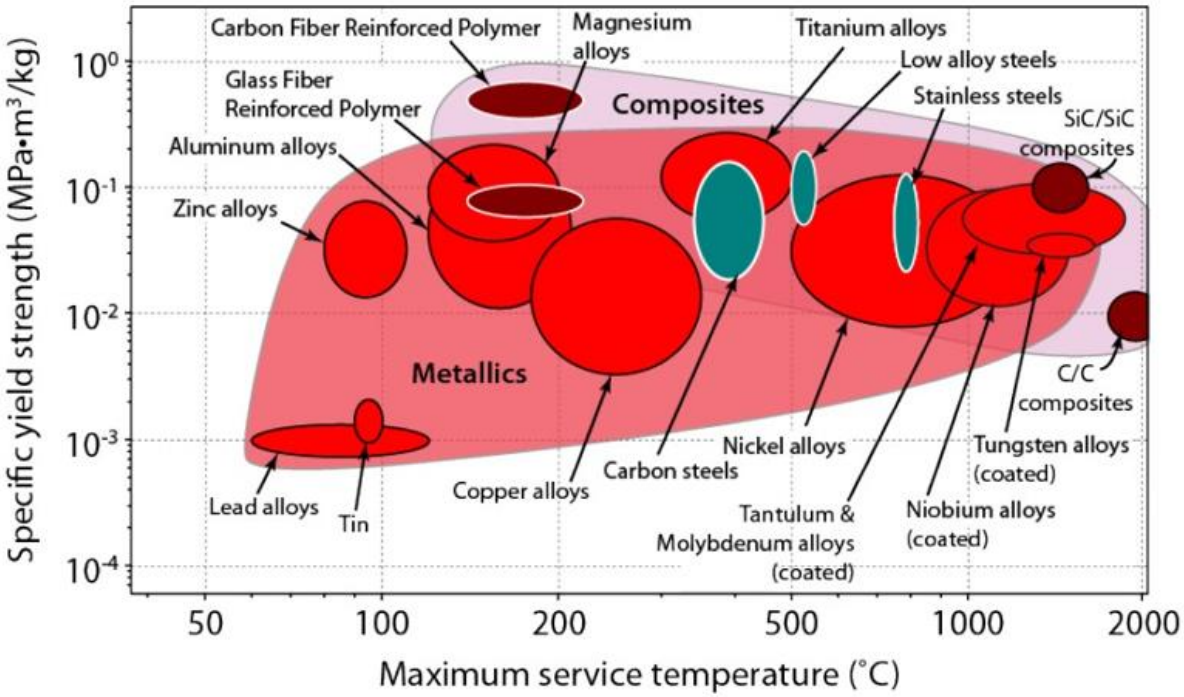

Figure 1: Material properties of various aerospace structural materials [1]

With knowledge of these material properties, when presented with a structural diagram like Figure 2, it is intuitive to gain an understanding for where and at what magnitude these thermal loads occur. This diagram shows structural materials used on the X-51A, an experimental high-speed vehicle that demonstrated the feasibility of a hydrocarbon powered scramjet. At these speeds, leading edges experience some of the greatest heat loads. This agrees with the figure above with Tungsten and Inconel near these areas. These materials have a high maximum service temperature of about $1900\ °C$ and $1000\ °C$ respectively. However, smooth bodies further from these regions experience lower heating rates such as the X-51 fuselage. From Figure 2, this is made up of titanium and aluminum which have a much lower maximum service temperature of about $550\ °C$ and $240\ °C$, respectively. It would be advantageous to have a single material that has all required material properties, a kind of "one size fits all" however, materials with higher strength and service temperatures traditionally have greater density. This is where understanding the margin of error in the thermodynamic heating can drastically improve vehicle characteristics. Materials with greater specific strength and density are only utilized in areas where they are needed.

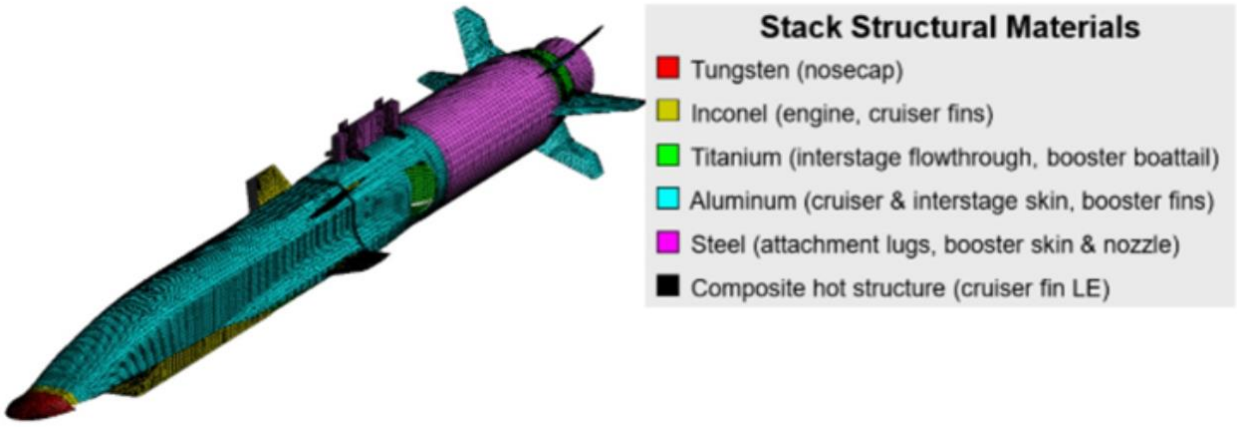

Figure 2: X-51 and boost assist rocket showing exterior materials [2]

2.2 Propulsion Design:

The proper selection of materials is crucial to high-speed aircraft design, ensuring structures can withstand high thermal loads while being light enough for effective flight. However, an efficient means of propulsion is also critical for a long-range vehicle capable of a wide range of speeds.

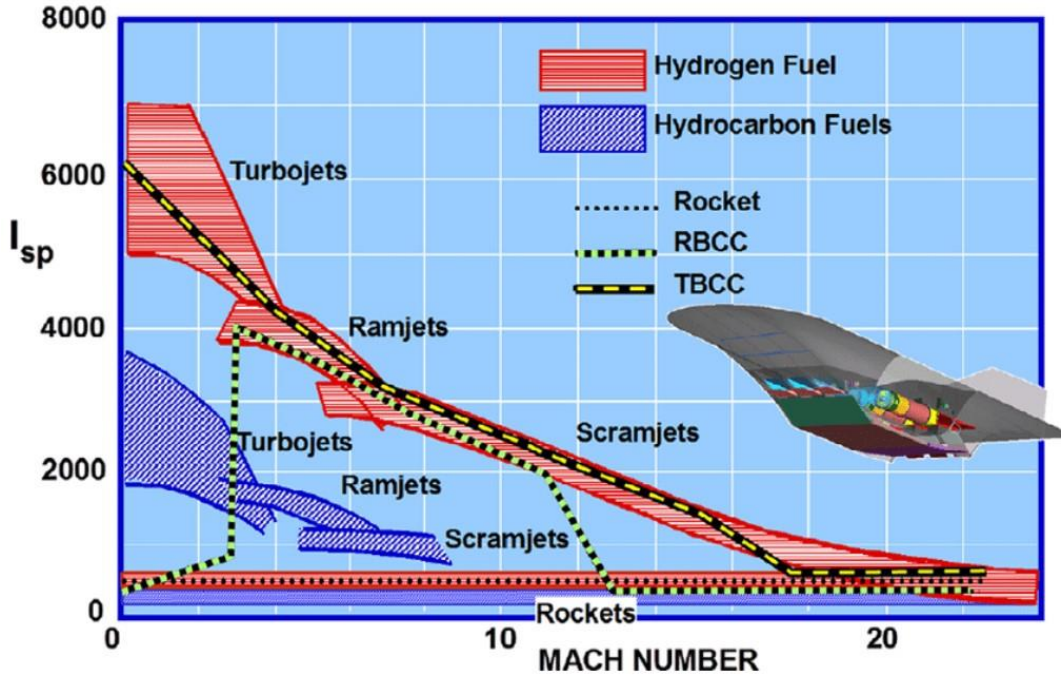

Figure 3: Specific engine impulse for various propulsion engines at varying Mach number with two different fuel configurations [26].

As shown in Figure 3, specific impulse is often used to compare engine performance for airbreathing engines and rockets. This specification measures how efficient a reaction mass engine uses propellent and is inversely related to specific fuel consumption.

$$I_{sp} = \frac{F_{th}}{g_0 \dot{m}} \tag{2}$$

From Eqn. 2, specific impulse, I_{sp}, is the ratio of thrust produced by the engine, F_{th}, over the weight of the propellent mass flow rate, $g_0 \dot{m}$. Based on this definition, its reasonable that airbreathing engines are more efficient than rockets, as they don't have to carry additional weight in the oxidizer. However, rocket engines have many benefits. They incorporate a higher thrust-to-weight ratio where more fuel is burned in a short amount of time. This makes them ideal for vertical take-off and orbital missions, but less efficient for atmospheric travel. For example, the rocket propulsion system on the space shuttle enables an orbital transit time in less than nine minutes. However, this same fuel mass would enable a turbojet driven Boeing 747-200 to remain airborne for about five days, circling the globe twice while carrying an even greater payload. This emphasizes the benefits of specific impulse and thrust-to-weight ratio. Where the turbojet maximizes thrust for a given fuel flow rate, and a rocket maximizes thrust for a given engine weight. Alternatively, specific impulse is often represented in a different form using the definition of thrust, i.e., the time rate of change of the fuels momentum, or simply, the product of the exhaust velocity and mass flow rate.

$$I_{sp} = \frac{v_e}{g_0} \tag{3}$$

Applying this to Eqn. 2, it is evident that exhaust velocity governs specific impulse. In other words, a more fuel-efficient engine will have greater exhaust velocity, Eqn. 3. Written in this form, thrust appears nowhere in this equation. Thus, an engine with greater specific impulse may not lead to greater thrust. Thrust, or the more often used thrust-to-weight ratio, is a design metric considered separately from specific impulse. Like specific impulse, this parameter is important for evaluating engine performance.

As mentioned above, fuel efficiency is a design metric can be measured using specific impulse or the inversely related specific fuel consumption. From the figure above, the performance of airbreathing engines is more favorable than rockets, at all Mach numbers. However, each of these designs are limited to a range of speeds; thus, to forgo the use of oxidizer a multiconfiguration approach must be adopted.

At subsonic speeds jet engines, such as turboprops and high bypass turbofans are very fuel efficient. However, due to their design, these engines are restricted to subsonic flight. Turbojets on the other hand possess respectable efficiencies and operate at much higher speeds. The common operating range for the turbojet is from static conditions to about Mach 3, making them particularly useful for Turbine Based Combined Cycle (TBCC).

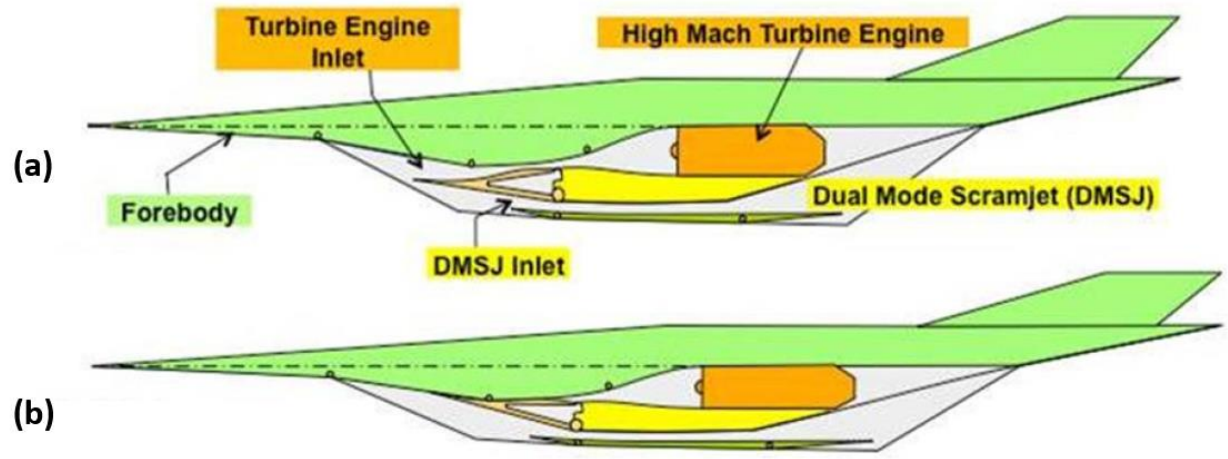

Figure 4: Configuration modes of a turbine-based combined cycle engine, with $\mathrm{Mach} < 4$ **(a)** and $\mathrm{Mach} > 4$ **(b)** [32].

As the name implies the TBCC utilizes a combined approach where a turbine engine is used from static to supersonic speeds and utilizing a separate flow path a switch is made to a scramjet at higher speeds. This is shown in Figure 4 where the turbine engine is positioned above a scramjet known as an over-under TBCC design. From Figure 4 (a) the inlet guide vane is open for the “low speed” flow path, indicating the turbine is operable until about Mach 4. This is a capability that exceeds current engine design, and according to the National Aeronautics and Space Administration (NASA), a “critical enabling technology for the TBCC” [32]. However,

once speeds are greater than Mach 4 there is a mode transition. The “low speed” flow path nearly closes, and the inlet fully opens for the dual mode scramjet. This presents additional challenges such as “unstart” and “buzz” which must be avoided for a smooth transition [32]. At these speeds ramjets and scramjets possess respectable efficiencies but operate on a narrow range of Mach numbers. This range can be made wider by utilizing a dual mode option where a ramjet transitions from subsonic to supersonic combustion known as a dual mode scramjet. These engine variations are discussed in more detail below.

Unlike a turbojet, a ramjet does not use turbomachinery to compress air and instead relies on inlet shape to compress the air at high velocities. Often using a series of shock waves. This converts most of the freestream kinetic energy into internal energy, resulting in a high-temperature, high-pressure gas, adequate for combustion. Therefore, compression is not possible at static conditions and a ramjet is unable to provide thrust. This engines effectiveness usually peaks at around Mach 4. At higher speeds the shock waves intensify causing the air temperature to become so great that it exceeds the service temperature of the material, and the engine design is no longer adequate. An interesting way to circumvent these limitations is to allow the flow to remain supersonic through the engine; this is a supersonic combustion ramjet or scramjet.

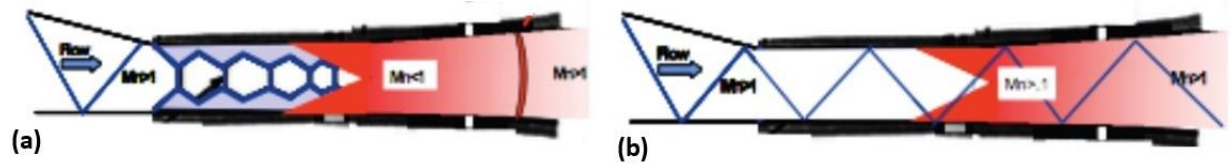

Figure 5: **(a)** Shock trains within the inlet and isolator of a ramjet and **(b)** throughout the entire scramjet [2].

This difference between a ramjet and scramjet can also be explored by observing the shock train that develops within the engines. For a typical ramjet, the shock train resides within the inlet and isolator but stops before reaching the combustor. At this location the mainstream flow transitions from supersonic to subsonic flow, shown in Figure 5 **(a)**. However, for a scramjet the shock train travels through the entire engine, indicating the flow is supersonic throughout, as shocks only appear in supersonic flow. However, as will be discussed shortly, these shock impingements on the engines structure present design challenges for aircraft structure.

Unlike ramjets, scramjets operate at higher speeds, specifically around Mach $5 \rightarrow 6$ [46]; therefore, an initial propulsion platform such as a turbojet is not sufficient for TBCC design. Instead, most scramjet concepts employ a multistage approach where a rocket is used to provide initial thrust until the speed is high enough for scramjet ignition. This is the scheme used for the X-43A and the X-51, except, instead of a rocket to scramjet dual-staged concept, these vehicles used a 3-stage design where they were first dropped from a B-52 Stratofortress at 50 thousand feet prior to rocket ignition. The rocket propels the vehicle until supersonic combustion can be achieved. However, despite the flow being supersonic (having lower static enthalpy) there are still large concerns with heat mitigation. In fact, there is a plethora of published research dedicated to developing and optimizing the TMS for the scramjet engine.

2.3 Thermal Management System:

For high-speed vehicles, the TMS often provides cooling to the engine's structure and exterior surfaces of the aircraft. This ensures structural limits are within service temperatures of the material. The TMS also maintains stable operating temperatures for onboard electronics (e.g., sensors, radar, display, etc.). In thermal management design there are two systems often employed, passive systems which do not rely on coolant, and active systems which use a continuous supply of liquid to provide convective cooling. Three common types of passive systems are ablative, insulative, and heat sink, shown in Figure 6.

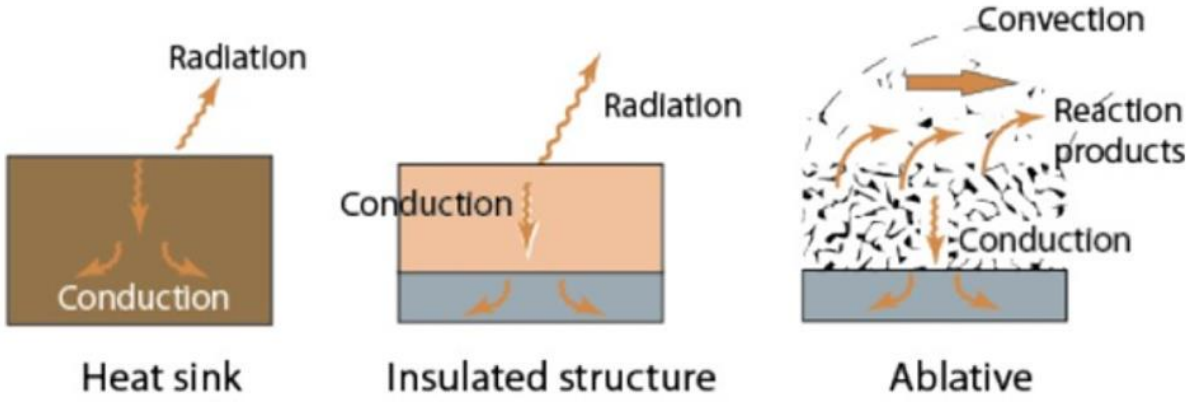

Figure 6: Basic passive TMS concepts [1]

2.3.1 Heat Sink

A heat sink is a material that absorbs, stores, and evenly distributes heat; thus, high thermal conductivity, k (ensuring even heat distribution), and high heat capacity, C_p (ensuring a high thermal storage) are ideal properties. The overall heat sink capability of the material is measured by emissivity, e, where

$$e = \sqrt{kC_p\rho} \tag{4}$$

However, the storage capacity of a heat sink sink is directly related to its mass, where higher mass ultimately leads to greater size and weight. This was a viable option for the development of the InterContinental Ballistic Missile in the 1950s where copper was used on the rocket nosecone. However, for high-speed vehicles, with a primary goal of limiting weight, structural materials with a sole purpose of absorbing heat are rarely considered and instead the fuel is used as the heat sink.

2.3.2 Insulative

An insulative structure is a material or layering of materials that offers high thermal resistance and high thermal emissivity, producing large thermal gradients by restricting heat flux to the underlying structure. This TMS can often be divided into two categories; ceramic materials that are either a coalition of widely spaced fibers, woven fiber blankets, or formulated into closed cell foam, or a gap or standoff that is filled with gas or exists as a vacuum.

2.3.3 Ablative

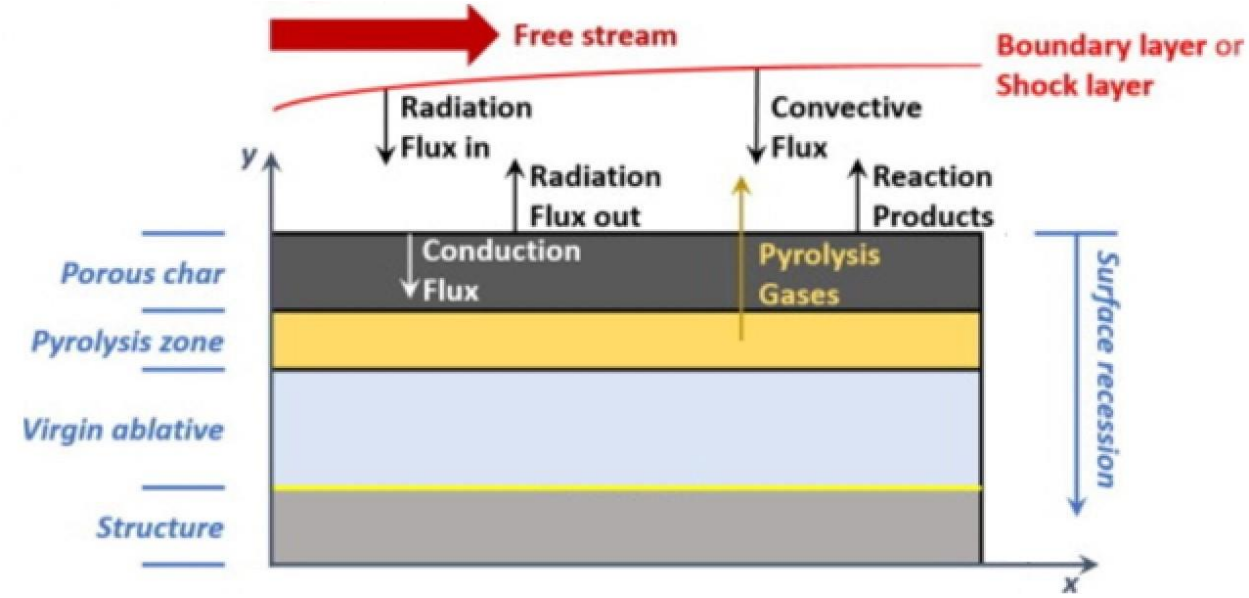

Figure 7: Structural interior of ablative coating showing the endothermic ablative process during high thermal heating, adapted from Riccio [25].

An ablative TMS is a single use coating often applied to the windward side of the aircraft providing a chemical reacting layer. This insulates the structure from extreme thermal environments such as atmospheric reentry. The ablation coating is made of “composites that are reinforced with organic resins” [9] that, when heated, pyrolysis occurs where the chemical reaction and phase changes absorb heat in the process of forming a hydrocarbon gas. This gas then percolates up and is injected into the oncoming flow. This thickens the boundary layer, providing a thermally insulative layer for the vehicle. The material left over, known as carbonaceous residue, or char, forms a highly emissive insulative layer that offers further thermal resistance. This type of ablative shielding is used for reentry vehicles typically carrying astronauts from the International Space Station to Earth such as Soyuz and Dragon 2 space capsules.

2.3.3 Active TMS

Passive TMS are often utilized on the exterior of high-speed vehicles, providing insulation from the extreme temperatures produced from aerodynamic heating. However, for interior structures, such as inside a scramjet, active TMS are often employed [1] [4] [9].

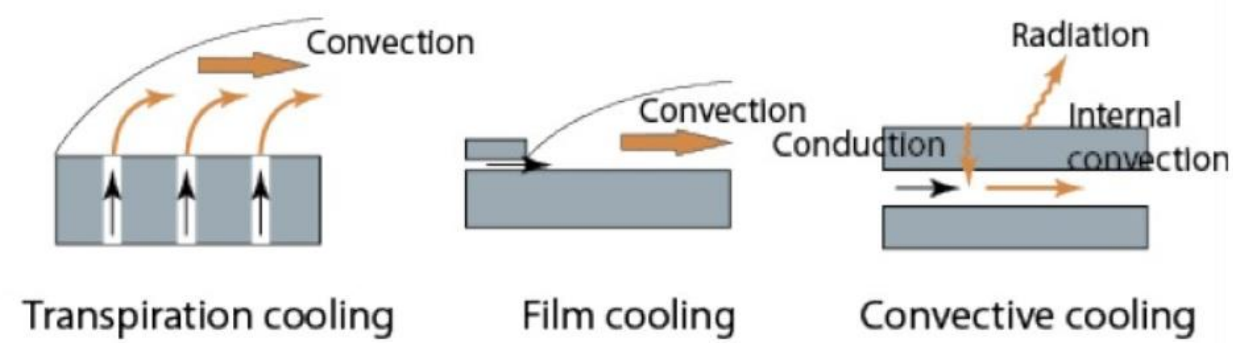

Figure 8: Basic concepts for active TMS [1]

The main difference between active and passive TMS concepts is active systems rely on forced convection using a coolant to absorb and remove heat from the structure, and passive TMS only rely on material properties to provide a thermal barrier without the aid of a coolant. Shown in Figure 8, some basic types of active TMS are transpiration cooling, film cooling, and convective cooling. Transpiration cooling and film cooling are very similar. Fluid is forced through gaps or holes in the surface and injected into the boundary layer. This provides cooling in two ways; the coolant travels through the surface, removing heat before being injected into the boundary layer. Also, the coolant reacts with hot gas reducing the temperature near the wall by producing a cooler layer or film that coats the surface. This reduces the thermal gradient between the wall and hot gas, which in turn reduces heat flux. A common approach used to equate this heating is the adiabatic wall enthalpy method.

$$q_w = \rho_e u_e C_H (h_{aw} - h_w) \tag{5}$$

From Eqn. 5, the main mechanism for aerodynamic heating is the difference between the adiabatic wall enthalpy, h_{aw}, and enthalpy at the wall, h_w. Also utilized is the Stanton number, C_H.

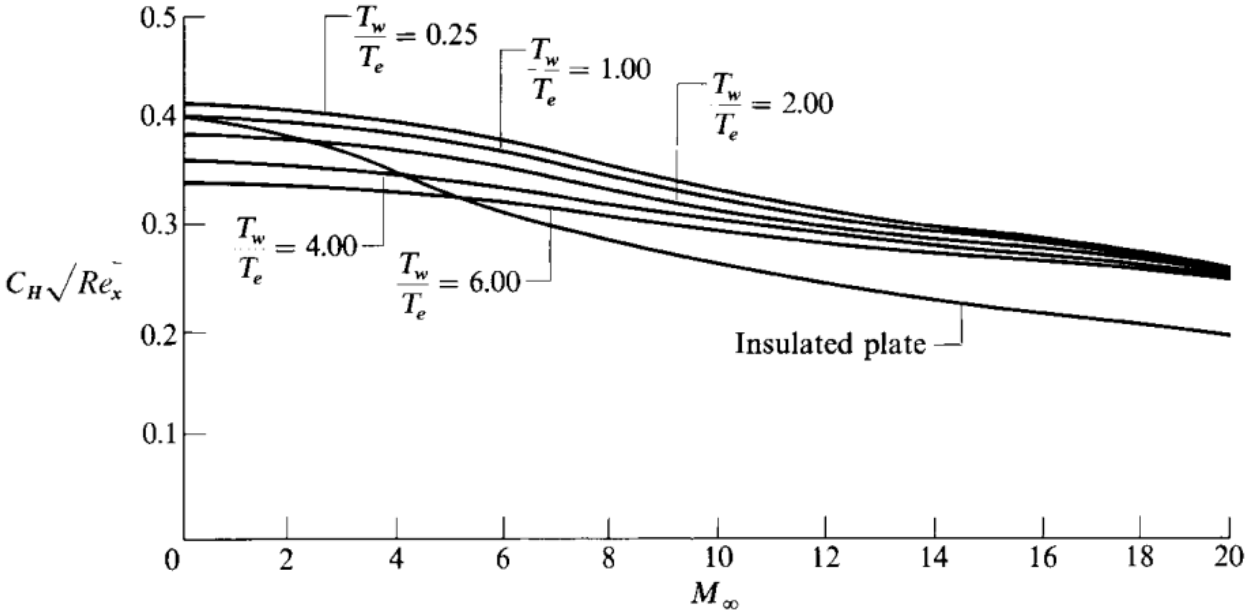

Figure 9: Stanton numbers for compressible flow over a flat plate [48].

From Figure 9, the Stanton number is a function of the streamwise Reynolds number, Re_x, ratio between the temperature at wall, T_w, and boundary layer edge, T_e, and the freestream Mach number, M_∞. This figure was populated using a numerical approach known as Crocco's theorem solving the governing differential equations of mass, momentum, and energy.

Assuming constant specific heats Eqn. 5 can be rewritten showing that the temperature difference is the "driving potential" for heating.

$$q_w = \rho_e u_e C_H C_p (T_{aw} - T_w) \tag{6}$$

Thus, instead of the adiabatic wall enthalpy this equation references the adiabatic wall temperature, T_{aw}. As the name implies, this temperature results in no heat transferred to the wall. It may seem logical that this is simply the stagnation temperature of the gas, observing the no slip condition. However, for the case of the flat plate the actual wall temperature can be less and is dependent on fluid properties.

Since temperature difference is the main "driver" for heating a temperature profile can be used to represent local heat flux rates. A classic example of film cooling and or transpiration cooling is shown in the figure below where a normalized temperature, θ is used to represent the heat distribution.

$$\theta = \frac{T_\infty - T}{T_\infty - T_c} \tag{7}$$

The local normalized temperature is defined using Eqn. 7 where $\theta = 1$ corresponds to the coolant temperature at the injection sight and $\theta = 0$ indicates temperature of the freestream gas.

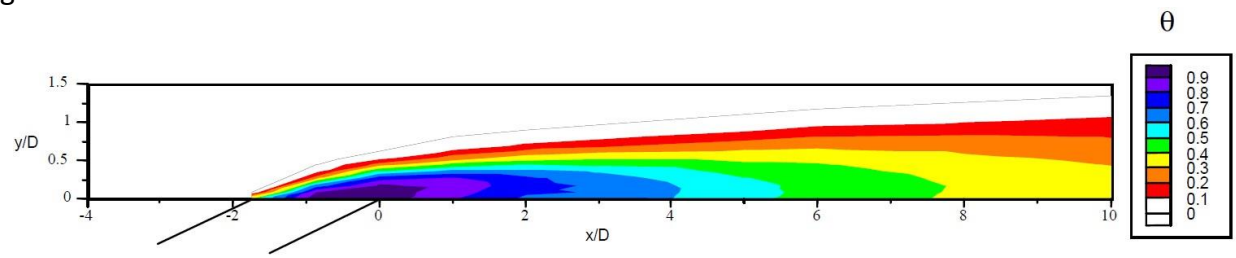

Figure 10: Normalized temperature distribution taken through the centerline of a cooling jet showing the injection of coolant into the boundary layer [28].

Shown in Figure 10, at the injection site $(x = 0)$ film cooling has the greatest influence on the temperature distribution with $\theta \approx 1$. However, as the coolant is carried downstream it mixes with the mainstream flow and the bulk fluid temperature steadily increases. Thus, cooling is very effective at the the injection sight but decreases downstream.

Besides providing cooling, this concept can also prevent oxidation by reducing interactions between the surface and free-stream oxygen. This technique is applicable to both film cooling and transpiration cooling as both techniques form a thin coolant layer that coats the surface, reducing surface exposure to mainstream oxygen.

Due to their delivery mechanisms, transpiration cooling is different than film cooling. Physically speaking, transpiration cooling uses a porous medium to disperse coolant into the boundary layer where film cooling uses specific channels directing flow through a particular path. There is no set flow path using transpiration cooling due to the composition of the porous medium. Micrometer sized channels guide the flow in random directions before being injected evenly into the boundary layer. Thus, more control is possible with a film cooling TPS where coolant injection angle and Mach number can be regulated through channel design. Additionally, precisely placed holes rather than a porous medium offer greater structural rigidity for components under high stress [35]. This makes film cooling well suited for turbine engine design.

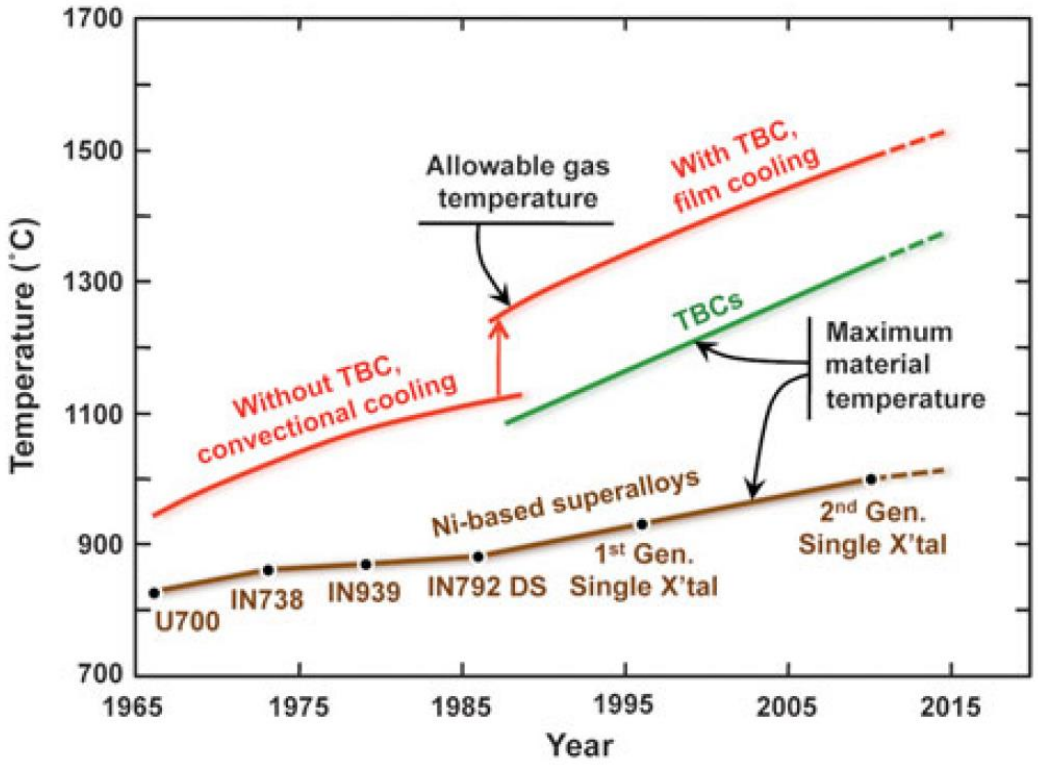

Figure 11: Progression of thermal capabilities showing temperature limits of structural material (Ni-based superalloy) and thermal based coatings (TBC) with enhanced capability film cooling offers [33].

As shown in Figure 11 gas temperatures within a turbine engine can be higher than thermal limits of the material. This is advantageous in increasing engine efficiency and power production [35]. In fact, due to the apparent benefits film cooling is used on nearly every modern engine [34]. With some of the highest thermal stresses, first and second turbine blades often incorporate some form of film cooling. Bleed air drawn from the compressor is forced through guide vanes inside the blade before being injected into the boundary layer. This way, cooling is provided to the interior structure before coating the outer surface insulating it from the hot gas. Unfortunately, using film cooling for a scramjet TMS presents design challenges due to the high-speed nature of the flow path.

Unlike turbojets or ramjets, flow through the scramjet is entirely supersonic. For this engine design film cooling is commonly referenced as supersonic film cooling. At these speeds film cooling is less effective primarily due to the shocks that form continuously through the engine. As researched by Peng et. al., when shocks interact with the boundary layer there is an adverse effect on film cooling efficiency leading to a temperature increase near the wall and and greater heating. Zhang et al. investigated supersonic film cooling effectiveness in the inlet and isolator of scramjet using a numerical model validated using data from Juhany et al. [36]. In this research four parameters were varied, namely, injection angle, injection Mach number, blowing ratio, and freestream Mach number. Using the finite volume technique with upwind discretization, it was found that the injection angle had little influence on film cooling efficiency

at lower angles. However, at larger angles flow disturbances were present leading to a significant reduction in flow velocity when $\theta > 45°$. This led to higher heat flux due to the high stagnation temperatures within the engine.

$$M = \frac{\rho_f u_f}{\rho_\infty u_\infty} \tag{8}$$

Additionally, it was found that as coolant Mach number, M_c and blowing ratio, M (Eqn. 8) were increased, cooling effectiveness improved. This outcome is rather predictable considering increasing either of these parameters leads to a higher coolant flow rate. Thus, more coolant in the main flow reduces the temperature gradient at the wall. However, it was noted that increasing these parameters had a negative effect on pressure recovery. Although this effect was small when compared to the benefits in heat mitigation. For example, when the coolant Mach number and blowing ratio was nearly doubled there was a 20% increase in film cooling effectiveness but only a 4% decrease in total pressure recovery. Therefore, because the cooling effectiveness continues to increase with mass flow rate, despite this small reduction in pressure recovery, these parameters can be controlled optimizing aircraft design.

As discussed above, film cooling is incorporated in modern turbine engine design; however, it relies heavily on recovering cool bleed air. This makes it less applicable to high-speed engines such as scramjets. At these speeds extreme stagnation temperatures are present. Thus, when bleed air is directed through narrow channels the flow may reach subsonic speeds due to shock formation and therefore exceed material thermal limits. Because of this, other methods are often employed, such as regenerative cooling.

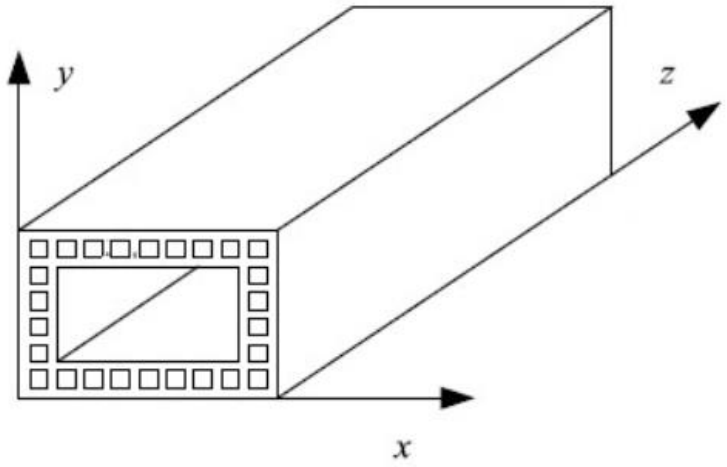

Figure 12: General rectangular scramjet cooling channel [4].

Regenerative cooling is another method that utilizes convection to insulate critical structural components. This method employs a similar approach as transpiration cooling and film cooling where a fluid decreases the thermal gradient at the wall, thereby decreasing heat transfer. However, regenerative cooling specifically utilizes the fuel as coolant confining it

through a particular flow path, known as a cooling channel. This is shown in Figure 12 where flow channels represent the structure of a scramjet engine. For most designs it is often advantageous to utilize fuel as the cooling medium eliminating the need to carry additional weight in coolant.

Regenerative cooling is often used for liquid fueled rockets and high-speed air breathing engines [37]. The X-15 and X-51 utilized this TMS with their respective fuels as coolant. The X-51 demonstrator was a research aircraft powered by a scramjet engine using a hydrocarbon fuel (JP-7) whereas the X-15 was a rocket powered plane using anhydrous ammonia and liquid oxygen as propellant. For cooling designs, fuel was pumped through cooling channels surrounding critical components of the engine, absorbing waste heat before being burned in the combustor and exhausted. These fuels were specifically selected due to their ideal thermal storage properties, e.g., high specific heat and latent heat of vaporization. This keeps the fuel temperature low while enabling more heat absorption.

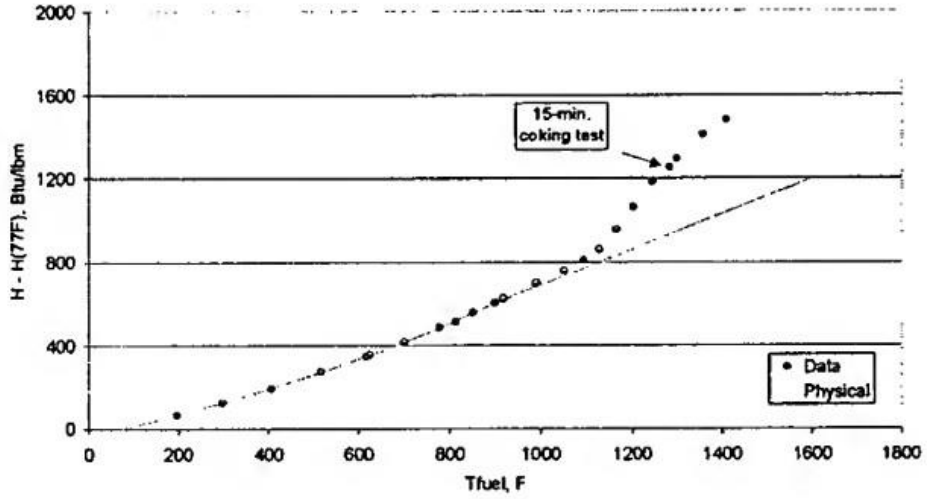

Figure 13: Progression of specific enthalpy of JP-7 with increasing temperature [6].

When a hydrocarbon fuel is heated eventually an endothermic process occurs, known as fuel cracking or pyrolysis. At a critical temperature, the long hydrocarbon chains begin to break into smaller, lighter molecules, accessing additional energy modes. This increases the fuel specific heat, allowing for greater thermal storage. This process is shown in Figure 13 where the slope of the curve (representing the specific heat) increases at the cracking limit of JP-7 at around $1000°F$. At this point the specific heat increases, reaches an inflection point, and levels off near the coking limit at about $1300°F$.

Coking is an unfavorable process where carbon begins to accumulate as a byproduct of fuel cracking. This clogs fuel lines and eventually leads to engine failure. This process can be prevented if the fuel temperature is controlled through engine design such as regulating the fuel flow rate. However, this can cause design inefficiencies if the flow rate exceeds the needs of the engine. Excess fuel is exhausted without being utilized for thrust and the “wet” weight of the craft must be increased as well.

Unlike hydrocarbon fuels, fuel pyrolysis does not occur when using hydrogen. Additionally, this propellant has a specific heat that is seven times greater than most kerosene

derived fuels (at STP) and its value continues to increase with temperature, eventually dissociating at 1500 K. However, one of the most desirable properties of hydrogen is its high specific impulse.

$$I_{sp} = \frac{1}{g_0}\sqrt{\frac{2\Delta h}{m_m}} \tag{9}$$

Using a theoretical approach, the specific impulse of any fuel can be determined using an energy balance assuming all chemical reaction energy is converted to molecular kinetic energy. From Eqn. 9, Δh is the enthalpy change of the reaction, m_m is the propellant molar mass, and g_0 is the force of gravity at sea level (for more information regarding this derivation see Meyers [38]). This represents the maximum possible specific impulse of an engine. Comparing theoretical values between hydrogen and anhydrous ammonia (used on the X-15 XLR99 rocket engine) hydrogen outperforms by 41% with a specific impulse of 532.5 seconds. In fact, hydrogen with oxygen as oxidizer has the greatest specific impulse of any known propellant [40]. This is primarily why hydrogen is used in both rocket and air-breathing engine designs. Simply put, it produces the greatest amount of energy per unit weight of propellant.

The X-43A research vehicle used hydrogen as propellant. This fuel provided enough thrust to accelerate the craft to Mach 9.68 on November 16th, 2004, using a scramjet engine. To withstand the extreme aerodynamic heating at these speeds, carbon-carbon composites were added to the leading edges and ceramic tiles were applied to the aircraft body. A material design like the Space Shuttle. However, traditional methods of regenerative cooling were not used to cool the engine. This was primarily due to the short engine test runs (around 10 seconds) making it impractical to use fuel as coolant. Instead, a secondary fluid was utilized, specifically, a glycol-water mixture during the boost phase, and pure water during scramjet testing [39]. However, this was a research vehicle. For a final aircraft design the scramjet engine will cover a wider range of Mach numbers, utilizing longer burn times. Thus, it may be more applicable to employ regenerative cooling.

There are many benefits that make hydrogen a preferred fuel for high-speed applications. Most notably its high energy density, being about four times greater than most kerosene derived fuels. This leads to greater fuel weight savings compared to hydrocarbon fuels. However, there are also many disadvantages. For example, it has a very low density ($71\ \mathrm{kJ/kg}$ at $23\ \mathrm{K}$ and $1\ \mathrm{atm}$), requiring three times more volume space than most hydrocarbon fuels, using a simple calculation comparing products of energy density and specific volume. This ultimately leads to larger, heavier tanks that limit aircraft design. Additionally, with a vaporization temperature of $23\ \mathrm{K}$ the fuel must be stored cryogenically to avoid over pressurization. This presents additional complications e.g., specialized materials, thick walls, boil off valves, to name a few. Alternatively, critical hydrogen could be utilized; however, this nearly doubles the required volume at $700\ \mathrm{bar}$ (maximum tank pressure). Furthermore, as discussed by Killackey et. al, there are also problems utilizing hydrogen for regenerative cooling at high Mach numbers, illustrated in Figure 14.

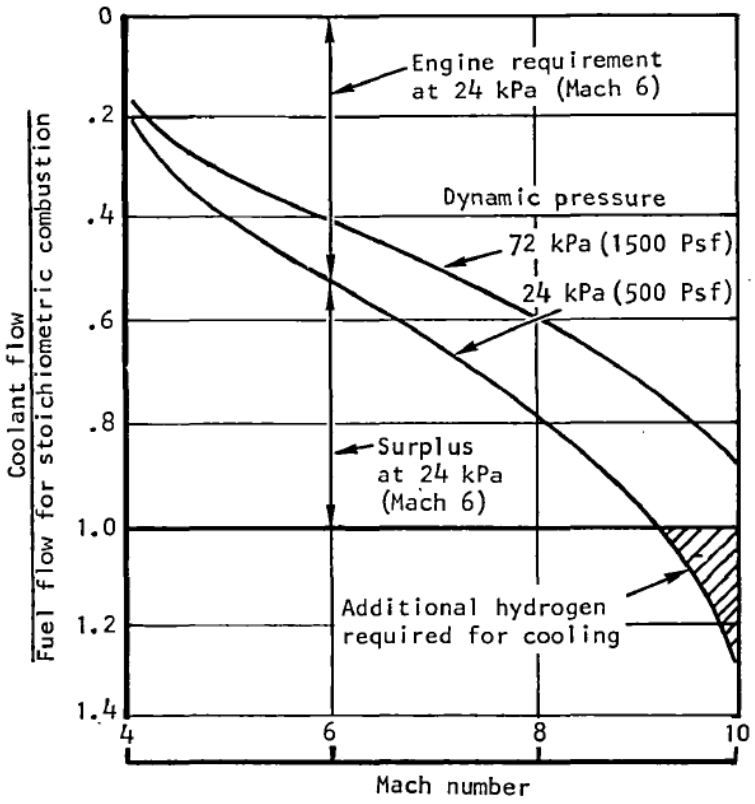

Figure 14: Coolant requirements for a hydrogen powered scramjet engine [42].

Using a numerical analysis Killackey et. al assess the performance of a regeneratively cooled scramjet engine. This was was to power a concept high-speed research vehicle with a "mass after rocket burnout of about 21,000 lbs". The engine was divided into six modules, each having a height, width, and length, of 18 in., 14.4 in., and 10.31 ft, respectively. The process used to make these predictions in Figure 14 follows. Required fuel flow rates for the given conditions was provided by NASA-Langley Research Center; thus, coolant flow (ordinate numerator) was a known parameter. Coolant flow for stoichiometric combustion (ordinate denominator) was determined using a set fuel thermal limit (based structural capabilities) and heating obtained by the adiabatic wall enthalpy method. Lastly, the flight envelope was considered for two dynamic pressures incorporating altitude variations.

From Figure 14, at Mach numbers greater than 9 fuel flow does not satisfy cooling requirements for some flight conditions. However, this analysis only incorporates thermal loads of the engine; thus, heating accrued from other areas (electronics, aircraft structure, etc.) may result in further limitations. Inadequately designed cooling jacket channels may also require higher flow rates to reach necessary heating rates. Thus, is it advantageous that nominal cooling jacket operations are within engine requirements.

In the design of a hydrogen powered scramjet cooling jacket, Scotti et. al., optimized performance by making the fuel flow rate the objective function specifically, by limiting this parameter. This is contrary to the common goal of minimizing weight because the cooling jacket contributes little to the overall mass but can negatively influence other aircraft parameters (e.g., pumping requirements, engine efficiency, flight range, etc.). Besides coolant

flow, other design limitations were considered, including material temperature limits, stress, fatigue, Mach number, and pressure drop through the channel. Two structural concepts were considered i.e., channel-fin and pin-fin as well as three structure materials, namely Nickel 210, Zirconium Copper, and Titanium Aluminide. Parametric assessments were applied varying inlet pressures and heating rates evaluating performance of the possible configurations. This was shown to determine ideal heat exchanger concepts, material, and geometry that minimized the coolant flow rate.

Main conclusions drawn from this evaluation show the channel-fin design, utilizing Nickel 210, outperforms the pin-fin design for all heating rates. This was due to the complex interaction between the Mach number and fatigue constraints. These parameters were the main contributor that increased coolant flow rate, something that was unknown prior to this investigation. The main difficulty for both designs occurs when low inlet pressure and high heating rates were investigated. This is because this activated the Mach constraint as the density of hydrogen decreased leading to an increase in coolant velocity. To prevent this, the channel area was increased. This, however, activated the fatigue constraint as heat transfer decreased, increasing the temperature gradient. To circumvent this, the coolant flow rate was increased; however, this again activated the Mach constraint and channel area was again increased. The process was repeated until both constraints were satisfied. This presents an interesting relationship between the Mach number and fatigue constraints.

The pin-fin design had comparatively lower channel area; thus, this interaction between Mach number and fatigue was more prominent. This heavily influenced the objective function, so much so that extreme temperatures no longer govern design and Zirconium Copper, and Titanium Aluminide become more favorable materials offering better fatigue resistance. The optimal design configurations for these two cooling-jacket concepts were used to determine the optimal coolant flow rate as a function of heat flux as shown in Figure 15.

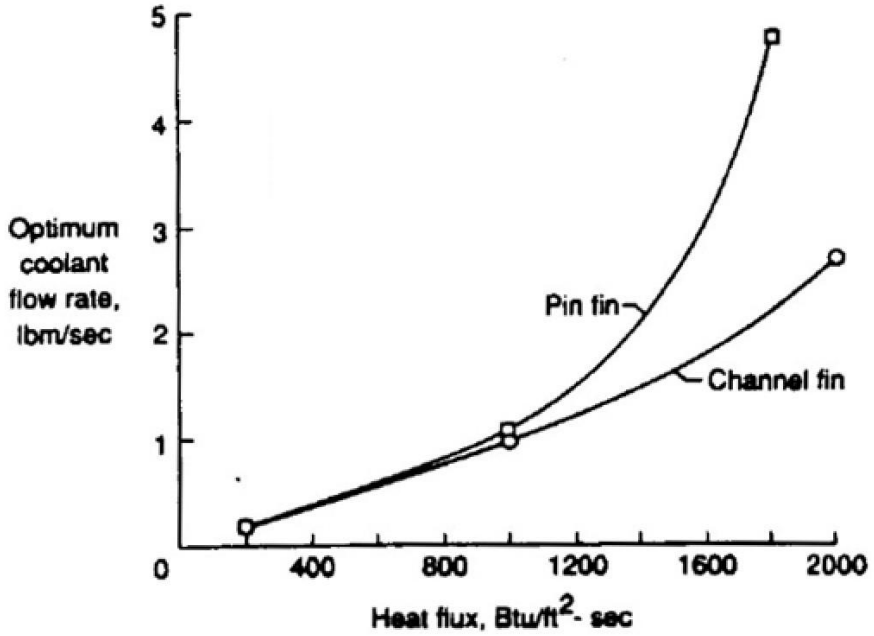

Figure 15: Progression of the optimal coolant flow rate for Nickel 210 channel-fin and pin-fin concepts utilizing an inlet pressure of 3000 psi [3].

The above analysis relied on a simplified case where a single $36" \times 36"$ panel was used, simulating heating from all components of the engine together. However, for an investigation of fuel routing affects Scotti et. al. also performed a three-panel investigation simulating cooling through three separate sections of the scramjet, namely, the inlet, combustor, and nozzle. As shown in Figure 16, a flow routing scheme independent of the flow path minimizes the coolant flow rate to $3.32\ \mathrm{lbm/s}$. However, this may lead to large thermal gradients in the structure. A more simplistic design is to plumb coolant consecutively through each panel, limiting these temperature gradients. This however does increase the objective function with a 4% increase in coolant flow rate for the inlet-to-nozzle scheme and a 17% increase for the nozzle-to-inlet scheme. Purely based on these results the independent and inlet-to-nozzle flow routing schemes are best; however, this investigation was not proposed to define an optimal flow plan but merely discussed routing effects. Obviously, there are added complexities when selecting the optimal fuel path where other vehicle design considerations must be realized.

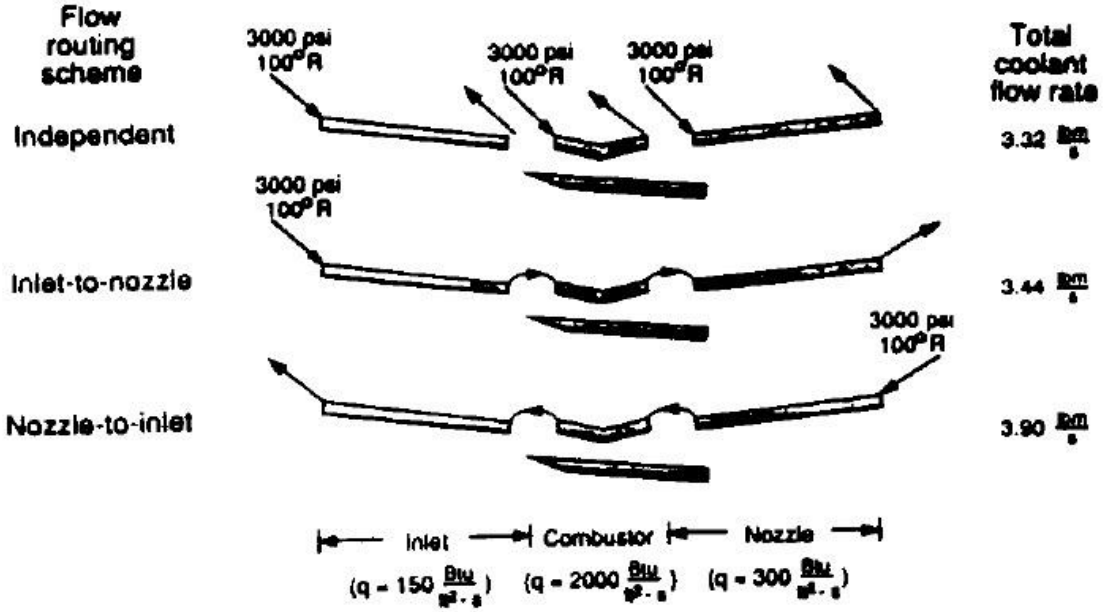

Figure 16: Coolant flow routing scheme for three different configurations using a set inlet pressure and temperature of $3000\ \mathrm{psi}\ 100°\mathrm{R}$ and constant heating rates for the inlet, combustor, and nozzle [3].

Another possibility for scramjet cooling is to utilize regenerative cooling and film cooling in tandem. Research was performed by Zuo et al. for a hydrocarbon fueled scramjet assessing the potential benefits of this approach. This method takes advantage of the proven regenerative cooling cycle while incorporating an additional thermal mode. In this design, fuel is pumped through scramjet cooling channels absorbing heat, which eventually causes fuel pyrolysis until the fuel coking limit is achieved. The supercritical fuel is then injected into the combustion mainstream flow cooling the walls as it reacts with the turbulent boundary layer. A diagram of this approach is shown in Figure 17 below.

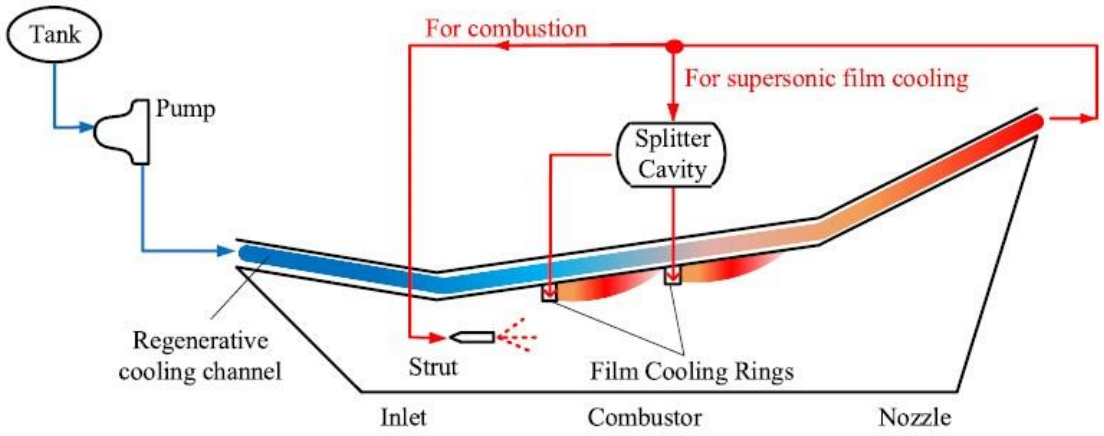

Figure 17: TMS scheme for a scramjet engine incorporating regenerative cooling and film cooling [4]

Using N-Decane with the fuel flow rate set to stoichiometric conditions, a one-dimensional model was developed. Due to the lack of experimental data, CFD was used for model validation. Conclusions from this research suggested greater cooling performance with an 8% increase in flight Mach number with the engine wall temperature restricted to $1300K$. Wall temperatures are shown in the figure below overlayed with results from regenerative cooling only. From the figure, the dual TMS offers a decrease in temperature of about 30°C from the first instance of film cooling ($x \approx 0.3$) and even more at the second instance at ($x \approx 1.1$). The dips in temperature at the fuel injection site are an artifact caused by ignoring axial heat transfer.

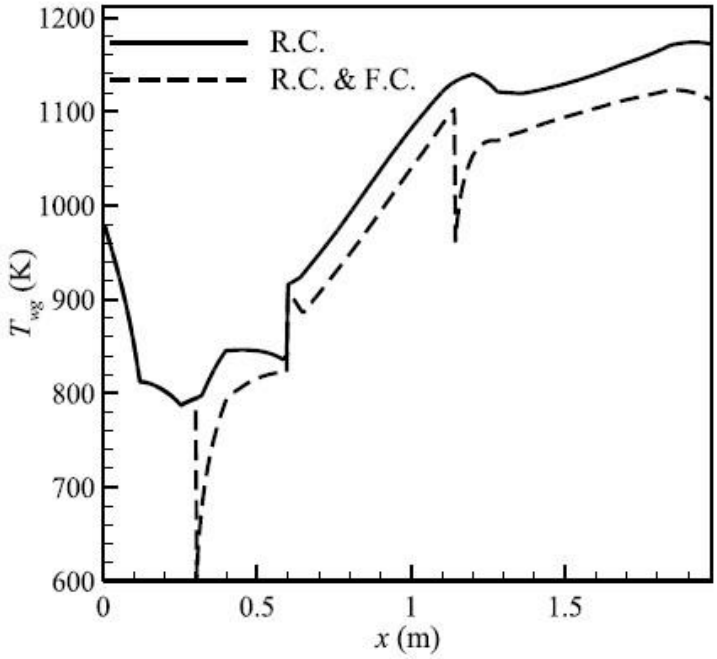

Figure 18: Wall temperature within a scramjet engine using a bulk flow temperature of 1930 K [4].

2.4 Power Generation:

As discussed previously, one of the biggest challenges for high-speed vehicles is managing heat loads with adequate TMS design. One of the most proven techniques is regenerative cooling. This method increases engine efficiency through fuel heating and does not require additional coolant for considerable weight saving. Propulsion design is also critical; thus, the engine must be very efficient. This ensures aircraft design is optimized for high-speed, long-range missions. At high Mach numbers the scramjet offers optimal performance. However, it has no moving parts and traditional methods for electrical power generation utilizing a shaft driven generator are not suitable. Consequently, novel methods must be employed for power generation. One approach investigated by Haowei et. al, takes advantage of the strong expansion that occurs during the regenerative cooling process. This approach is like the expansion cycle typically used on the first stage of a rocket where, after cooling the engine, the fuel is expanded through a turbine providing necessary mechanical work. This is advantageous for high-speed design due to its high efficiency and structural simplicity [5].

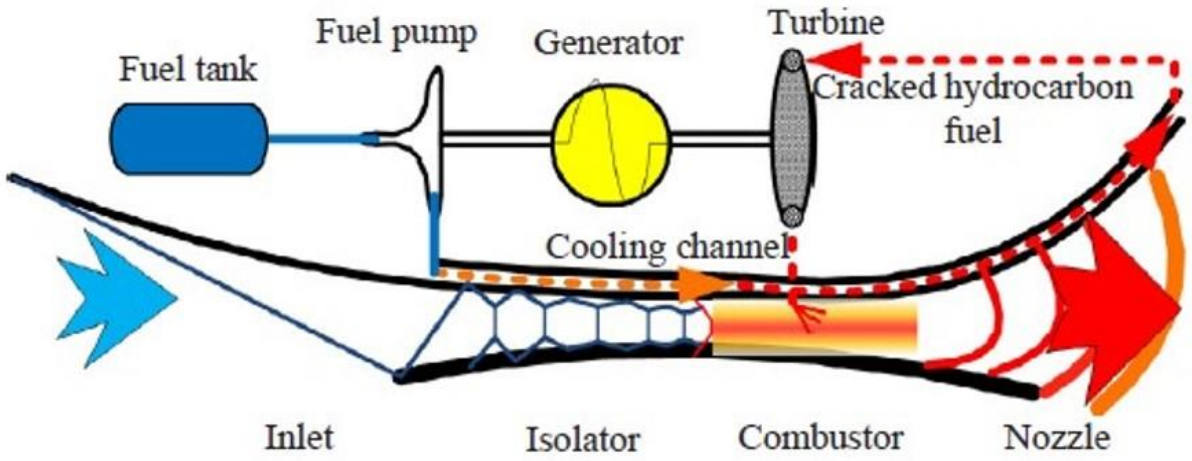

Figure 19: Combined TMS and power generation diagram utilizing expanded thermally cracked fuel [5]

As shown in Figure 19, this system combines thermal management with power generation. Fuel is pumped through regenerative cooling channels incurring endothermic pyrolysis and absorbing heat. These cracked and uncracked hydrocarbons then expand through the turbine, producing power, before being burned in the combustor. The optimization of this work relied on developing analytical models investigating the work generating capabilities of hydrocarbon fuel. The model was validated with an experimental system using a 500 kw nickel alloy electrical heater and an axial flow turbine mounted on gas bearings with peak efficiency of 0.8. However, due to the high temperature hydrocarbon gas, thermal deformation limits of the turbine were reached before it could achieve appropriate design speeds. Thus, peak efficiency was well below design, at about 0.19.

Further investigations determined system performance using a hydrocarbon fuel (RP-3). The main parameters evaluated were mass flow rate, temperature, and fuel heating pressures.

These properties were then varied and changes in isentropic enthalpy were used to evaluate power generation capabilities of the system.

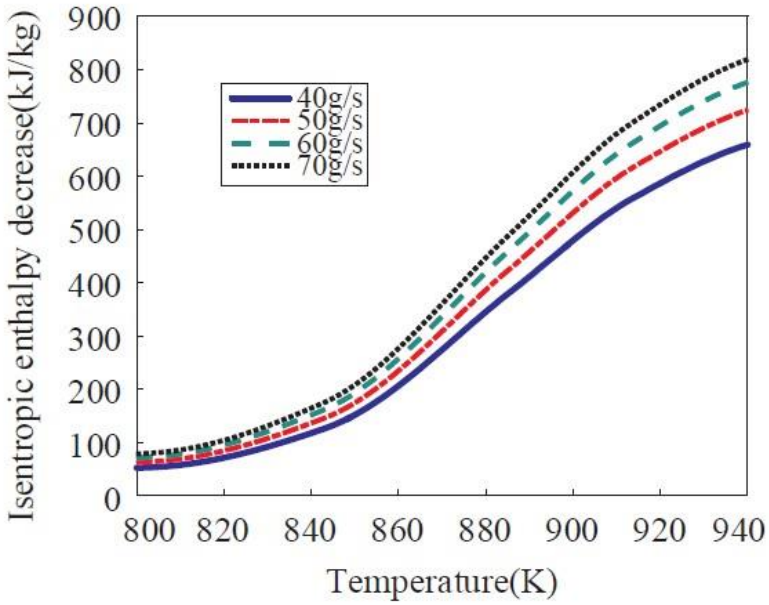

Figure 20: Influence of temperature and mass flow rate on potential power generation of RP-3, referencing isentropic enthalpy [5].

From the figure above, temperature has a substantial effect on the work doing potential of hydrocarbon fuel RP-3, referenced by the change or decrease in isentropic enthalpy across a hypothetical turbine. These effects become noticeable at $800\ \mathrm{K}$ where the slope begins to increase, most prominent at $860\ \mathrm{K}$ having the greatest slope, and less of an effect at higher temperatures, nearly leveling off at $940\ \mathrm{K}$. However, at this upper bound $(940\ \mathrm{K})$ the slope is still positive; thus, the optimal temperature has not been achieved. This temperature was constrained due to the coking limits of RP-3. Thus, for an optimal design this may represent the turbine inlet condition which produces maximum power.

Different flow rates were also analyzed. Figure 20 shows higher flow rates offered greater potential for work, most notable at higher temperatures. For both parameters, changes in enthalpy affected the pyrolysis process, specifically where higher temperatures and flowrates lead to more molecular dissociation. This resulted in better operational state points at the inlet and exit of the turbine providing a greater enthalpy change. This also became apparent when analyzing various heating pressures varied from 3 to $5\ \mathrm{MPa}$. Higher pressure increased conversion, again leading to greater isentropic enthalpy decrease. However, these variations were slight, and instead were primarily dependent on temperature such as the case from above. This suggests increasing heating pressure presents little benefit toward power generation within this range.

With the optimization of these parameters, and model purposed by Haowei et. al. validated with empirical results, these results present interesting findings that may support future research. Main conclusions drawn from this analysis show obvious benefits for high-speed vehicle design. Utilizing regenerative cooling and cracked hydrocarbon power generation

together offers considerable weight savings where the fuel is used as coolant heated through cooling jackets and incurring pyrolysis until adequate molecular dissociations occurs. Finally, the cracked fuel expands through a turbine, producing necessary power.

Compared to the alternative rocket engine, a scramjet is a more efficient means of propulsion for a multi-use long-range high-speed aircraft. As discussed by Zuo et al., the regenerative cooling cycle utilizing fuel as the heat sink is a viable TMS for high-speed vehicles utilized by the X-15 rocket plane and X-51 Waverider. Additionally, it was found that pairing this TMS with film cooling offered an 8% increase in flight Mach number. However, because combustion is supersonic, traditional methods of power generation would result in thermal protection issues and aerodynamic drag [5]. Instead, as proposed by Haowei et. al. there is the possibility of incorporating an expansion power cycle. This would utilize regenerative cooling to expand the fuel through various stages of pyrolysis leading to greater power production. However, above all maybe the need to develop versatile materials that can withstand extreme temperatures and heat loads experienced by these aircraft.

3. Methodology

3.1 Innovative Solution

The expansion power cycle utilizing the cracking of hydrocarbon fuel presents an approach toward meeting the power generation and thermal requirements for high-speed vehicles. However, an alternative solution is to use a Rankine cycle system. This approach also incorporates traditional methods of using a fuel heat sink, where fuel is pumped through critical areas of the vehicle, absorbing heat before being burned in the combustor. However, a secondary fluid, water is used to increase the heat sink capacity of the fuel. This takes advantage of the latent heat of vaporization where steam is produced as a byproduct of removing heat from the fuel. Energetic steam is then used to drive a turbine, where mechanical work supplies power to the vehicle using a generator. With the additional cooling provided by the secondary fluid, the temperature of the fuel can be regulated, reducing the potential for undesirable effects, such as fuel coking, and/or reductions in engine efficiency and performance.

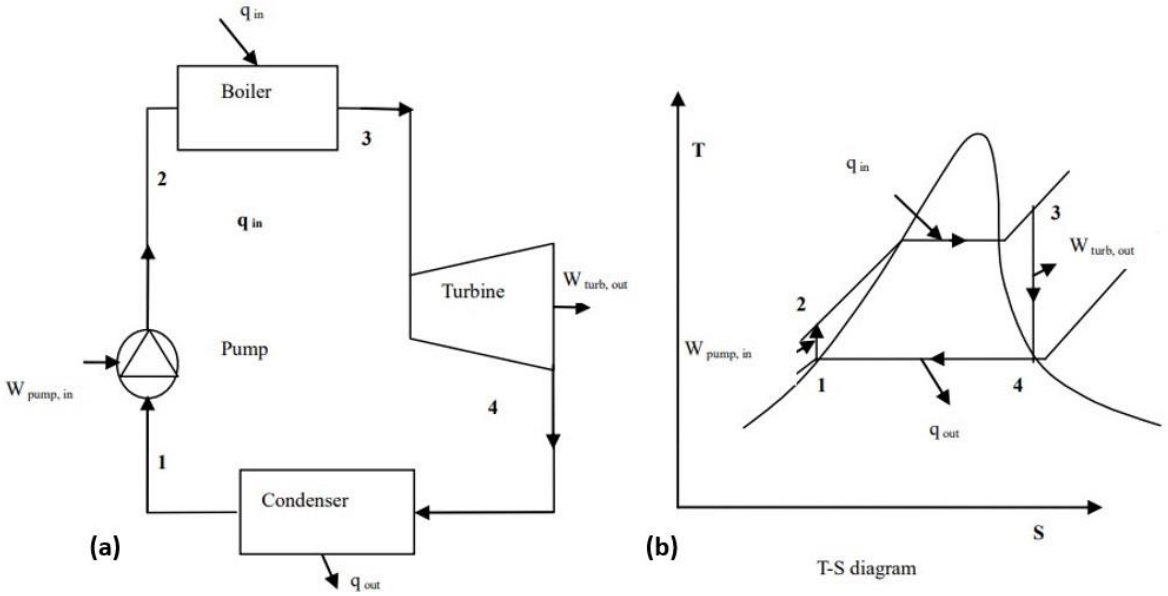

Figure 21: Rankine cycle component diagram (a) and T-S diagram, (b) representing the idealized fluid states used to define actual system performance [6].

3.1.1 Rankine Cycle

A Rankine cycle is an idealized thermodynamic cycle that describes the individual processes by which mechanical work is extracted from a fluid, (usually water) using a specific heat engine, such as a steam turbine.

$$\eta_{thermal} = \frac{W_{out}}{Q_{in}} = \frac{Q_{in} - Q_{out}}{Q_{in}} = \frac{T_H - T_c}{T_H} \quad (10)$$

Like most heat engines, energy is obtained from the working substance as it moves from a heat source to a heat sink where the difference in temperature is used to determine the

maximum theoretical work, as per the Carnot theorem, Eqn. 10. Additionally, the Rankine cycle is often used to evaluate the performance of steam cycle systems.
The four processes of the Rankine cycle include:

- $1 \rightarrow 2$ Isentropic compression, increasing the pressure of the liquid
- $2 \rightarrow 3$ Isobaric heat addition, liquid evaporates
- $3 \rightarrow 4$ Isentropic expansion, fluid energy is converted to mechanical work
- $4 \rightarrow 1$ Isobaric heat removal, fluid condenses

3.1.2 Dual-Mode Rankine Cycle for Aircraft Applications

Thermal power systems convert thermal energy into mechanical work making them particularly useful as a means of power generation for high-speed vehicles due to the extreme heat loads available. Using this approach, waste heat from the vehicle can be converted into electrical energy, cooling the vehicle, and providing power for flight operations. However, a thermal management system based solely on this approach is limited by the enthalpy change across the heat engine. To increase these thermal limits an innovative solution is to employ a dual mode system, incorporating an additional configuration. This is indicated in Figure 22 by the exhaust valve used to regulate the secondary flow path. From the figure, steam is either directed to the condenser, or exhausted to atmosphere, representing the open and closed configurations, respectively. In both configurations, the fuel is used as the heat sink, absorbing heat from critical areas, such as cooling channels that protect the structure from extreme thermal loads.

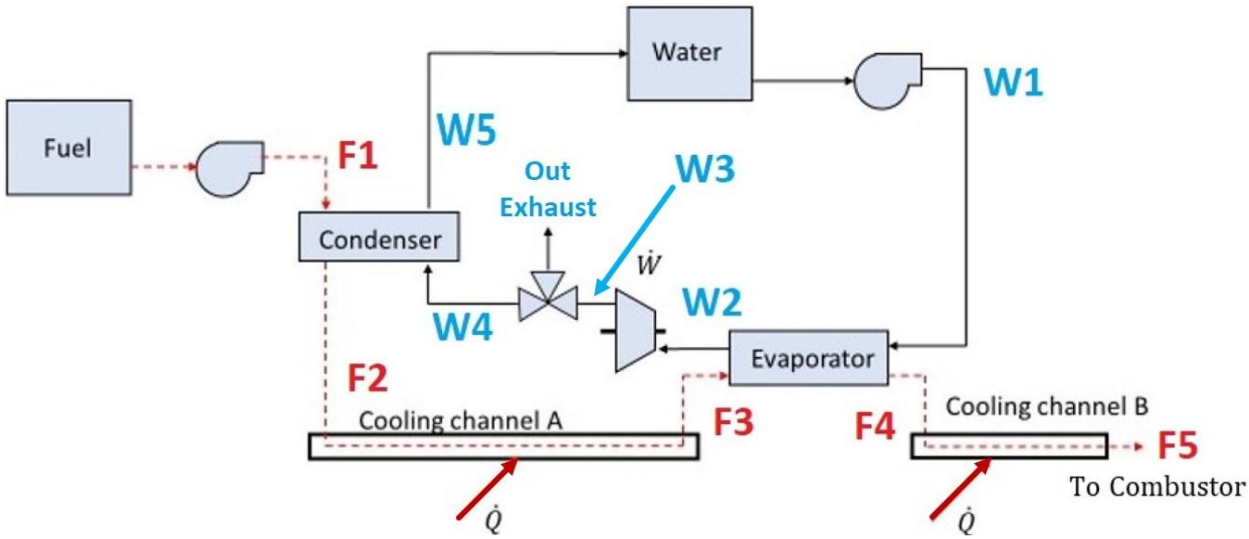

Figure 22: Thermal management diagram, incorporating the dual mode Rankine cycle where fuel is used as a heat sink before being burned in the combustor, adapted from [9].

With the exhaust valve closed, fuel is used as the cold sink, condensing low pressure steam from the turbine. Heat is added to the fuel within the condenser ($\mathbf{F1} \rightarrow \mathbf{F2}$) and removed from the fuel within the boiler($\mathbf{F2} \rightarrow \mathbf{F3}$), resulting in net cooling based on the energetic changes of the fluid through the steam engine. Therefore, the cooling potential of this mode is limited by the efficiency of the expansion device and is only applicable when the fuel is within its enthalpy limits; for example, when a high fuel flow rate is used, providing an

adequate fuel heat sink. However, this configuration is optimal in reducing the overall mass of the system as the secondary fluid is contained within the vehicle.

With the valve open, low-pressure steam is exhausted to atmosphere ($\mathbf{W3} \rightarrow \mathbf{W4}$), rather than being sent to the condenser. This provides a substantial increase in cooling as the fuel is not used as the cold sink. The total cooling potential of this configuration is equivalent to the heat transferred from the fuel to the water in the boiler. This makes it applicable for flight operations when closed configuration does not meet the thermal capabilities of the vehicle. However, in the open configuration all exhausted fluid is lost, increasing the weight requirements needed for continuous operation. Therefore, limiting this configuration is key toward reducing the weight of the TMS.

Figure 22 shows there are two cooling channels with the evaporator placed in between. This increases the cooling capabilities of the system by taking advantage of the cooling provided by the evaporator. In fact, the thermal management system is optimized when the temperature of the fuel is maximum at the exit of each cooling channel. With greater fuel temperature entering the evaporator, a greater temperature difference exists between the fluid and more heat can be removed by the system ($\mathbf{F3} \rightarrow \mathbf{F4}$) via the boiler. Thus, it is ideal for the temperature of the fuel to be maximum at the evaporator inlet, $\mathbf{F3}$. With cooler fuel exiting the boiler, a second cooling channel is placed downstream, where more heat can be added to the fuel. Thus, increasing the overall cooling capabilities of the system. Obviously, cooling is maximized if the fuel exits the channel ($\mathbf{F5}$) at maximum enthalpy. This is just below the coking limit, preventing carbon buildup and ensuring continuous controlled fuel flow. The exact amount of heat divided between these channels is a process of design optimization. It is based on a variety of system parameters ensuring the system meets the requirements of the aircraft while minimizing weight. This is discussed in more detail in section V. Vehicle Level Modeling.

Optimizing the system becomes difficult with sudden changes in flight situations. This is when transient effects become important in reducing the weight of the TMS, specifically by reducing the amount of water needed to meet the thermal requirements of the aircraft. The closed configuration does not exhaust water and is therefore optimal in managing water mass. However, the open configuration provides greater cooling. Thus, it is advantageous to develop a system that meets thermal requirements during all operations but limits the exhausted water. An innovative solution is to develop a modular system that exhausts only a portion of the steam needed to ensure the fuel is within its enthalpy bounds. Steady state results can be used to determine the precise position of the valve for a given flight situation; however, when the flight situation is changing the optimal position adjusts with time. Therefore, the response of the system must be observed through this transition to determine the trend representing valve position. This will provide the required information to estimate the weight of the TMS for a given mission profile.

3.2 Experimental System

An experimental system based on the dual-mode Rankine is used for studying thermal management and power generation capabilities, with a focus on transient system dynamics.

3.2.1 System Description

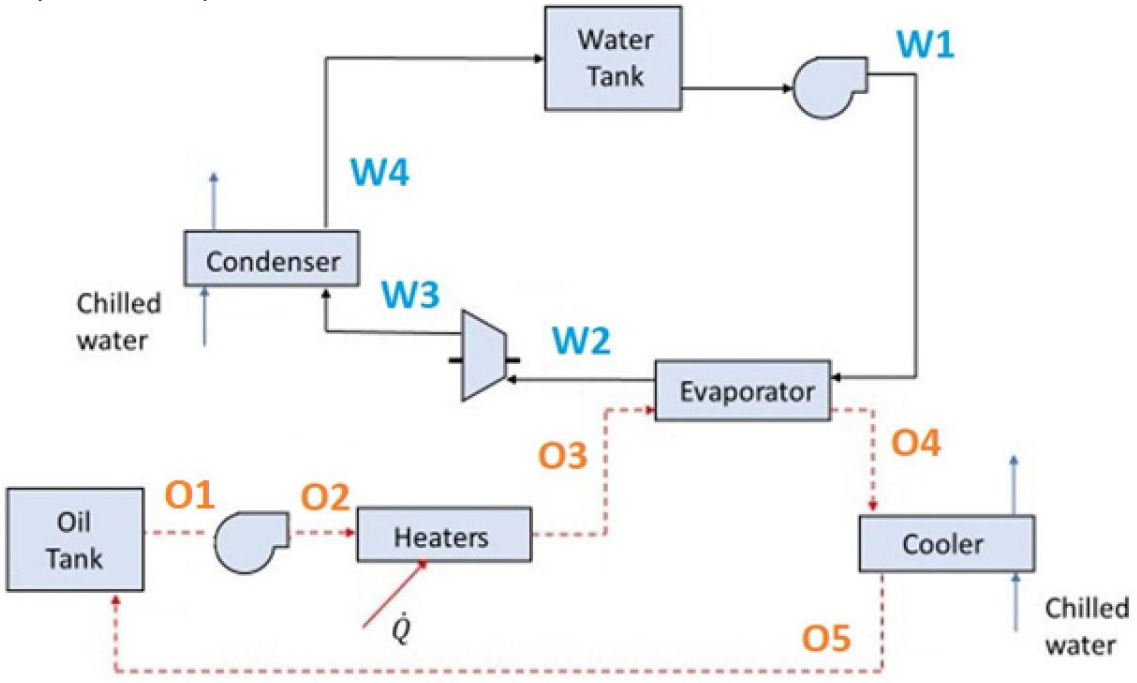

Figure 23: Diagram representing rig components and fluid flow processes, adapted from [9].

Many of the same operating principles exist between the aircraft TMS, Figure 22, and experimental system, Figure 23. However, there are differences in the operational parameters and flow configurations for practical purposes of the lab scale system. Specifically, the thermal loads, flow rates and temperatures are not equivalent to the aircraft TMS. Primarily this reduces cost and increases safety of the experimental system. There are also discrepancies in the flow configurations. A key difference is the thermal fluid flow path where the Aircraft TMS incorporates *fuel* in an open loop, and the rig utilizes *oil* in a closed loop. For the vehicle, cool fuel is continuously drained from the tank and heated as it flows through the cooling channels before being burned in the combustor. However, in the lab scale system, heat is supplied to the oil using resistance heaters and cooled within the evaporator and oil cooler before returning to the heaters. Overall, this closed oil configuration enables a relatively low storage of oil and reduces the power requirements needed to regulate oil temperatures.

Another modification made to the system is the cold sink used within the condenser during closed loop operation. For the aircraft TMS, fuel is drawn from the tank and used to cool low pressure steam within the condenser. This works well for cooling applications as the fuel is initially of low enthalpy. However, in the experimental system, the oil is at a much higher temperature, making it ill-suited for a cooling medium. Thus, instead chilled water is used. This not only condenses the steam but also ensures the water temperature in the tank stays relatively constant. This enables the system to reach a steady state which is required to characterize the individual components.

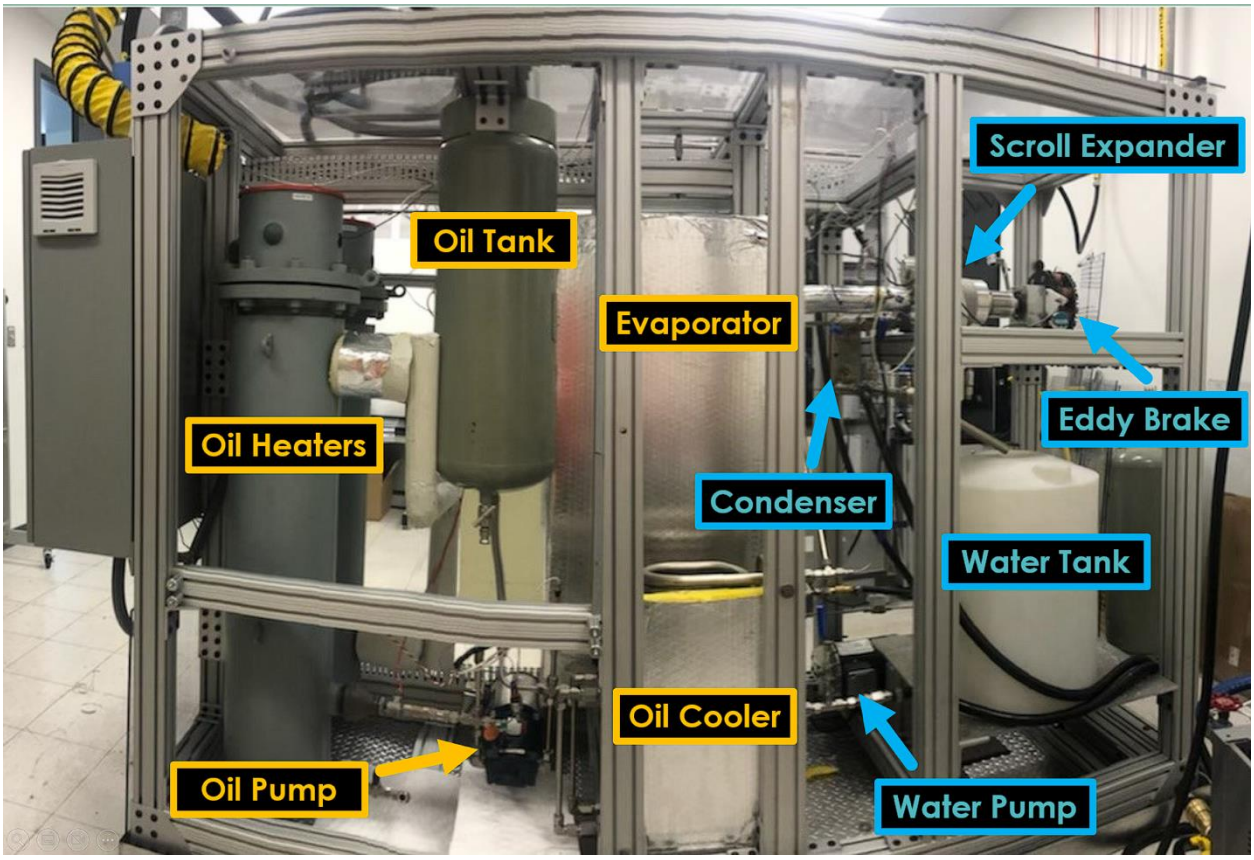

Figure 24: Experimental rig replicating the open cycle of the Rankine cycle system.

The preliminary experimental system is shown in Figure 24. Noting the configuration of the oil loop, the required pressure differential is provided via a gear pump forcing the fluid through the heater inlet (bottom). The oil then flows upward, exiting at the top where plumbing directs the flow to the base of the second oil heater, where it again travels upward, exiting near the top. The now hot oil is directed through the evaporator where it cools before flowing into the oil cooler and back to the pump, completing the cycle. For typical operations, oil does not enter or exit the tank and instead provides sufficient head pressure for pump operation.

Observing the working fluid loop, room temperature water is drawn from the tank via a piston pump, forcing the fluid through the evaporator, producing high-pressure steam. The fluid is then directed through the scroll, expanding the steam before entering the condenser. After exiting the condenser, the liquid water is plumbed to the top of the water tank that is open to atmosphere. As discussed previously, chiller water is first used to condense the low-pressure steam in the condenser and is then used to cool the oil in the oil cooler. The description of these process loops provides a general reference for the design of the experimental system; however, the individual components are discussed in more detail below.

The oil tank is a 30-gallon ASME-code expansion tank with a maximum temperature and pressure of $232\ ^{\circ}\mathrm{C}$ and $150\ \mathrm{psi}$, respectively. This component does not replicate the vehicle TMS but instead ensures an adequate supply of oil. A constant head pressure of nitrogen ($20\ \mathrm{psi}$) is supplied to the tank reducing the development of air pockets. This increases

confidence in the measured oil flow rate as air pockets can disturb flow estimates. A Cox dual turbine flow meter is used to measure the volumetric flow rate. It is calibrated to 4.34 cS and within the specified uncertainty (± 0.10 %) for fluids less than 9.34 cS. It has a maximum operational temperature of 165 °C and a range of flow rates from $0.095 \rightarrow 11.40$ lpm. Providing the required pressure differential is a Haight gear pump with a max capacity of 3 GPM. Two identical 30 kW Watlow resistance heaters are placed in series (60 kW total) replicating the thermal load on an aircraft. However, the bus bar limits the power supplied to the system to $30\ kW$; thus, the maximum capabilities of these heaters are not achieved. Following the heaters, the oil is directed through the evaporator.

The evaporator is a critical component for the power production and cooling capabilities of the system. Using a counterflow arrangement, hot oil is used to superheat liquid water where it undergoes phase transition from liquid to liquid-vapor to purely vapor. During the expansion, the pressure of the fluid is increased primarily due to the scroll expander obstructing the flow path upstream. The original evaporator consists of four semi-helical tube-in-tube heat exchangers (TTHX) manufactured by Exergy Heat Transfer Solutions (model no. AS-00528). It is constructed of 316L stainless steel, with a heat transfer surface area of 0.24 m^2. The original oil cooler was composed of the same tube-in-tube heat exchangers; however, only two were needed to ensure the oil temperature was within the operational range of the pump and flow meter. Using a counter flow arrangement cooling water exiting the condenser provided additional cooling to the oil.

The critical components of the water loop include the tank, pump, evaporator, scroll expander and condenser. For the original system, a three-cylinder piston pump with a maximum capacity of 3 GPM was used to draw water from the 22 Gal. polyethylene tank. However, this pump was found to produce pulsatile wave patterns resulting in overpredicted flow rates. Thus, the pump was replaced by a progressive cavity pump to provide a more constant flow. The cavity pump has a maximum capacity of 0.455 GPM. After exiting the pump, water is forced through the flow meter before entering the evaporator. An Omega brand turbine flow meter measures the volumetric flow rate with an uncertainty of ± 2.64 mGal/min. After exiting the evaporator high-pressure steam is directed to the scroll expander.

The scroll expander is a critical component in quantifying power generation and cooling capabilities of the system. It was selected due to its versatility and poses a respectable efficiency near 70 %. This device works very similar to kinetic turbines. Energy is extracted from a high-pressure, high-temperature vapor, producing work and mechanical energy. However, unlike kinetic turbines, progressive cavity machines are better suited for this application, mainly due to their comparatively lower rotational speeds and clearance requirements. These attributes reduce manufacturing costs considerably and lead to a more robust design, tolerating lower vapor quality levels, and higher pressures [31]. This results in greater reliability for most small-scale systems.

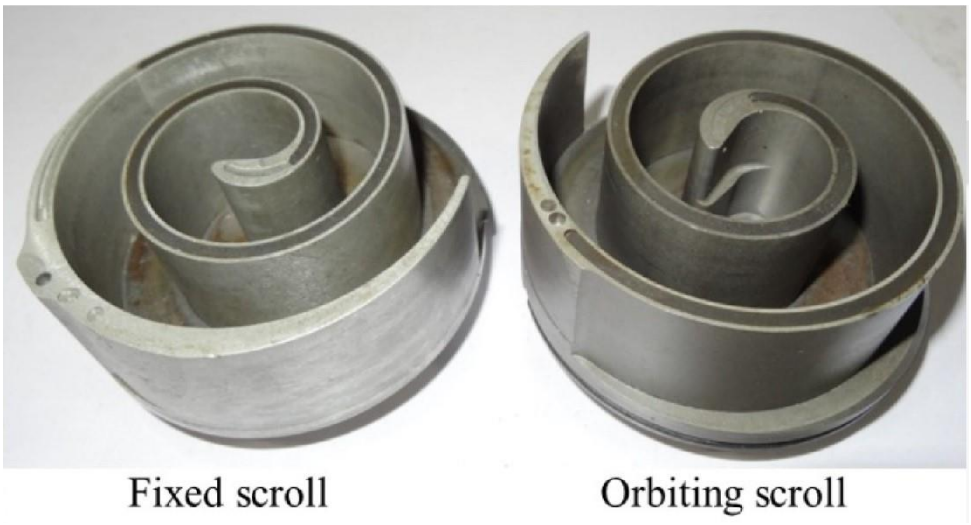

Figure 25: Illustration of scroll expanders inner geometry [29].

As shown in Figure 25, the inner geometry is comprised of two spiral shaped scrolls that are of similar size and shape mirrored or inverted across the horizontal. The structure of these scrolls is created using an involute profile. This geometry is easily described as a single line traced out by the end of a string when unwound from a circle.

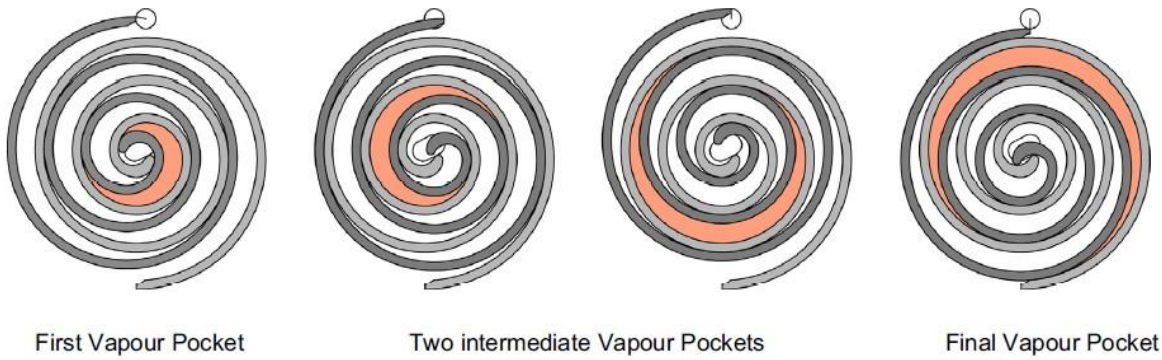

Figure 26: Diagram showing the orbital motion of the scroll expander traced by a virtual circle [30].

The circular motion of the device is shown in Figure 26. One scroll orbits while the other is stationary. This ensures the scrolls are in contact at some points, sealing the vapor pockets within. As the scroll moves, fluid is drawn through the suction port (center), filling the first vapor pocket. After a single orbit the filling process is complete and the first vapor pocket travels to the periphery. In other words, the vapor pocket is no longer in contact with the suction port. Additionally, all subsequent vapor pockets continue to expand as they also move to the periphery during the same motion. The vapor is then discharged outside the mechanism thereafter. The three flow processes through the device are suction, expansion and discharge.

The scroll expander utilized for this study is manufactured by Airsquared (model E15H022A-SH) rated for a standard output of 1KW of power, with a volumetric efficiency of 3.5. Recommended fluids are air, carbon dioxide, natural gas, and most refrigerants. Typically, refrigerants are used as the working fluid; however, using steam as the working fluid alleviates environmental concerns during open cycle operations when steam is exhausted to the atmosphere. Using steam presents challenges as a working fluid where high temperatures increase corrosion and limit bearing life. However, modifications have been made to the bearing seals, increasing the operation temperature. With steam as the working fluid, maximum operation temperature is $175\ °C$. Adhering to manufacture recommendations and monitoring bearing health will ensure the long life of the scroll expander.

An Eddy brake controls the speed of the scroll and determines the mechanical power. The Eddy brake is freely attached to the shaft where electrically induced coils apply a counter torque, controlling its speed. The brake is fixed to a strain gauge via a moment arm that records the measured force needed to estimate torque. An optical sensor measures the shaft speed so scroll power can be calculated.

Shown in Figure 24, compression tubing made from 316 stainless steel is used for plumping. For the water loop, pipe diameters vary from ¼ inch at the pump outlet to 1 inch at the scroll outlet. While $1/2$ inch piping is primarily used for the oil loop. Additionally, stations are placed between each active component, estimating the state of the fluid. These are measured using E-type thermocouples and pressure transducers with an uncertainty of $\pm 0.5\ °C$ and ± 0.4 psi, respectively. Thus, pressures and temperatures are used to estimate the state of the fluid. This leads to complications in estimating properties for two-phase fluids as pressure and temperature remains constant across the vapor dome despite a change in state. However, as will be discussed in section 4.3.2 Corrugated-Plate Analysis) an energy balance within the evaporator estimates fluid state for two-phase fluid when thermal losses are small.

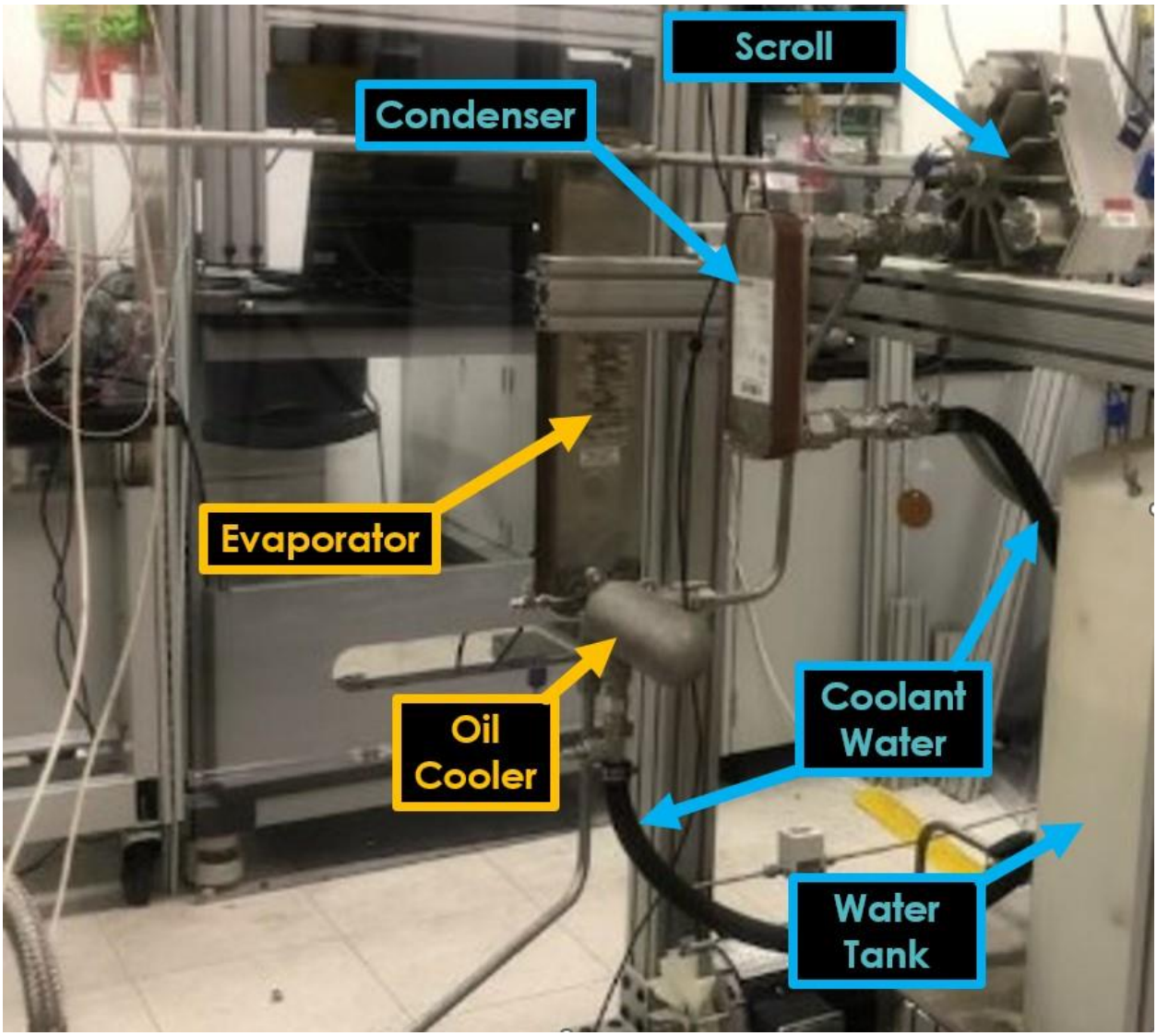

Figure 27: Experimental system showing the newly installed evaporator and oil cooler.

The primary purpose of the experimental system is to investigate the capabilities of the Rankine cycle system for high-speed aircraft applications. However, it also serves as a test bench to evaluate the capabilities of individual components. Thus, various attributes can be evaluated and compared (e.g., weight, volume, performance, etc.) to determine the most appropriate design to be implemented in the system. Therefore, various components will be introduced into the system with the eventual aim of a scaled representation of the aircraft TMS.

The evaporator is a key component in estimating the power generation and cooling capabilities of the system. Thus, it is advantageous to evaluate different heat exchangers. As discussed above the initial evaporator consisted of four helical tube-in-tube heat exchangers placed in series with dimensions $80 \times 11 \times 7.5\ \text{in}^3$ and total weight of $42.8\ \text{kg}$. This component was shown in Figure 24 encased in fiberglass insulation. However, there are other

heat exchangers available that are more suitable for aircraft applications. Such as the corrugated plate heat exchanger (CPHX) indicated as the evaporator in Figure 27. This component is both lighter and occupies less volume than the TTHX with dimensions $21 \times 1.6 \times 4.4\ \mathrm{in}^3$ and weight of $5.7\ \mathrm{kg}$. However, it offers a near equivalent heat transfer area at $0.84\ \mathrm{m}^2$, only about 10% less than the TTHX. Therefore, the performance of the CPHX is evaluated and compared with the TTHX. Additionally, as shown in Figure 27, the oil cooler has also been replaced by a shell-in-tube heat exchanger (STHX). The oil cooler is not a critical component of the aircraft TMS and only serves to regulate the oil temperature. However, the chiller offers a high water flow rate that is beneficial in characterizing these heat exchangers. In fact, the chiller loop has been used to determine all liquid-liquid heating for each heat exchanger, using water. This process is discussed in more detail in the appropriate heat exchanger subsections.

IV. Model Development

The experimental system presented above was used to model critical components of the system. This includes the various heat exchangers, including, the evaporator, condenser, and the oil cooler, as well as, the power extraction devise, i.e., the scroll expander. Of the components in the Rankine cycle system, the heat exchanger is very complex, and an accurate accounting of the fluid thermal effects must be represented between the different fluid phases while being true to first principles. However, the range of these models can only be defined based on the operating range of the experimental system, confining their applicability to the specific input parameters (e.g., flow rates, temperatures, and pressures) used during testing. Therefore, to ensure these models are within their quantified accuracy, model inputs must be within the capabilities of the experimental system. The development of the component models will be described and their comparison to the experimental data will be presented.

4.1 Heat Exchanger Modeling Strategies

In the literature, various heat exchanger modeling strategies are employed to capture the physics associated with vapor compression systems. Like the Rankine cycle, these physical systems rely on a condenser and evaporator to transfer heat between the working fluid and exterior medium. Two methods commonly employed are moving boundary (MB) and finite volume (FV) models. These represent different ways of discretizing the heat exchanger as fluid properties (temperatures, viscosity, conduction coefficients) change through the device, thus affecting heat transfer.

The finite volume approach, shown in Figure 28 (a) discretizes of the overall volume into fixed regions. This allows for the phase and properties to be assumed constant through each one. The physical accuracy increases as the size of each individual volume becomes very small, approaching a differential volume. The models fidelity is therefore directly related to computational cost, where greater accuracy is produced due to the smooth integration of conservation laws across the boundaries. For both FCV and MB models, the conservation laws include conservation of mass, momentum, and energy. However, with the assumption of constant pressure, the conservation of momentum can be dropped, simplifying the set of equations. This is valid when the pressure drop is small, resulting in negligible change of state through the device. This was found to be true for the experimental system; however, pressure loss may become more apparent during refinements in aircraft design, in which this assumption may no longer be valid.

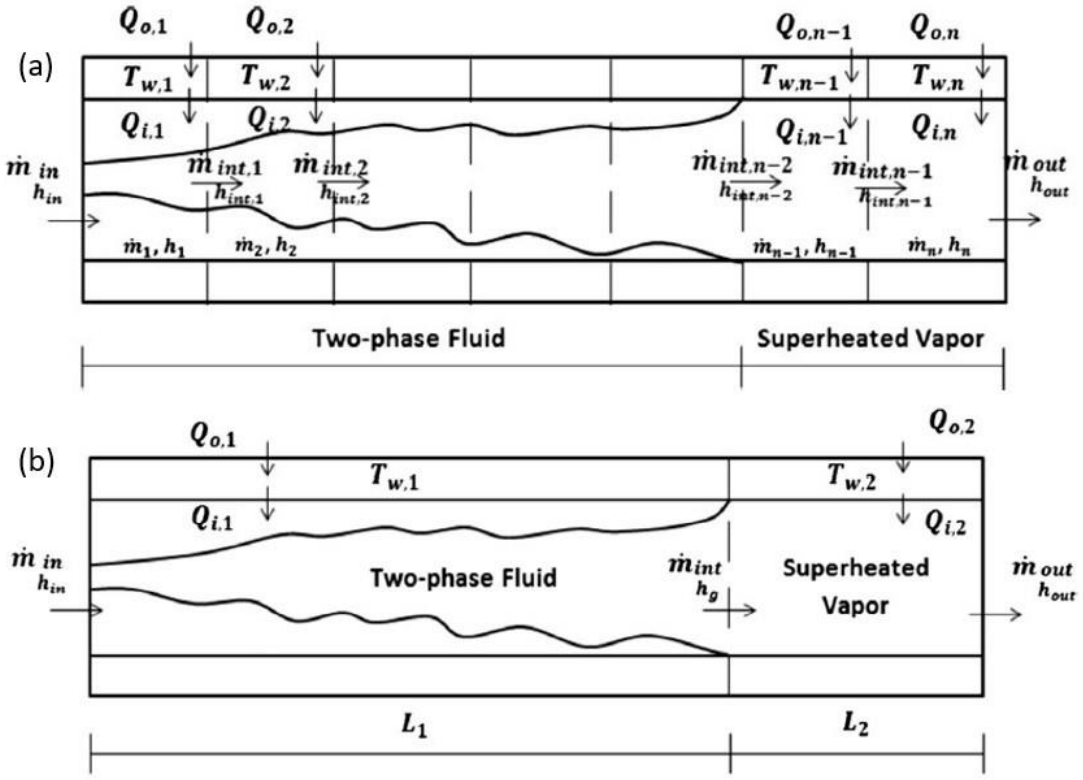

Figure 28: Discretized heat exchanger geometry for the finite control volume (a) and moving boundary (b) models including parameters associated with mass and energy conservation [8].

Unlike the FCV, MB models discretize the heat exchanger based on the number of phases present, Figure 28 (b). For the case of the physical evaporator and the condenser devices, MB models would form a maximum of three separate regions, allowing for an accurate physical representation of the heat transfer within the subcooled liquid, two phase, and superheated zones. This results in lower computational cost, on the order of three magnitudes, compared to FCV schemes [7]. However, there is the added complexity of locating the interface between phases due to the dynamic nature of the phase boundaries. This gives basic significance to the term moving boundary, as the boundaries move within the control volume. As discussed by Smit [7] this leads to FCV being more robust due to the homogenous assumption employed where only one phase domain exists in each control volume, and thus the phase boundary always exists between two finite volumes. Additionally, in cases where phases disappear and reappear, such as during startup and shutdown, additional techniques must be employed to ensure there are no discontinuities in the laws of conservation for MB models. For example, in a shutdown event where the superheated region eventually disappears the series of equations fail; therefore, strategies must be employed to make the switch from conservation laws to tracking equations that determine when the nonexistent phase is becoming active. As discussed by Smit [7] various thermodynamic properties can be used to determine the onset of the switch, including void fraction, two-phase density, two-phase region length, and enthalpy. Many of these switching schemes must also employ a minimum length threshold to ensure

code stability by preventing the continual disappearance and reappearance of a phase domain, known as chattering. For these cases, FCV models are often used as a form of validation in the development of the MB models to ensure a stable scheme strengthening the notion that FCV models are more robust. As discussed below, both FCV and MB modeling strategies can be employed using MATLAB/Simulink software.

The MATLAB/Simulink library browser contains Simscape subset models which are component blocks that enable the rapid creation of dynamic models. In the fluids library, built-in heat exchangers can be used to model an extensive array of heat exchanger geometries incorporating different fluid mediums. They also include additive physical effects such as fouling and fin effectiveness.

In the two-phase thermal-liquid domain, a single built-in heat exchanger utilizes the MB approach where the subcooled liquid, two phase, and superheated zone lengths are tracked and can be displayed through an output port. This component quantifies the heat transfer between a single-phase liquid and a two-phase fluid. Input geometry and additional heat transfer aspects discussed above can be keyed into the users setting dialog box; however, modifications to source code is not possible due to proprietary restrictions placed on the component. Fortunately, these restrictions are not enforced on simpler Simscape heat transfer blocks such as two-phase and thermal liquid heat pipes. These, along with other thermal blocks, can be used to create custom heat exchanger models. For initial model development the FCV approach is found to be favorable as it does not require phase boundary tracking and is therefore easier to implement. So, the MB approach will not be used.

Many built-in heat exchangers within Simulink utilize the effectiveness-NTU analysis method, which is a preferred approach compared to the log mean temperature difference (LMTD) technique. For single phase heat exchangers, the LMTD method requires an iterative procedure if the outlet temperatures are unknown; however, for these situations the NTU method does not require such iteration. However, for multiphase heat exchangers incorporating a counter flow arrangement, a process of iteration must still be utilized, independent of the chosen modeling scheme. This configuration is utilized for modeling the physical evaporator and condenser within the experimental rig and as such an iterative procedure must be used in the solving procedure. The exact details of how this iterative procedure is scripted is presented.

$$\varepsilon = \frac{\dot{Q}}{\dot{Q}_{max}} \tag{11}$$

The effective-NTU method relates the actual heat transfer rate with the maximum possible heat transfer rate, Eqn. 11. This maximum presents the hypothetical case where the fluid of lower heat capacity rate experiences the maximum possible temperature difference, Eqn. 12.

$$\dot{Q}_{max} = C_{min}(T_{h,i} - T_{c,i}) \tag{12}$$

This heat transfer rate is theoretically possible in a counterflow heat exchanger of infinite length where the minimum heat capacity rate is calculated using Eqn. 13.

$$C_{min} = \min(C_h, C_c) \tag{13}$$

Eqn. 12 can be proved by simply noting that if the maximum heat capacity rate was utilized this would result in a violation of energy conservation as the heat transfer rate is limited by the temperature difference.

$$\dot{Q} = C(T_{out} - T_{in}) \tag{14}$$

Furthermore, the actual heat transfer can be calculated using the product of the temperature change and heat capacity rate of either fluid, assuming the heat exchanger is insulated from the environment. This of course requires that the outlet temperatures are known, the very properties that the NTU method sets out to solve.

$$\varepsilon = f\left(\text{NTU}, \frac{C_{min}}{C_{max}}\right) \tag{15}$$

It can be determined that the heat exchanger effectiveness is a function of the number of transfer units (NTU) and the ratio of the heat capacity rates, Eqn. 15. With this relation the actual heat transfer rate can then be determined despite no knowledge of the exit temperatures. The exact equation is commonly tabulated in most undergraduate heat transfer textbooks and is dependent on the type of heat exchanger and/or flow configuration.

$$\varepsilon = \frac{1 - \exp[-\text{NTU}(1 - C_r)]}{1 - C_r \exp[-\text{NTU}(1 - C_r)]} \tag{16}$$

For a concentric tube heat exchanger with a counter flow arrangement Eqn. 16 represents the relation where C_r is the ratio of heat capacity rates. This equation is developed by first applying an energy balance to differential elements between the hot and cold fluids under the following set of assumptions taken from Frank and David [11].

1. The heat transfer is insulated from surroundings

2. Axial conduction along the tubes is negligible.

3. Potential and kinetic energy changes are negligible.

4. The fluid specific heats are constant.

5. The overall heat transfer coefficient is constant.

$$\frac{T_{h,out} - T_{c,out}}{T_{h,in} - T_{c,in}} = \exp[-NTU(1 + C_r)] \tag{17}$$

This results in Eqn. 17 where NTU is a dimensionless parameter that relates the potential for the difference in temperature between the hot and cold fluid to cause a temperature change in the fluid of lower heat capacity rate, Eqn. 18.

$$\text{NTU} = \frac{\text{UA}}{C_{min}} \tag{18}$$

Here, the overall heat transfer coefficient, U is often found empirically and is specific to the heat exchanger and fluids utilized. Some common heat exchanger designs are shown in Figure 29 showing a wide range of values for each combination. However, rather than using these, it is often more advantageous to seek refined film coefficients from the literature.

Fluid Combination	U **(W/m^2 · K)**
Water to water	850–1700
Water to oil	110–350
Steam condenser (water in tubes)	1000–6000
Ammonia condenser (water in tubes)	800–1400
Alcohol condenser (water in tubes)	250–700
Finned-tube heat exchanger (water in tubes, air in cross flow)	25–50

Figure 29: Overall heat transfer coefficient for different heat exchanger designs [11].

Using temperature relations for counterflow heat exchangers, the left side of Eqn. 17 can be written in terms of the heat exchanger effectiveness and the ratio of heat capacity rates, resulting in the final equality shown by Eqn. 16 (This provides a brief description of the derivation of Eqn. 16, for a more complete explanation see Kays [10]). Therefore, with all the variables on the right side of Eqn. 18 known, the effectiveness-NTU relation can be used to equate the heat transfer rate for a basic liquid-liquid heat exchanger. However, in the case of two-phase flow, multiple heat transfer zones exist within the physical device where the heat flux changes. This is represented in Figure 30 where each phase represents a different control volume. Therefore, the process of obtaining the final outlet properties is more complex, in that each region must be solved sequentially. Stating this explicitly, for parallel flow the results found for each control volume are used to solve the outlet properties for the successive region

downstream. Counterflow, on the other hand, adds additional complexity since there are fewer known values at station one, Figure 30. Therefore, the initial heat transfer rate must be assumed and, as a result, the process must be iterated until the initial predictions converge to the true value. This is the flow configuration for the evaporator where hot oil is used to produce steam.

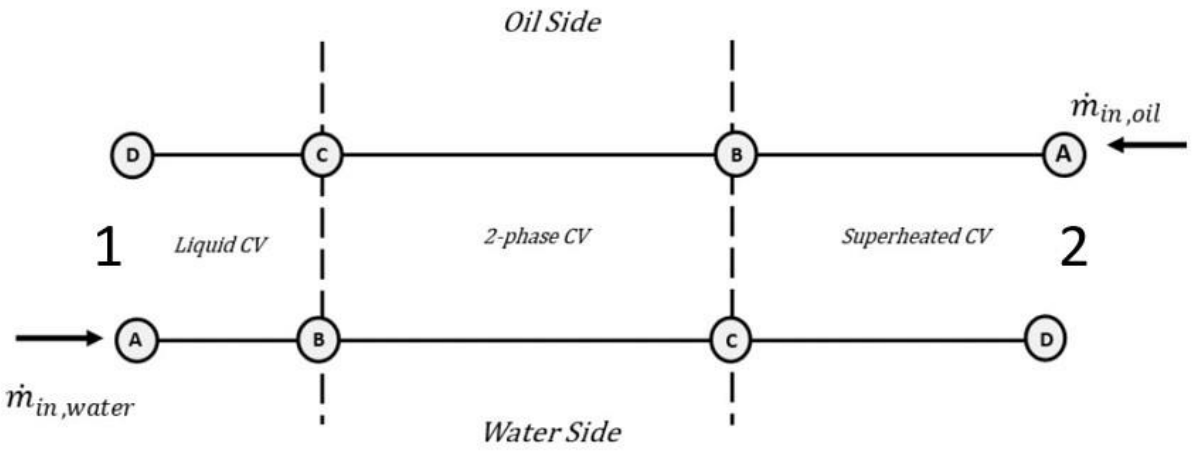

Figure 30: Heat exchanger nodes, referencing the location of the water side phase boundary where variation in heat transfer exist [9].

In a two-phase heat exchanger, such as an evaporator or condenser, the heat transfer rate in the two-phase region can be determined based on the enthalpy of vaporization and mass flow rate, Eqn. 20. However, because the inlet fluid phase is different between these devices, entering as a condensed liquid in the evaporator, and as a superheated vapor in the condenser, the heating rates that can be determined are different. For the evaporator, the subcooled heating can be determined and for the condenser the superheated heat transfer can be determined. This of course assumes constant pressure, confining the state path to a particular endpoint. For the case of the evaporator, the heat transfer rate in two regions can be solved using Eqns. 19 and 20, respectively. (The effectiveness-NTU method described below only applies to an evaporator. However, the same methodology can be used to model a condenser with superheated vapor at inlet. See Appendix B for the effectiveness-NTU method applied to the condenser.)

$$\dot{Q}_{sc} = C_{min}\left(T_{c,A} - T_{c,B}\right) \tag{19}$$

$$\dot{Q}_{2p} = \dot{m}_w h_{fg} \tag{20}$$

The difficulty, however, is associated with determining the maximum heat transfer rate, as the oil temperatures at nodes B, C and D are unknown. Therefore, it is advantageous to first

presume the outlet state of the oil, at node D. This prediction can be made more accurate by noting that the oil is the only medium providing heat; thus, all the heat absorbed by the water was evidently lost by the oil, allowing for a more accurate prediction given by Eqn. 21 where C_{max} references the heat capacity rate of the oil.

$$T_{h,D} < T_{h,A} - \frac{\dot{Q}_{sc} + \dot{Q}_{2p}}{C_{max}} \tag{21}$$

Using the calculated heat transfer rates from the subcooled and two-phase control volumes, the oil temperature at node D must satisfy Eqn. 21. Continuing upstream, with the subcooled liquid heat transfer rate known, and a thermal loss term obtained from experimental results the oil temperature at node C can be defined, Eqn. 22.

$$T_{h,C} = \frac{\dot{Q}_{sc} + \dot{Q}_{loss,CD}}{C_{max}} + T_{h,D} \tag{22}$$

This temperature $\left(T_{h,C}\right)$ is then used to equate the maximum heat transfer in the subcooled domain using Eqn. 12, giving a value to the heat transfer effectiveness. This is then used to solve for the number of heat transfer units, using Eqn. 16.

$$A = \pi D L_i \tag{23}$$

Therefore, with the heat transfer area defined, Eqn. 23, the length of the subcooled region, L_{sc} can be calculated, as all other variables in Eqn. 18 are known. This will become useful for determining how well the initial temperature was predicted. However, the length of the two-phase and superheated regions must be calculated before any conclusions can be made. Fortunately, with the state of the oil at node C defined, the temperature at node B can be determined using a similar procedure as described above where the heat transfer rate and thermal losses are used to determine the temperature of the oil downstream.

$$T_{h,B} = \frac{\dot{Q}_{2p} + \dot{Q}_{loss,BC}}{C_{max}} + T_{h,C} \tag{24}$$

Using Eqn. 24 the temperature at node B can be calculated. With this known the heat exchanger length for the two-phase region can be calculated using the same procedure discussed above i.e., Eqns. 11, 16, 18, and 23. This process is used to find the superheated length as well. With the temperature of the oil at node A given, the heat transfer rate can be determined by subtracting the thermal losses within the superheated domain, shown by Eqn. 25

$$\dot{Q}_{sh} = \dot{Q}_{h,AB} - \dot{Q}_{loss,AB} \tag{25}$$

This heat transfer rate can then be used to calculate the temperature of the superheated steam at the outlet of the evaporator using Eqn. 26.

$$T_{c,D} = T_{sv} + \frac{\dot{Q}_{sh}}{C_{min}} \tag{26}$$

However, this is only correct if the sum of all heat exchanger lengths equals the total length of the heat exchanger, where each individual length is determined using the process discussed above.

$$L_{sl} + L_{2p} + L_{sh} = L \tag{27}$$

If Eqn. 27 is not satisfied the entire process repeats where a new value is assumed for the outlet temperature of the oil. Computational cost can be reduced by utilizing a successive approximation method such as the secant method. See Appendix A for the full list of equations and for script development.

4.2 Oil Cooler Modeling

The purpose of the oil cooler (shown in Figure 31) ensures temperatures are within the operating conditions of the flow meter and pump. From the cross-section in Figure 31 (b), the oil cooler is a shell and tube heat exchanger composed of 13 inner tubes with 4 shell-side baffles. It is made of stainless-steel with a weight of $1\ \mathrm{kg}$. Chiller water flows through the inner tubes and oil flows through the outer shell. This flow configuration was found to increase heat transfer which can be attributed to the shell side baffles that enhance heating for low Reynold flows [12]. During operation oil flow rates are nearly a magnitude less than the coolant water leading to a large discrepancy in Reynolds numbers with $\mathrm{Re}_{\mathrm{oil}} \approx 3000$ and $Re_{coolant} \approx 9000$. Therefore, if the configuration was reversed, where coolant was pumped through the outer

shell the heat transfer effectiveness would be reduced as the coolant is more turbulent and therefore less responsive to flow enhancements. This was confirmed experimentally.

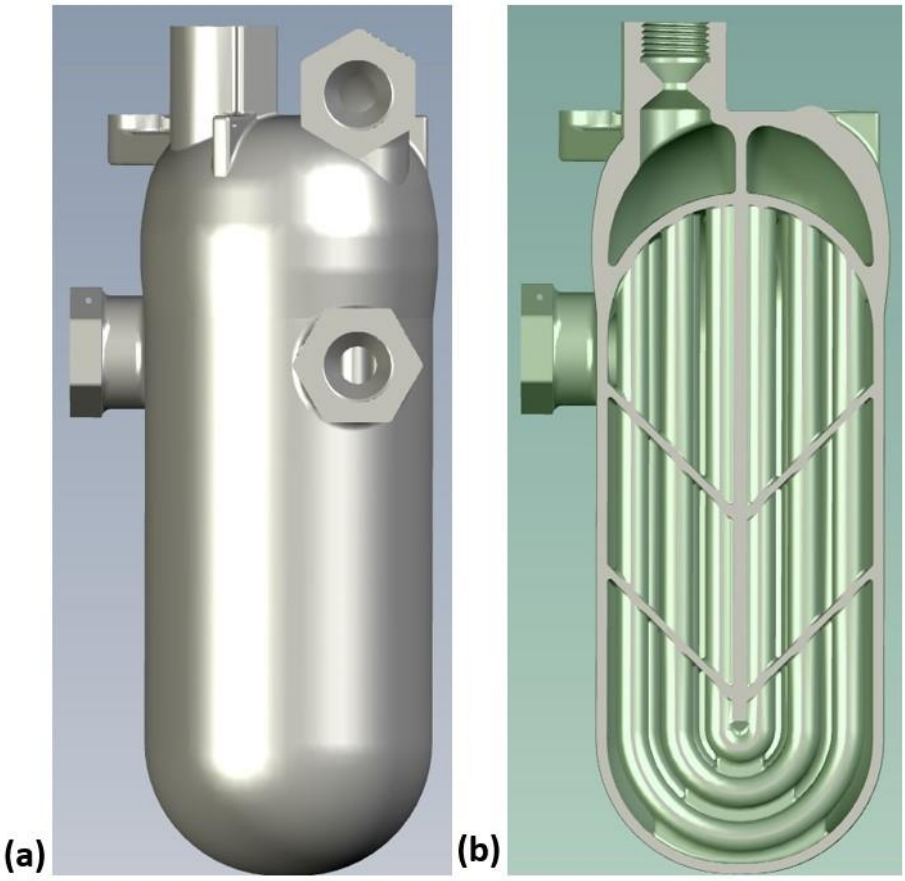

Figure 31: AMHX Geometry (a) and cross-section (b)

Accurately modeling the oil cooler is critical in developing a model that can predict capabilities of the experimental system. Inaccurate heating estimates lead to misrepresented fluid states upstream and because the oil loop is closed these discrepancies will cascade

through every component in the circuit. With the temperature difference as a driving force for heat transfer this in turn affects cooling potential and power estimates of the system.

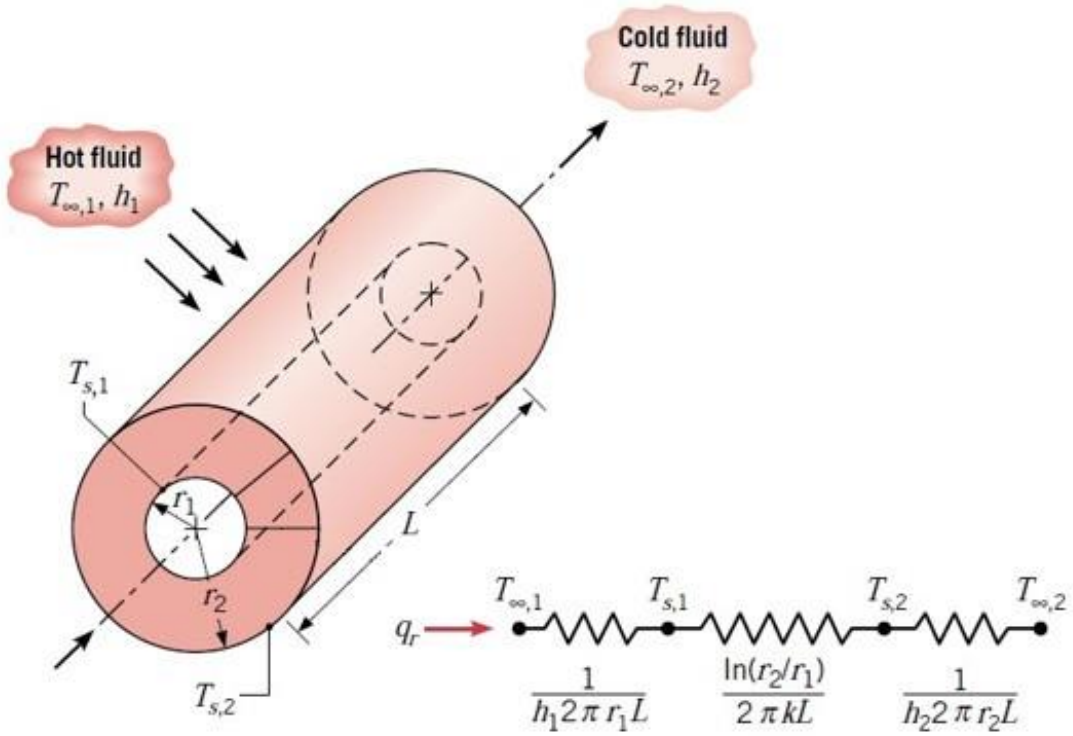

Figure 32: Heat transfer through a pipe referencing the thermal resistance concept [11].

$$R_{ov} = \frac{T_{lm}}{Q} = R_1 + R_w + R_2 \tag{28}$$

$$R_1 = \frac{1}{h_1 2\pi\, r_1 L} \tag{29}$$

$$R_w = \frac{\ln(r_2/r_1)}{2\pi k L} \tag{30}$$

$$R_2 = \frac{1}{h_2 2\pi\, r_2 L} \tag{31}$$

Shown in Figure 32, heat transfer within a heat exchanger can be modeled using the thermal resistance concept. This quantifies the ability of a substance to resist the transfer of heat for a given temperature difference. Within the heat exchanger, the overall resistance can be described as a sum of the individual resistances within the device. Assuming negligible fouling these are associated with convection heating between the hot and cold fluid and resistance of the wall. This is modeled using Eqns. 29 through 31. With the overall resistance calculated experimentally using Eqn. 28, convective resistance of one fluid can be used to

predict the convective resistance of the other. This idea follows the notion that all variables are resolved since the number of unknowns and equations are equal. Using this approach thermal resistance can be determined empirically even when the flow geometry is complex, such is the case for the shell side of the oil cooler.

With circular pipe flow well documented in the literature, heat transfer can be estimated for the coolant side of the oil cooler. Therefore, with this convective resistance known, the method described above was used to determine oil-side resistance.

$$\mathrm{Nu}_2 = 0.023\mathrm{Re}_2^{0.8}\mathrm{Pr}_2^{n} \tag{32}$$

The convective heat transfer within the inner tubes (coolant side) is represented by the Dittus-Boetler equation (Eqn. 32). This correlation assumes fully turbulent flow where $n = 0.4$ for heating, or $n = 0.3$ for cooling. Using the definition of the Nusselt number the coolant side convective heat transfer, h_2 can be determined and used to equate the oil side resistance.

$$\mathrm{Nu} = \frac{h}{k/L} \tag{33}$$

The Nusselt number, Eqn. 33, is a dimensionless parameter that relates the convective to conductive heat transfer across the fluid boundary. In this equation L is the characteristic length, commonly referenced as the hydraulic diameter (D_h) for channel flow. Therefore, with this parameter known the convective heat transfer coefficient, h, can be determined for a given fluid and channel geometry.

It must be noted that the resistance of the pipe wall can be isolated to provide a more accurate determination of the oil convective resistance; however, it was left incorporated as a sum between the resistance of the oil and resistance of the pipe wall. This approach produces no reduction in the models ability to predict overall heating and only increasing the convective resistance of the oil in magnitude. Thus, this was found to be a preferred approach as it reduces computation time and model complexity.

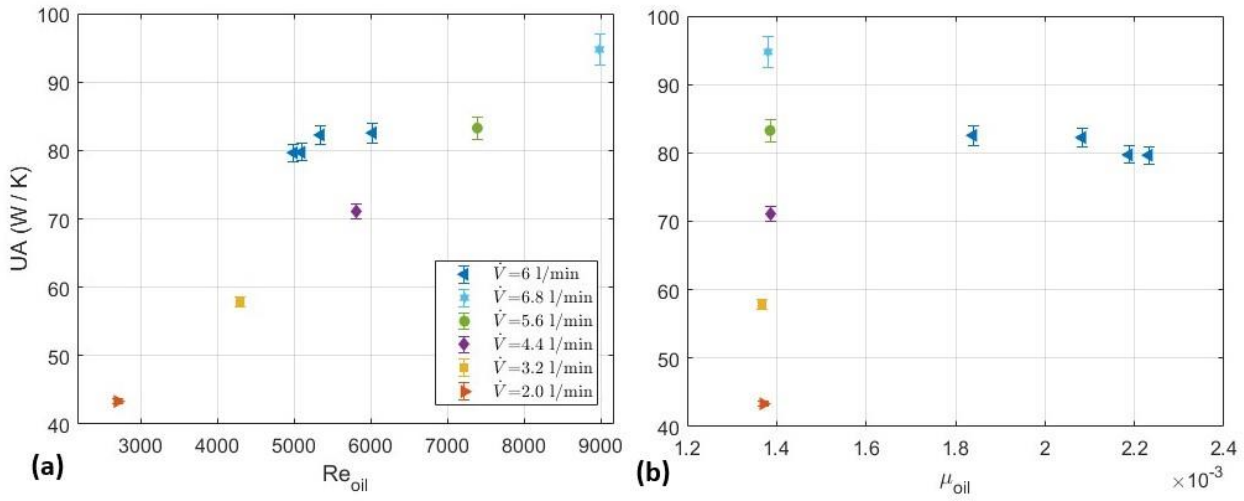

Figure 33: Variations in oil side heating through changes in flow rate and temperature, plotted as a function of Reynolds number (a) and dynamic viscosity (b).

Using the method described above, the oil-side heat transfer was determined for a variety of steady state points (averaging 15 minutes of data). This analysis was conducted by varying the oil flow rate at constant temperature and varying the temperature at constant flow rate. For the varied temperature evaluation, the mean oil temperature spanned from $123 \rightarrow 135°C$. Influence of viscosity on heat transfer is show in Figure 33 (b) where all points of constant temperature have similar viscosities and data with constant flow rates show different viscosity due to the variations in temperature. The effect of Reynolds number on heat transfer is shown in Figure 33 (a) where there is a near linear relationship for all points with constant temperature. However, when the flow rate is held constant, there is less of an effect. Considering the uncertainty in the calculation, it may be assumed that there is no change in heat transfer, as the margins of errors overlap for these points. For these cases, the change in Reynolds number is largely attributed to the change in viscosity and/or temperature. It must be noted that there was an effect on flow velocity due to density change; however, this was less significant due to the small variations in temperature. The conclusion drawn from these results is that oil side heating is largely dependent on Reynolds number. However, changes in Reynolds number due to variations in viscosity are less noticeable. This is attributed to the flow geometry where oil side baffles increase mixing for low viscosity flows. Therefore, as the Reynolds number decreases due to higher viscosities, the effects of flow enhancements are more pronounced, leading to a negligible reduction in heat transfer despite these lower Reynolds numbers.

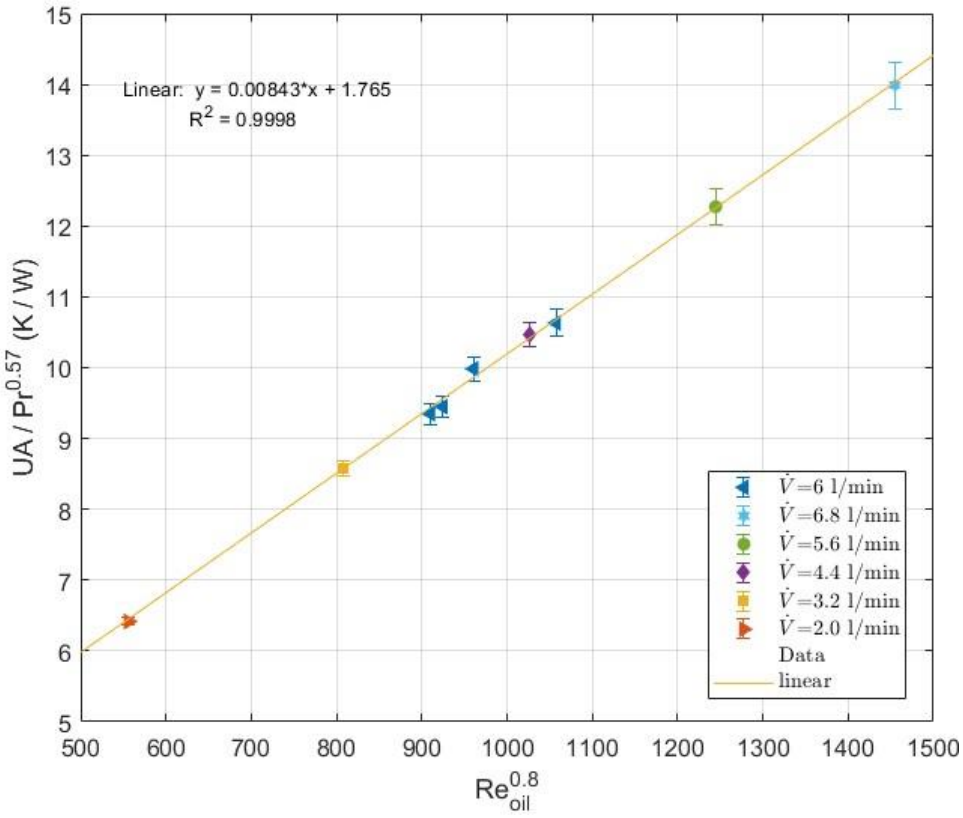

Figure 34: Curve fit used for oil cooler model development.

Based on the discussion above, changes in Reynolds number due to variations in fluid temperature have less of an effect on oil side heating. Therefore, if these factors can be neglected an accurate estimate of the heat transfer can be determined. This would counteract Reynolds' dependence on viscosity allowing for accurate heating estimates as flow rates and temperatures are varied. Shown by the semi major axis in Figure 34, this was performed using the Prandtl number, Eqn. 34, a nondimensional parameter that is defined by the state of a given fluid.

$$\mathrm{Pr} = \frac{v}{\alpha} = \frac{\mu/\rho}{k/(\rho C_p)} \tag{34}$$

$$\mathrm{Re} = \frac{uL}{v} \tag{35}$$

It is the ratio of the momentum diffusivity, v to the thermal diffusivity α both of which are specific to the given fluid. Therefore, with the Reynolds number (Eqn. 35) also in terms of momentum diffusivity, dependence on this parameter can be isolated.

Through a parametric evaluation it was found that a Prandtl number to the power of 0.57 enabled all cases to fit the linear trend when flow rates were varied. It was also noted that a Reynolds number to the power of 0.8 enabled a more accurate linear approximation, Eqn. 36.

$$\mathrm{Nu} = \mathrm{Pr}^{0.57}(0.0139\mathrm{Re}^{0.8} + 2.901) \tag{36}$$

Using the linear trend from Figure 34 and the definition of the Nusselt number, the oil side heating was modeled in a usable form to be encoded. The resulting correlation is of similar form as the Dittus-Boetler equation (Eqn. 32) where heating shares a direct relationship with the Prandtl number and Reynolds number. Using this empirically developed correlation and Eqn. 32 representing coolant side resistance, the total heat transfer can be predicted.

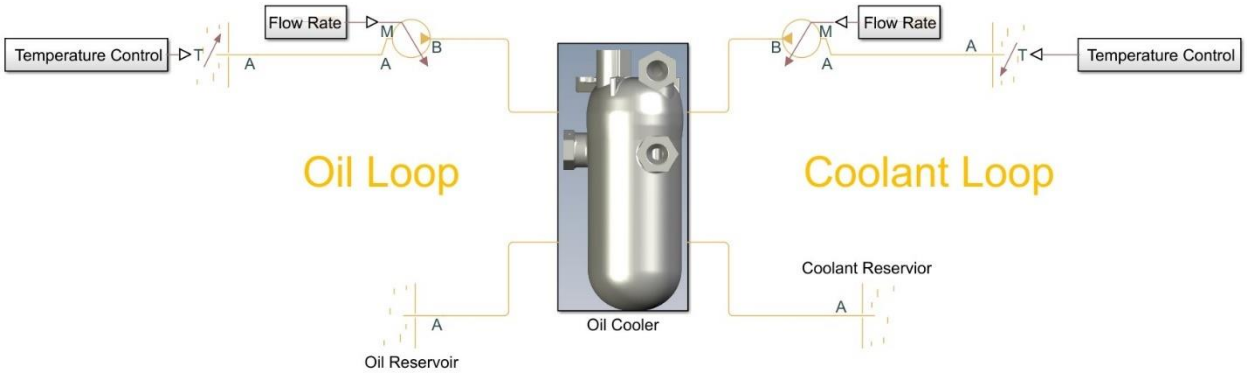

Figure 35: Simscape Oil Cooler Evaluation Model

Using a finite volume approach and the MATLAB Simulink software, the correlations discussed above were used to develop a custom heat exchanger model. As shown above, the model is isolated from other system components and the inlet temperatures and flow rates are controlled using empirical data. This enables an accurate assessment of model performance without the included errors produced by other modeled components.

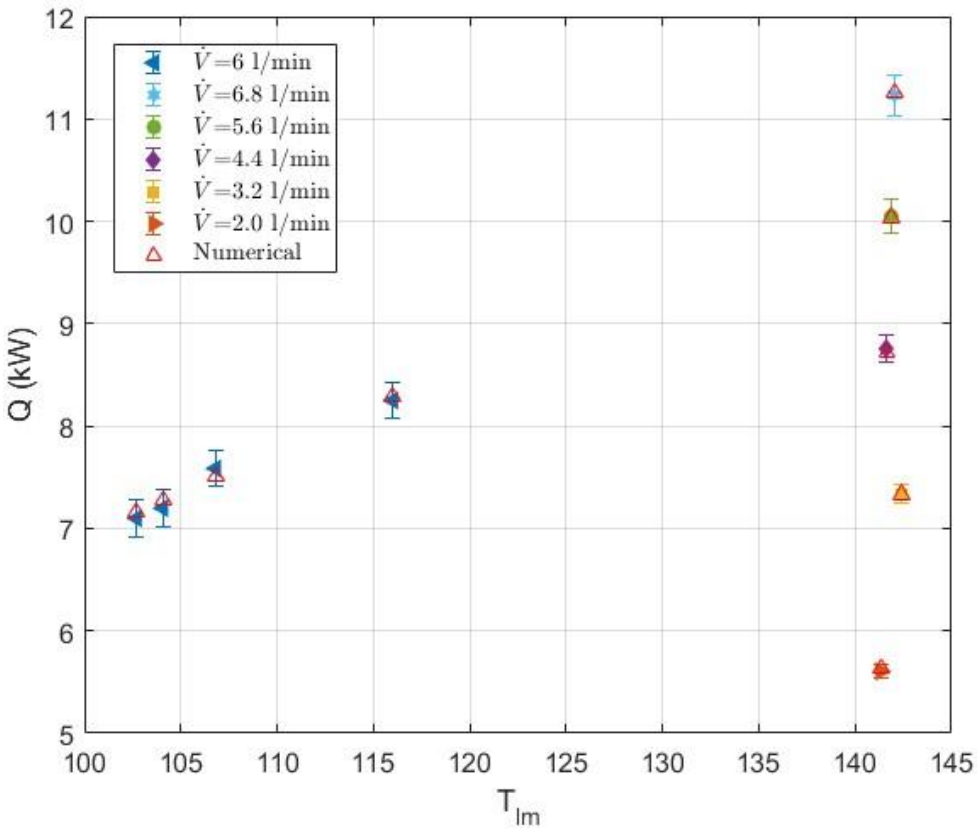

Figure 36: Performance assessment of the modeled oil cooler

The results of the model are shown in Figure 39 where all numerical values are within the uncertainties of the experimental system. This represents the models ability to predict heating through controlled variations in flow rate and temperature. At a constant flow rate, changes in heating are attributed to variations in log-mean-temperature, shown by the four left most points. At constant temperature, differences in heating are accredited to different flow rates, shown by the five right most points. Due to the large discrepancy in fluid heat capacity, changes in log-mean-temperature primarily represent changes in mean oil temperature. The performance of the model during these steady state conditions is assessed based on the RMSE and maximum error found to be 0.8% and 1.4%, respectively.

4.3 Evaporator Steady State Analysis

4.3.1 Tube-in-Tube

The Simulink fluids library has a MB heat exchanger model that utilizes the effectiveness-NTU method to determine the liquid, mixture, and vapor zone length fractions. The domains of this model are consistent with the experimental system, incorporating a single-phase liquid on one side, and a two-phase fluid on the other side of the heat exchanger. It also includes an array of heat exchanger categories, flow arrangements and has user inputs for geometry specifications. However, it does not account for flow enhancements, such as flow

turbulators, nor does it allow for consideration of thermal losses. Unfortunately, modifications cannot be made to the source code incorporating these effects because the component is proprietary. Therefore, the performance of the built-in components is assessed without these additional effects.

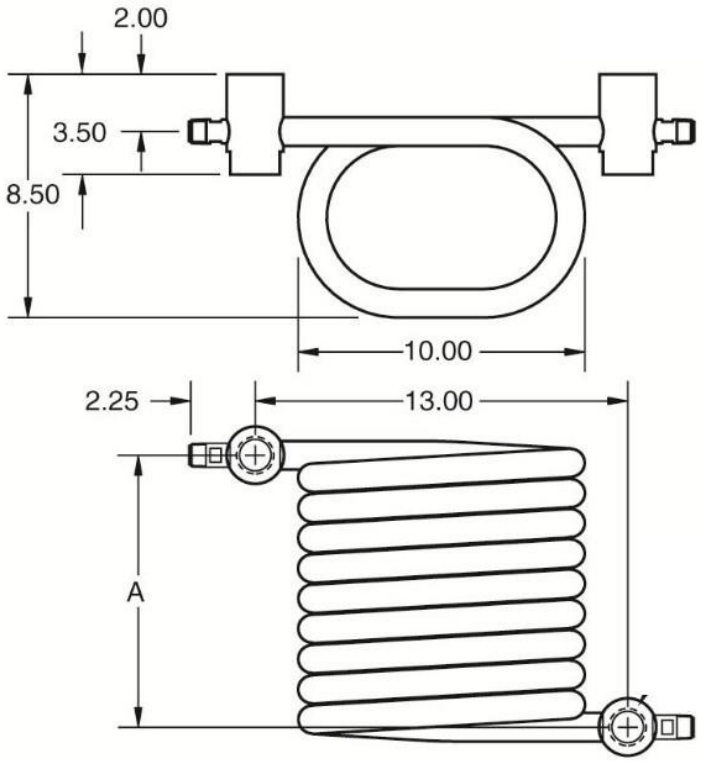

Figure 37: Geometry of a model AS-00528, tube-in-tube heat exchanger produced by Exergy LLC (Units in inches).

The physical evaporator is composed of four coiled, TTHX, placed in series, made from $316L$ stainless steel with a surface roughness of $0.5\mu m$. A single device is shown in Figure 37. In the device, hot oil is forced through the annular shell and water is pumped through the inner tube, under a counter flow arrangement. Fiberglass insulation is applied externally, three-inches-thick. For temperature measurements, E-Type probe thermocouples are used with a special limit of error of $\pm 1°C$ or 0.4%. For pressure measurements, SPTDT25 pressure transmitter are used with a range-based error of 0.5%. These sensors define the state of single-phase fluids at the inlets and outlets of the device.

The two-phase, thermal-liquid heat exchanger model in the Simulink fluids library offers a tube-in-tube geometrical configuration with counterflow arrangement, meeting most of the requirements of the physical evaporator. This model quantifies heat transfer using theoretical and empirical correlations referencing the Nusselt number. However, identifying the values of this parameter can be complex and depends on many aspects of the flow path and heat exchanger geometry and materials.

Using correlations for tube flow, the built-in heat exchanger model uses the following correlations defining the heat transfer coefficient under various flow reschemes, shown by Eqns. 37 through 39.

$$\mathrm{Nu}_{\mathrm{lam}} = constant \tag{37}$$

$$\mathrm{Nu}_{\mathrm{mix}} = 0.05\left[\left(1 - x + x\sqrt{\frac{\nu_{SV}}{\nu_{SL}}}\right) Re_{LO}\right]^{0.8} \mathrm{Pr}_{SL}{}^{0.33} \tag{38}$$

$$\mathrm{Nu}_{\mathrm{turb}} = \frac{f/8(Re - 1000)\mathrm{Pr}}{1 + 12.7\sqrt{f/8}\,(\mathrm{Pr}^{2/3} - 1)} \tag{39}$$

The laminar Nusselt number is treated as a constant. Under this flow rescheme the Nusselt number is often derived using a theoretical approach using the energy equation with the assumption of fully developed flow and constant surface heat flux. This produces a closed set of equations solving the velocity and thermal profiles (for a complete derivation see Incropera and DeWitt [11]).

For concentric annular pipe flow, assuming an insulated annulus and constant surface temperature, the laminar Nusselt numbers can be interpolated using

Table 1. For the given heat exchanger, the inner and outer Nusselt numbers equate to 5.61 and 4.49, respectively. These constants are then used as user inputs, enabling the model to represent the heat transfer coefficients in the laminar flow rescheme for annular straight pipe flow.

Table 1: Theoretically derived Nusselt numbers for fully developed flow through a concentric annulus with one wall insulated and the other held at constant temperature [11].

D_i/D_o	Nu_i	Nu_o
0	—	3.66
0.05	17.46	4.06
0.10	11.56	4.11
0.25	7.37	4.23
0.50	5.74	4.43
≈1.00	4.86	4.86

For the turbulent two-phase rescheme, the Nusselt number is calculated using the semiempirical Cavallini and Zecchin correlation, Eqn. 38. Developed in 1974, this relation describes the heat transfer processes of forced convection condensation and is applicable to a range of Reynolds numbers from $7{,}000 \rightarrow 53{,}000$. However, for stability a cubic function is incorporated, blending the heating rate at both boundaries of the two-phase rescheme, specifically between a quality of $0.0 \rightarrow 0.1$ and $0.9 \rightarrow 1.0$.

For single phase turbulent flow, the Nusselt number is calculated using the Gnielinski correlation. This correlation is often applicable near the transitional rescheme, having range of Reynolds numbers from $3000 \rightarrow 5 \times 10^5$ [11]. However, this correlation is only suitable for smooth pipes. According to Dejan [13], the smooth pipe assumption is only valid for flow with $2300 < Re_D < 5 \times 10^5$ if the relative roughness is $\epsilon/d < 5 \times 10^{-4}$. Fortunately, the evaporator meets these requirements, with a surface roughness at about a magnitude less. Thus, this assumption is found to be applicable for the surface of the TTHX; however, as shown below the model significantly underpredicts heating rates.

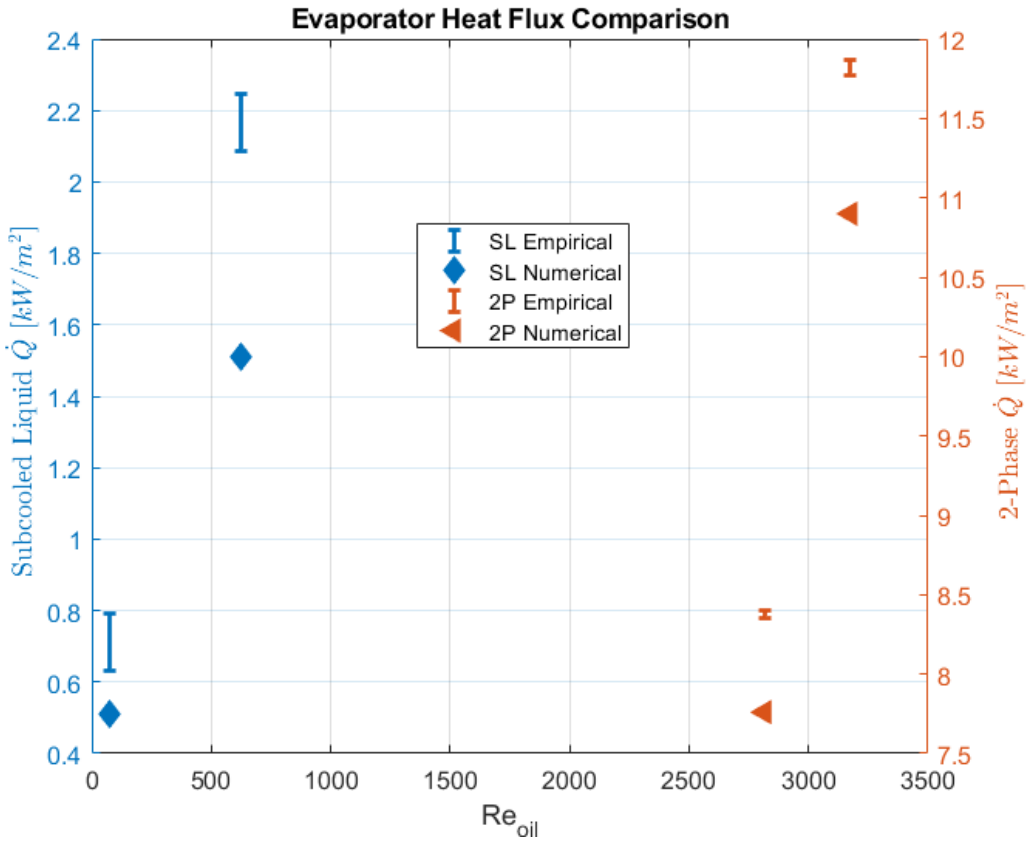

Figure 38: Numerical heat flux comparison using the Simulink MB heat exchanger model overlayed with empirical results.

To validate the built-in Simscape heat exchanger model, multiple steady state trials were conducted by varying the water flow rate and inlet oil temperature. As shown in Figure 38, these trials incorporated two different fluid configurations i.e., liquid-to-liquid and liquid-to-multiphase. For each case the model is shown to underpredict heating rates with an RMS error of 38.4%, 41.3%, 12.52% and 8.05%, going from high to low heating rates. Despite the more accurate multiphase heating predictions, the model incorrectly predicts the fluid phase at the outlet, predicting two-phase when the empirical data suggests superheated vapor. Interestingly, for all cases the model assumes a completely insulated design, unlike the physical evaporator that experiences losses from about $0.5 \rightarrow 1.5$ kw. For the model this should result in larger temperature gradients producing higher heating rates (assuming the heat coefficients

are modeled correctly). Therefore, this modeling strategy is found to be insufficient. The model uses straight pipe correlations which are not consistent with the experiment and will be investigated as a possible source of error.

As shown in Figure 37, the physical heat exchanger is not a straight pipe, it's curved through about 75% of the flow path. As discussed by Zhao [14], helical or curved tubes generate a secondary flow, that increases mixing and enhance heat transfer, giving reason for why the MB model is underpredict heating rates. Therefore, because the geometry is semi-coiled or closely resembles a helical heat exchanger, these heat exchanger concepts were investigated.

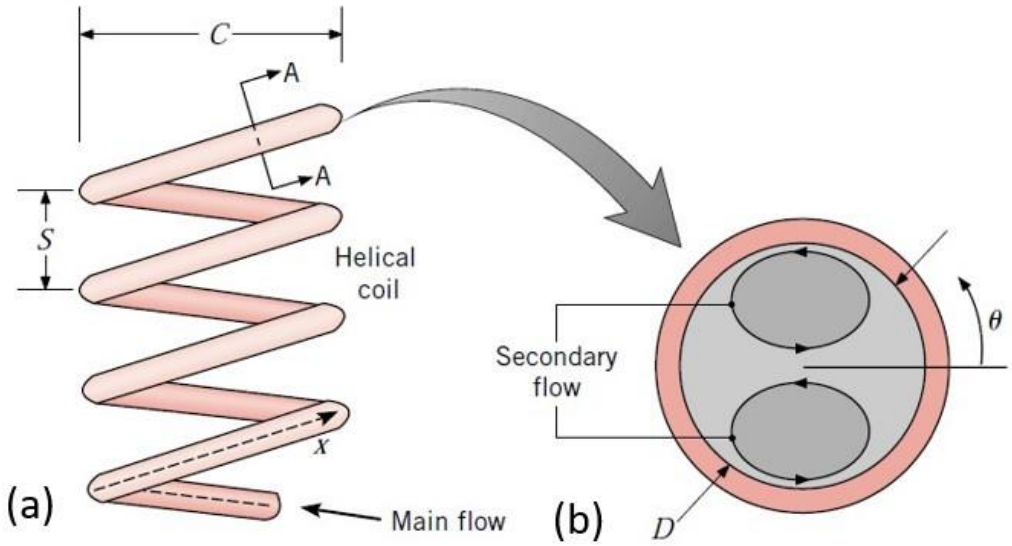

Figure 39: Diagram of helical coiled tube (a) and cross-section showing induced secondary flow (b) [11].

Coiled heat exchangers have been investigated for more than two centuries, having a variety of applications including chemical reactors, refrigeration, air conditioning, food, and dairy processing, to name a few. This is largely due to their enhanced heat transfer, ease of manufacturing, and compact size [43]. A schematic of the helical geometry is shown in Figure 39 (a). Figure 39 (b) shows the flow patterns are more complicated than straight tubes due to the centripetal forces that impart additional pressure gradients causing a secondary flow to form. These flow patterns complicate the analysis and helical models often rely on empirical correlations to quantify heating rates. This secondary flow can be described as two vortices, often referenced as Dean vortices, where the flow travels along the outer wall, perpendicular to the main flow eventually joining at the centerline, Figure 39 (b). Interestingly, these vortices generate stabilization effects that delay turbulent transition. Much research has been devoted to quantifying this onset, using the dimensionless curvature ratio as the sole parameter, Eqn. 40.

$$\delta = D/C \tag{40}$$

In most recent research, like El-Genk and Schriener [15] which purpose the rational argument that as $\delta \to 0$ turbulent transition approaches that of straight pipe flow, Eqn. 41.

$$Re_{cri} = 2300[1 + 51640\delta^{1.575}]^{0.2} \tag{41}$$

Additionally, there are other geometric effects to consider as well, such as helical pitch. Unlike the curvature ratio, helical pitch decreases centripetal effects and increases turbulent transition. However, for heating considerations, pitch effects have been shown to be negligible for a $P/D < 60$ [14]. At more than a magnitude less, this geometrical aspect was ignored, allowing the flow path to be modeled as a torus.

$$\mathrm{Nu_{lam}} = (2.153 + 0.318\mathrm{De}^{0.643})\mathrm{Pr}^{0.177} \qquad \begin{matrix} 20 < \mathrm{De} < 2000 \\ 0.7 < \mathrm{Pr} < 175 \\ 0.027 < \delta < 0.087 \end{matrix} \tag{42}$$

$$\mathrm{Nu_{turb}} = 0.013\mathrm{Re}^{0.93}\delta^{0.177}\mathrm{Pr}^{0.40} \qquad \begin{matrix} 0.7 < \mathrm{Pr} < 2000 \\ 9.7 \times 10^3 < \mathrm{Re} < 1.4 \times 10^5 \\ 0.012 < \delta < 0.177 \end{matrix} \tag{43}$$

In a comparative study, Zhao et. al. formulates an extensive set of correlations based on flow through helical tubes. These cover various physical aspects of the flow, such as turbulence transition, friction factors, and laminar and turbulent heating. Defined using the Nusselt number, these heating correlations are given a range based on the experimental envelope that was used to define them. In the laminar rescheme, many heating correlations are defined in terms of the Dean number, Eqn. 44.

$$\mathrm{De} = Re\delta^{1/2} \tag{44}$$

The Dean number accounts for centripetal forces by applying the curvature ratio, δ to the Reynolds number. This recognition pays tribute to W.R. Dean, the first person to obtain a theoretical solution for laminar flow through curved pipes. As shown by Eqn. 42, the Dean number is used by the correlation developed by Xin and Ebadian (1997). Performance of this correlation was evaluated for the subcooled flow due to its simplicity, and applicable range of parameters. However, once the water becomes superheated the turbulent correlation from Zhao et. al. (2020) is used, also within range of the experimental parameters (i.e., Pr, Re, and δ), shown by Eqn. 43. These correlations were than compared with those of a straight pipe, Figure 40.

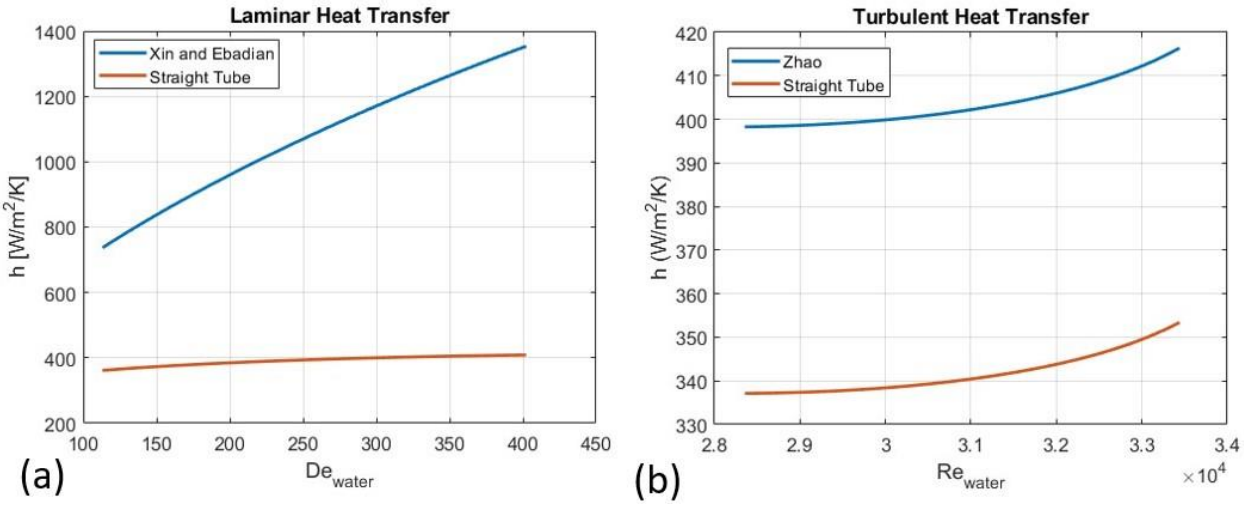

Figure 40: Heating comparison for the subcooled laminar flow (a) and turbulent superheated vapor (b).

As shown in Figure 40, the heating rates for coiled pipes supersede that of straight pipe for both the laminar (a) and turbulent reschemes (b); however, there is greater effect for the laminar flow cases. This is largely due to the enhanced mixing caused by the induced Dean vortices [43]. This increases the temperature gradient near the wall, thereby increasing heat transfer. Nevertheless, for turbulent flow the temperature gradient is already large due to the dynamic boundary layer; thus, the additional mixing has less of an effect, shown in Figure 40 (b).

Unfortunately, acquiring heating relations for two-phase flow is not as simple as the single-phase case. There are a wide variety of correlations for two-phase flow in pipes; however, there are no helical boiling correlations that span the working conditions of the experimental system.

$$\mathrm{Nu}_{\mathrm{turb,coil}} = \mathrm{Nu}_{\mathrm{turb,straight}}(1 + 3.5\delta) \tag{45}$$

Therefore, due to the turbulent nature of the two-phase flow, Eqn. 45 will be used to correlate turbulent boiling in curved pipes. This is a simplistic analogy by Jeschke [16] that correlates turbulent heating rates of coiled pipes to that of straight pipe flow. Comparing this with the turbulent coiled correlation from above (Eqn. 43) results in an error of about 3%, suggesting this approximation accurately relates these flow geometries at the given flow rates and temperatures.

$$h_{TP} = 3.90 h_{lo} \left(\frac{1}{X_{tt}}\right)^{0.62}$$

$$h_{lo} = 0.023 \mathrm{Re}_{LO}^{0.8} \mathrm{Pr}_{SL}^{0.4} k_{SL}/D$$

$$X_{tt} = \left(\frac{1-X}{X}\right)^{0.9} \left(\frac{\rho_{SV}}{\rho_{SL}}\right)^{0.5} \left(\frac{\mu_{SL}}{\mu_{SV}}\right)^{0.1} \tag{46}$$

A relatively simple correlation for boiling flow in a straight pipe is that developed by Mathur (1976), shown by Eqn. 46 [14], - the subscripts SL and SV represent the associated properties at the saturated liquid and saturated vapor state. This correlation was developed using $R22$ refrigerant and a tube diameter of $9\ \mathrm{mm}$. Compared to other boiling relations such as Shah (1982) and Gorgun (1986), this correlation is easier to implement and requires less equations and fewer known variables [14]. Additionally, the geometry used for its development nearly matches that of the inner tube of the evaporator. Using typical operational conditions of the experimental system this relation is shown in Figure 41.

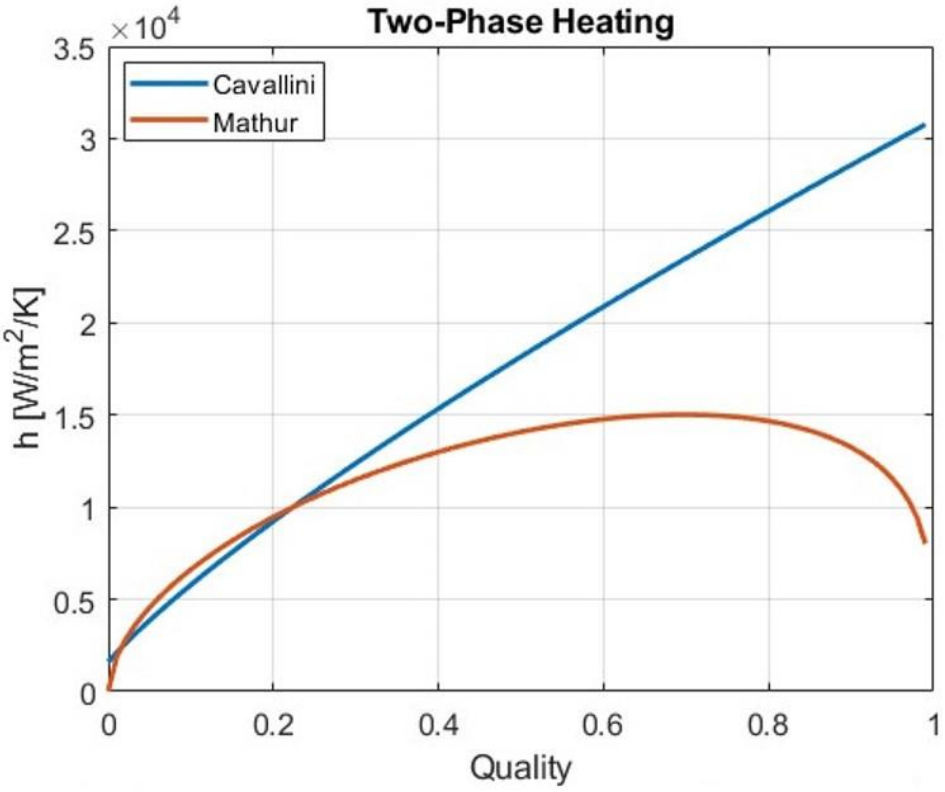

Figure 41: Heating comparison between Cavallini and Zecchin (1974) and Mathur (1976) correlations with $G = 49.1\ \mathrm{kg/m^2\ s}$ and $P_{sat} = 1\ \mathrm{atm}$.

As discussed previously, the Simscape MB model uses a condensation correlation to represent two-phase heating. However, in the physical evaporator boiling is occurring. Therefore, it was advantageous to compare the two correlations to discern if heating is correctly represented by the imposed correlation. The boiling correlation of Mathur and the condensing correlation of Cavallini, Figure 41, both show relatively high heating rates compared

to the subcooled liquid and superheated reschemes from Figure 40. Interestingly, these two-phase correlations are at the same magnitude and increase directly with quality until $X \cong 0.7$ where the boiling correlation begins to decrease. The overall trends, however, are very different where the condensing correlation appears nearly linear and the boiling correlation slope is initially high but continues to decrease with quality, eventually becoming negative at $X \cong 0.7$. Additionally, despite the variation in these results implementing one correlation over the other will not have a significant impact on the heating rate if the overall heat transfer is primarily dependent on the thermal resistance of the oil.

$$A_o U_{overall} = \left(\frac{1}{A_o U_o} + \frac{\ln(r_o/r_i)}{2\pi k_w L} + \frac{1}{A_i U_i}\right)^{-1} \tag{47}$$

This is observed in Eq. 47 where the third term on the right (representing the thermal resistance of the water) approaches zero as $U_i \to \infty$, simulating a large heat transfer coefficient for the water side of the evaporator. Therefore, it was advantageous to compare the heat transfer coefficients between the two fluids in the evaporator to determine the relative importance of the implemented 2-phase correlation. Thus, quantifying the oil heat transfer not only allows for the calculation of the overall heating but can also allow for a relaxation of the equation scrutiny in the two-phase rescheme.

$$\mathrm{Nu} = 0.075\mathrm{De} + 5.36 \tag{48}$$

There are few correlations for annular flow in helical heat exchangers. Some available publications, such as those by Reenie and Hagavana (2005) suggest a linear dependence with the Dean number [17], shown by Eqn. 48 . However, through empirical evaluations these relations did not replicate system performance, underpredict at low heating values, and over predict at higher heating rates. Additionally, implementing circular pipe flow relations such as Eq. 48, using the correlated hydraulic diameter, is often only suitable for turbulent flows [18]. Thus, with the oil assumed entirely laminar, continuing with the correlation-based approach was not suitable. Instead, the oil heat transfer was characterized empirically by varying the inlet temperature of the oil and flow rate, effectively controlling the mean Reynolds number. Interestingly, this evaluation was performed using the physical oil cooler as it is composed of two model AS-00528 heat exchangers, the same devises used for the evaporator. This approach took advantage of the capabilities of the coolant loop where a centrifugal pump, driven by a 0.5 HP motor, produced predictable single-phase turbulent flow through the inner tube of the heat exchanger. This resulted in a heat transfer coefficient much greater than that of the oil with liquid water as coolant. Therefore, any uncertainty in the oil resistance is reduced as the overall resistance is nearly unaffected by the low resistance of the coolant.

$$Nu = CRe^m Pr^n \tag{49}$$

To formulate an effective correlation based on empirical results one procedure commonly employed assumes convective heating can be described using Eqn. 49. Where the

power of the Prandtl number varies from about $n = 0.3 \rightarrow 0.4$, often found empirically [19]. However, a simpler approach, is to assume $n = 0.3$ if the fluid is cooled and $n = 0.4$ if it's heated, following results of the Dittus and Boelter equation. This variable grouping, Pr^n can then be divided through leaving the right side only in terms of the Reynolds number. This allows the Reynolds power, m to be determined through iteration until the line of best fit is obtained. The resulting slope is the constant C in Eqn. 49. These are the steps employed to determine the oil side heating correlation.

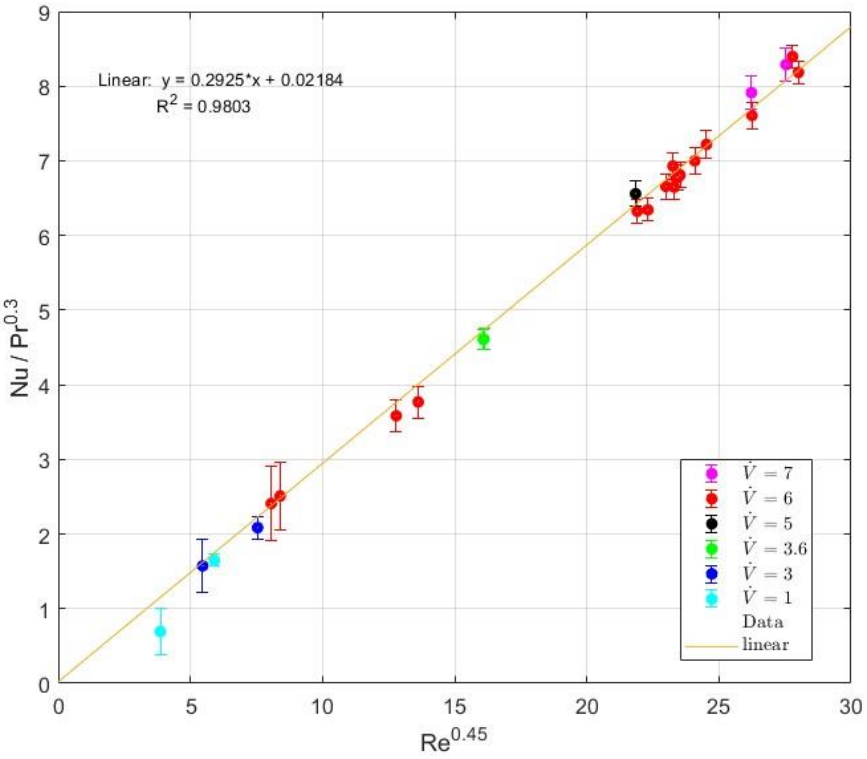

Figure 42: Heating within the tube-in-tube oil cooler with varied mean oil temperature and flow rate from $32 \rightarrow 150°C$ and $1 \rightarrow 7\ \mathrm{l/min}$, respectively.

$$\mathrm{Nu} = 0.2925\mathrm{Re}^{0.45}\mathrm{Pr}^{0.3} \tag{50}$$

Figure 42 shows several steady state values which were used to determine heating for the annular side of the oil cooler. These were averaged over 10 minutes with a collection rate of $1\ \mathrm{Hz}$. To represent the Nusselt number as a function of Reynolds number, the dependency on the Prandtl number was removed, shown by the semi-major axis. Using the process defined above, the best linear fit was found with $m = 0.45$ enabling the determination of the constant C in Eqn. 49. The resulting correlation is shown by Eqn. 61 which neglects the y-intercept found from the best fit line as this was insignificant.

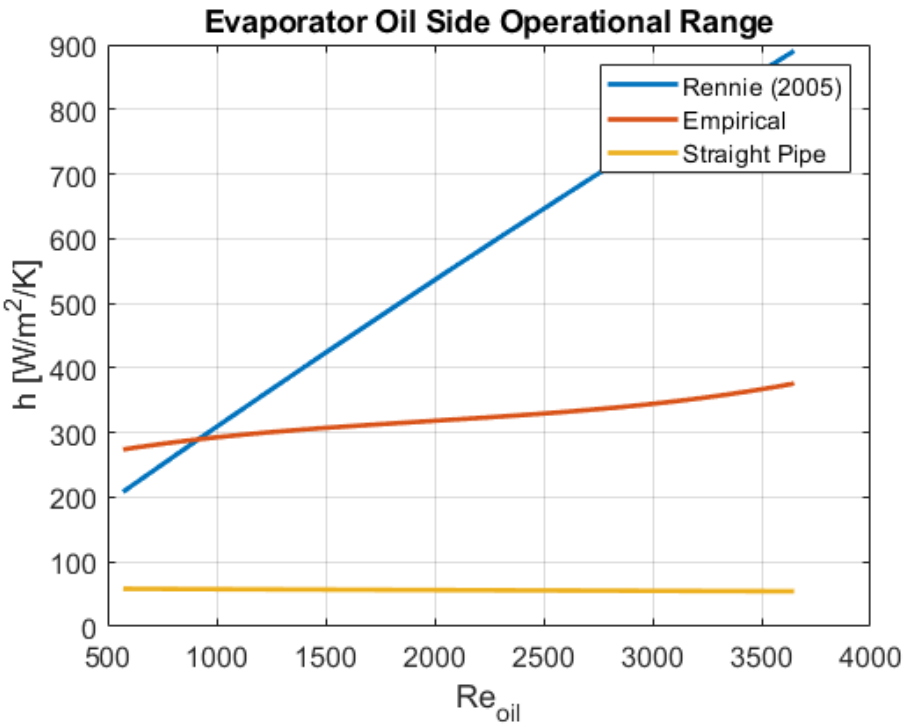

Figure 43: Heating comparisons for the evaporator annulus using typical system operations with $T_{oil} = 80 \rightarrow 200$ °C and $G_{oil} = 323$ kg/m^2/s.

With the coolant flow within the working ranges of the experiments performed by Zhao et. al. Eqn. 43 was used to determine the film coefficient of the coolant. This approximation assumes the flow path is entirely helical which is of course incorrect given the heat exchanger has sections of straight pipe. However, as discussed above, due to the relatively low resistance of the coolant any errors incurred by this approach are minimal. Thus, with all resistances known except the resistance of the oil, the oil film coefficient could be determined for the given investigation using the results from Eqn. 50. The results are given in Figure 43 with correlations for a straight pipe (derived from Table 1) and annular helical pipe flow from Reenie (2005), overlayed for comparison. Figure 43 shows that nearly the entire empirical trend is between the two correlations, which is a reasonable result as the heat exchanger is a combination of the two different geometries.

With heat transfer well documented for helical heat exchangers, and due to the likeness of geometry, the flow path of the waterside was evaluated assuming an entirely helical evaporator. Thus, heating for the subcooled liquid, liquid-vapor mixture, and superheated vapor was calculated using helical pipe correlations. As discussed above, large differences in heating existing between straight pipe and helical pipe correlations for laminar flow. However, the liquid region only encompasses about 18% of the enthalpy change; thus, if heating falls somewhere in between, inaccuracies due to this approximation should be minimal. For the two-phase rescheme, available correlations suggest large film coefficients relative to the oil, regardless of flow geometry. Thus, heat transfer is primarily a function of oil resistance and

variations between two-phase heating correlations are trivial. In the vapor rescheme, flow is turbulent and heating between two geometries varies by about 20%. However, like the subcooled domain this encompasses a small portion of the enthalpy change, at 5%. Therefore, this should also result in minimal error. These ideas suggest that for each region assuming a completely helical geometry will have a small effect on heating predictions. Ultimately, heating has a weak dependence on water flow regions because either the enthalpy change is small, or the convection coefficient is high, relative to the oil. Furthermore, with oil-side heating determined empirically, all convective resistances have given values and the evaluation of these approximations can be scrutinized. This is performed using a finite control volume model where input parameters (flow rates and temperatures) were controlled using experimental data.

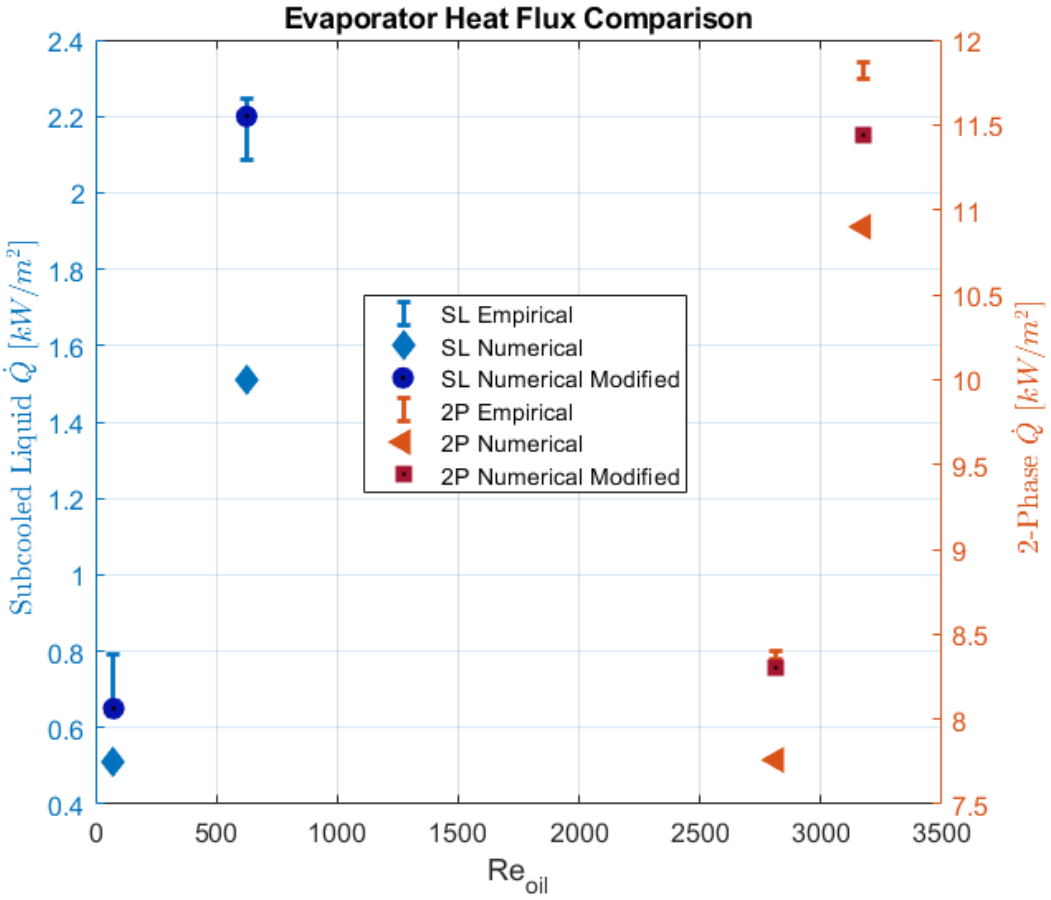

Figure 44: Performance assessment of the tube-in-tube evaporator model

Shown in Figure 44 the modified numerical results are within the uncertainty of the empirical data for most points tested. These points were averaged over ten minutes at 1 Hz. For all cases, model performance is better than utilizing straight pipe correlations. These results suggest, assuming helical geometry for water side is adequate in predicting steady state heating for the given evaporator. The performance of the model during steady state conditions is assessed based on RMSE and maximum error, at 14.2% and 36.4%, respectively.

4.3.2 Corrugated-Plate Analysis

The experimental system provides a scaled representation of the Rankine cycle system. However, it also serves as a test bench to test various components and assess the potential changes in system performance. The evaporator is a critical component that drives power generation and cooling capabilities of the system. Therefore, it is advantageous to represent the evaporator with the most applicable heat exchanger.

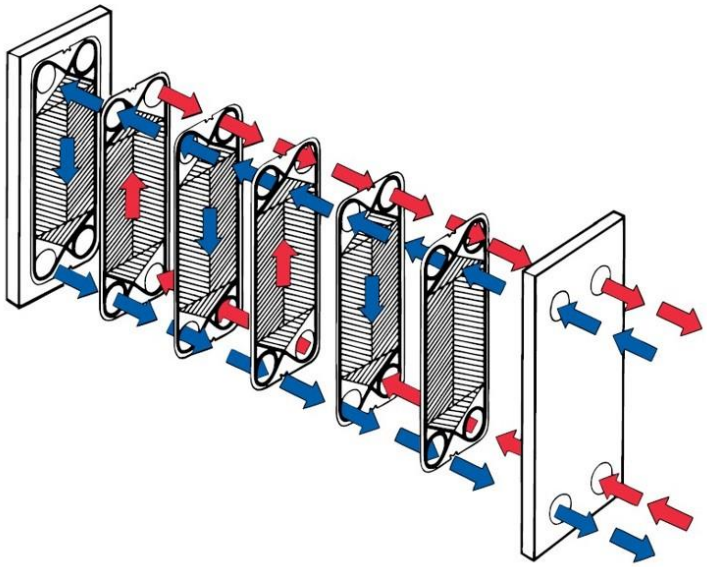

Figure 45: Corrugated plate heat transfer concept [45].

Considering various design metrics including operating conditions, performance, weight etc. it was determined that the corrugated plate heat exchanger (CPHX) is well suited for aircraft applications. An expanded diagram is shown in Figure 45 where the red and blue arrows indicate a counter flow arrangement. This design increases performance by maximizing surface area while minimizing volume space. From the figure inlet flow is forced through multiple narrow channels across corrugated plates. These plates function as flow turbulators increasing heat transfer by interacting with the boundary layer and enhancing flow mixing.

Based on system operating conditions a Xylem Brand brazed plate heat exchanger was integrated into the system. This heat exchanger has sixteen plates resulting in a near equivalent heat transfer area as the TTHX analyzed previously. However, the size and weight of the CPHX is less, with dimensions of $21 \times 1.6 \times 4.4\ \text{in}^3$ and weight of $5.7\ \text{kg}$ compared to the TTHX that has dimensions and weight at $80 \times 11 \times 7.5\ \text{in}^3$ and $42.8\ \text{kg}$, respectively which provides a significant reduction in both parameters.

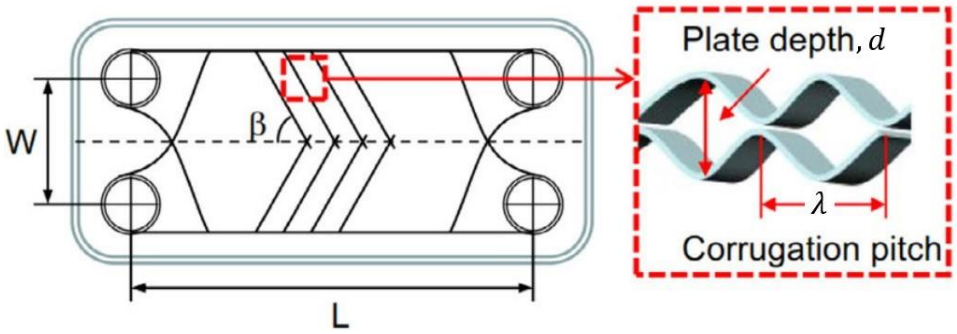

Figure 46: Geometry of a plate heat exchanger with a scaled cross section [29].

The inner geometry of the chevron plate HX is complex, with different variables used to define corrugation dimensions. This geometry affects heat transfer and pressure drop within the heat exchanger, specifically, the corrugation angle, β, corregation plate depth, d and corrugation pitch λ, shown in Figure 46. From literature, these dimensions vary widely resulting in contrasting correlations for various CPHX. Therefore, it is desirable to utilize a correlation that was developed with similar geometry. However, due to proprietary restrictions the geometry of the evaporator is unknown; thus, this approach is not feasible. Instead, experimentation is used to develop custom correlations specific to the given heat exchanger.

$$h_h = \frac{\dot{Q}}{A(T_h - T_w)} \tag{51}$$

As discussed in section 4.2 Oil Cooler Modeling), heat transfer is largely dependent on convective thermal resistance or the heat transfer coefficient of each fluid. Eqn. 51 represents one of the simplest forms quantifying this parameter. This uses the wall and bulk flow temperatures to perform the calculation. However, it's difficult to use in practice as measuring the inner wall temperature, T_w is challenging.

An alternative approach, referred to as the Wilson plot method, only requires known values for mean fluid temperature and heat transfer rates [18]. E. E. Wilson originally proposed this method to determine film coefficients for a shell and tube condenser where cool liquid flowing through the inner tubes condensed the shell-side vapor. This method is based on the concept of separating the overall thermal resistance into the convective resistance of one fluid and combining the remaining resistances of the heat transfer process.

$$R_{ov} = \frac{1}{h_h A} + \frac{t}{kA} + \frac{1}{h_c A} \tag{52}$$

$$R_{ov} = \frac{1}{h_h A} + b \tag{53}$$

$$b = \frac{t}{kA} + \frac{1}{h_c A} \tag{54}$$

This is shown by Eqn. 53 where all but the convective resistance of the cold liquid is combined into a single constant, b. If all resistances within a heat exchanger are held constant except the convective resistance of a single fluid, changes in the overall resistance are clearly due to the varied convective resistance. Therefore, shown by Eqn. 54 the convective resistance of a fluid must be held constant, referenced with the variable b. Performing this experimentally requires the fluid properties to remain constant, specifically fluid temperature and Reynolds number. However, if properties (conductivity, and viscosity) can be assumed linear function of temperature only the mean temperature must remain constant [20].

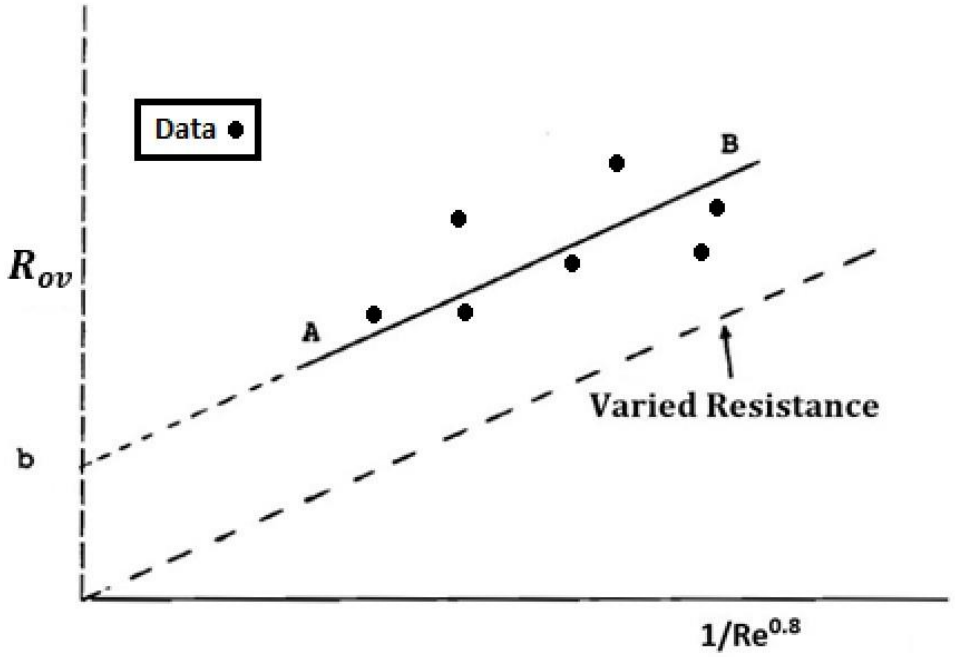

Figure 47: Traditional Wilson plot, adapted from [20]

This concept is shown above where overall resistance is determined for a variety of data points while the Reynolds number of a single fluid is varied. A curve fit has been applied forming a straight line from A to B. At the y-intercept the fluid resistance goes to zero as the Reynolds number approaches infinity. This is shown by the dotted line where only the varied resistance remains. At the y-intercept the overall resistance of the curve fit becomes equivalent to the remaining resistance noted by the variable b. However, the overall resistance is typically not linear with Reynolds number, as shown in Figure 47. Instead, the Reynolds number must be defined in a particular form.

$$\boldsymbol{R_{ov}} = m\frac{1}{Re_h^u} + b \tag{55}$$

Shown by Eqn. 55, a linear relationship can be formed when overall resistance is written as an inverse power to the Reynolds number. The value for the exponent u is intrinsic to the fluid flow path. A rigorous approach can be employed to obtain it by applying natural logarithms, followed by an iterative procedure discussed in [19]. However, a more simplistic

method was used where the exponent was varied until the curve fit best represented the trend, using the coefficient of determination (R^2 value). Wilson determined empirically that $n = 0.8$ results in a linear relationship for turbulent pipe flow, shown by the semi-minor axis in Figure 47.

A modification to the Wilson plot method discussed by Lee [21] assumes the heat transfer coefficients are in the form of a correlation similar to single-phase turbulent flow where

$$h_h = C_h Re_h^u Pr_h^v \left(\frac{k_h}{L}\right). \tag{56}$$

The value of the exponent v is often chosen to reflect that of the Dittus-Boelter equation with $v = 0.3$ for cooling and $v = 0.4$ for heating, following the process discussed in [22]. This expression can then be substituted into Eqn. 55.

$$R_{ov} = \frac{1}{C_h Pr_h^v (k_h/L) A} \frac{1}{Re_h^u} + b \tag{57}$$

Relating this to Eqn. 55, the slope m can be defined as

$$m = \frac{1}{C_h \mathrm{Pr}_h^v (k_h/L) A}. \tag{58}$$

However, this slope is also determined from the curve fit applied to the empirical data. Therefore, this slope, m, can be used to determine the constant, C_h by rearranging Eqn. 58.

$$C_h = \frac{1}{m \mathrm{Pr}_h^v (k_h/L) A} \tag{59}$$

All variables are known properties of the fluid and heat exchanger geometry; thus, C_h can be solved, providing the last value needed to define the film coefficient in Eqn. 56.

$$h_c = \frac{A}{b - \frac{t}{kA}} \tag{60}$$

Additionally, the slope intercept, b is also obtained from the linear fit; thus Eqn. 54 can be rearranged solving for the film coefficient for the cold fluid if the internal resistance of the wall (t/kA) is known.

This procedure can be repeated multiple times at different cold side resistances. With enough data, heating correlations can be developed for the cold side as well. However, a more accurate approach is to apply the Wilson method separately to both fluids [2018], that is, hold the resistance of one fluid constant while varying the other, and then vice versa. This approach simplifies the data collection procedure requiring the development of only two trends.

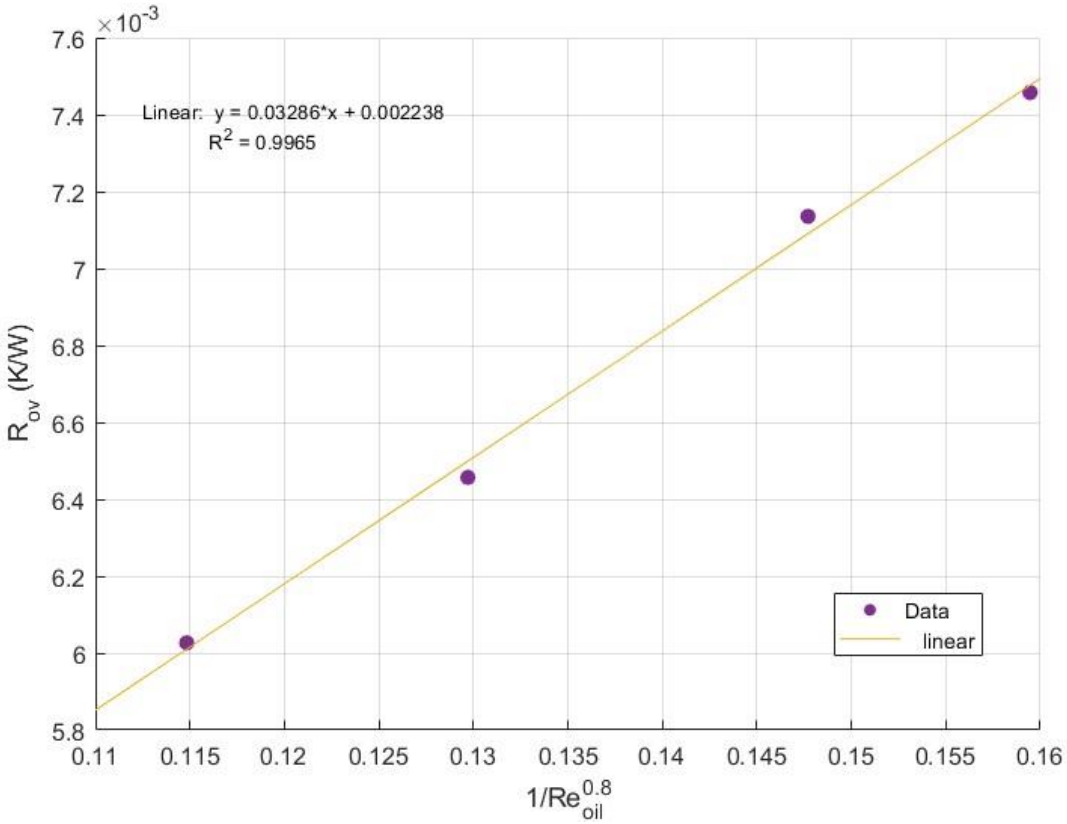

Figure 48: Wilson plot method applied to oil-side of the CPHX.

Due to the unknown geometry within the CPHX the Wilson plot method was used to determine the oil side film coefficient, Figure 48. This was performed using a single-phase investigation between the oil and liquid water. The oil flow rate was varied, and the water resistance was held constant. This study incorporated a range of oil side Reynolds numbers from $10 \rightarrow 15$ by varying the mass flux from $10.7 \rightarrow 17\ \mathrm{kg/m^2 s}$ and a range of Prandtl numbers from $5.20 \rightarrow 5.51$ by varying mean temperature from $79 \rightarrow 81\ ^{\circ}\mathrm{C}$. The slight variations in oil temperature ensured constant water side resistance. This is due to the direct relationship between heat transfer and fluid velocity. As the flow rate of the oil was increased, convection improved; thus, to prevent a change in outlet water temperature the log-mean-temperature was reduced. The limited range of Reynolds numbers was due to the high effectiveness of the heat exchanger that produced large changes in the fluid temperatures. Thus, to ensure fluid properties were within capabilities of the system the exit oil and water temperatures were limited. Specifically, this was to ensure the water was below the saturation limit and the viscosity of the oil was within the calibrated range of the flow meter.

$$Nu = 0.3761Re^{0.8}Pr^{v} \quad (61)$$

Using the definition of the Nusselt number (Eqn. 33) the film coefficient (Eqn. 60) can be nondimensionalized removing equational dependence on fluid properties. Therefore, Eqn. 61 can be applied to a variety of single-phase fluids. However, the applicability of this correlation is dependent on the dimensionless parameters utilized. As discussed above, this was between a narrow range of Reynolds and Prandtl numbers. During typical operation if the liquid water and superheated vapor are near these values further experimental testing may not be needed to predict heating in these domains. This correlation may then be applied.

During typical operation the mean Reynolds number for liquid water is 9.5, 5% less than the lower range of the correlation. When comparing Prandtl numbers, it is 46% less, at 2.8. However, for the superheated vapor there is more discrepancy. The mean Reynolds number is about 500 and the Prandtl number is near 1. Thus, for the case of superheated vapor this method is questionable. Testing the method would require additional experimentation. However, due to system limitations this was not feasible and instead the developed correlation was utilized for each single-phase fluid. Thus, for evaporator heating, this correlation was applied to the oil, subcooled water, and superheated vapor, leaving the two-phase region as the only unknown resistance.

The experimental system is not equipped with a preheater; thus, phase domains through the evaporator are comprised of three separate regions (i.e., subcooled liquid, two-phase, and superheated vapor). Therefore, to determine two-phase heating this region was isolated using predicted heating rates and lengths for the remaining regions. To simplify the analysis, the experimental procedure was conducted such that there was no superheated region; thus, only the subcooled liquid region needed to be removed.

$$\dot{Q}_h = \dot{m}_h C_{p,h}\left(T_{h,in} - T_{h,out}\right) \quad (62)$$

$$\dot{Q}_{c,SL} = \dot{m}_c Cp_c\left(T_{c,SL} - T_{c,in}\right) \quad (63)$$

$$\dot{Q}_{2p} = \dot{Q}_h - \dot{Q}_{c,SL} \quad (64)$$

With known inlet and exit oil temperatures, the total heat loss of the oil was determined using Eqn. 62. Strictly for the subcooled region oil heat loss and water heat gain is assumed equivalent. Thus, this energy can be quantified using Eqn. 63 and removed from the total oil heat loss. This determines the heat added only to the two-phase water, shown by Eqn. 64. With thermal losses less then $0.5\ kW$, thermal losses were assumed negligible, and a heat loss term was not included.

$$R_{ov,2p} = \frac{\Delta T}{\dot{Q}_{2p}} \quad (65)$$

As shown by Eqn. 65, this two-phase heating rate, $\dot{Q}_{2p}$, is used to determine the overall resistance of the region along with the temperature difference, ΔT, representing the temperature between saturated water temperature and mean oil temperature.

$$R_{2p} = R_{ov,2p} - R_{w,2p} - R_{h,2p} \tag{66}$$

$$R_{w,2p} = \frac{t}{kA_{2p}} \tag{67}$$

$$R_{h,2p} = \frac{1}{h_h A_{2p}} \tag{68}$$

Using the concept of resistances as discussed in section 4.2 Oil Cooler Modeling), the convective resistance of the water was isolated using Eqn. 66 where the resistance of the wall and oil is determined using Eqn. 67 and 68, respectively. However, not defined in these equations is the two-phase area, A_{2p}.

$$A_{2p} = A_{tot} - A_{SL} \tag{69}$$

This was determined using Eqn. 69. where the subcooled area, A_{SL}, is obtained utilizing an additional equation representing convective heat transfer, Eqn. 70.

$$\dot{Q}_{SL} = A_{SL} h_{ov,SL} \left(T_{h,SL,mean} - T_{c,SL,mean}\right) \tag{70}$$

This area term (A_{SL}) can be isolated and the subcooled heat transfer, is already defined by Eqn. 63. The only other unknown in Eqn. 70 is the overall resistance of the subcooled domain, $h_{ov,SL}$.

$$h_{ov,SL} = \frac{1}{\frac{1}{h_{c,SL}} + \frac{t}{k} + \frac{1}{h_{h,SL}}} \tag{71}$$

$$h = 0.3761 Re^{0.8} Pr^{v} \left(\frac{k}{d_h}\right) \tag{72}$$

This is determined using Eqn. 71 utilizing the film coefficient of the oil and liquid water using Eqn. 72. Thus, with all variables from Eqn. 66 defined, the resistance of the liquid-vapor region is known providing the last required variable to define the two-phase film coefficient, Eqn. 73.

$$h_{2p} = \frac{1}{A_{2p} R_{2p}} \tag{73}$$

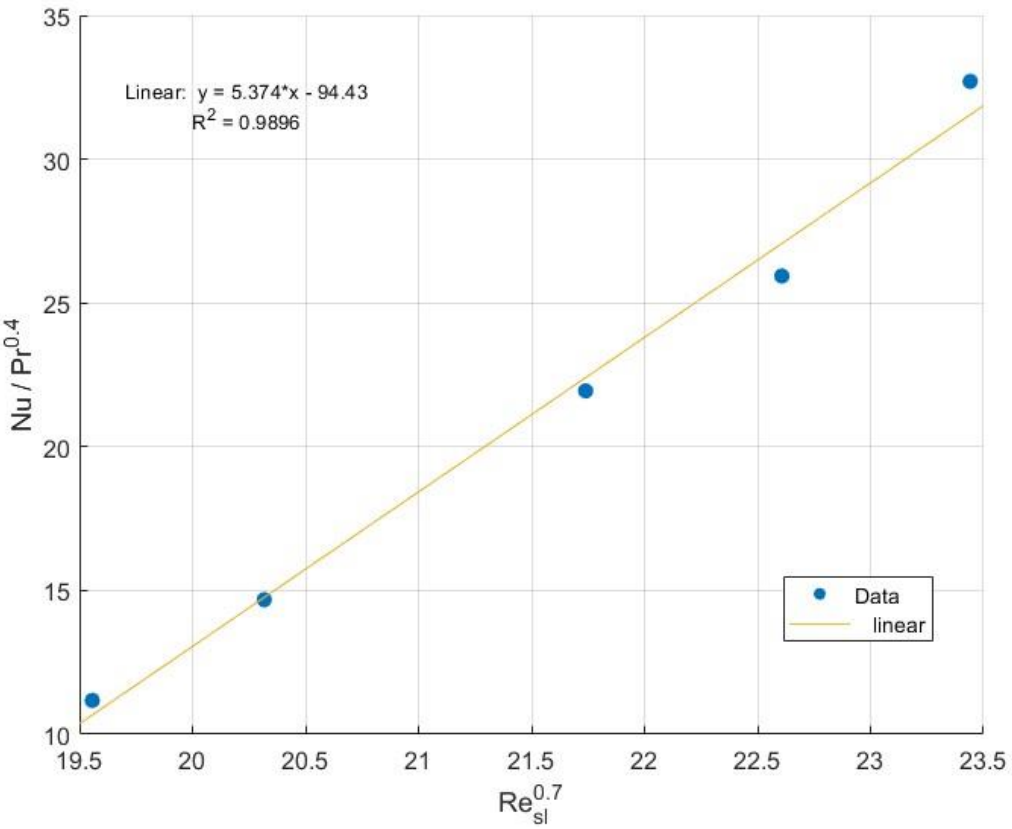

Figure 49: Two-phase heating within the CP HX

With the subcooled length removed, and two-phase water resistance separated from the overall resistance, heating within the two-phase domain could be determined experimentally, Figure 49. This involved varying the mass flux from $0.734 \rightarrow 0.881\ \mathrm{kg/m^2s}$ resulting in a Reynolds number from $18.5 \rightarrow 20.3$. However, the Prandtl number remained relatively constant at about 1.2 as the quality and temperature changes were minimal.

Following the process discussed above, the film coefficient was assumed to be in the form of Eqn. 56, (i.e., dependent on the fluid Reynolds and Prandtl numbers raised to specific powers). Therefore, the Prandtl number was raised to 0.4, indicating the fluid is being heated, and the Reynolds number was raised to 0.7 to produce the linear curve of best fit.

$$Nu = (5.374 Re_{sl}^{0.7} - 94.43) Pr^{0.4} \tag{74}$$

The resulting correlation is shown above where all nondimensional parameters reference saturated liquid water. Its applicability is based on the range of dimensionless parameters evaluated. The range of this correlation was limited to ensure high inlet steam quality with $x > 0.8$. This was quantified using an energy balance between the oil heat loss assuming negligible thermal losses.

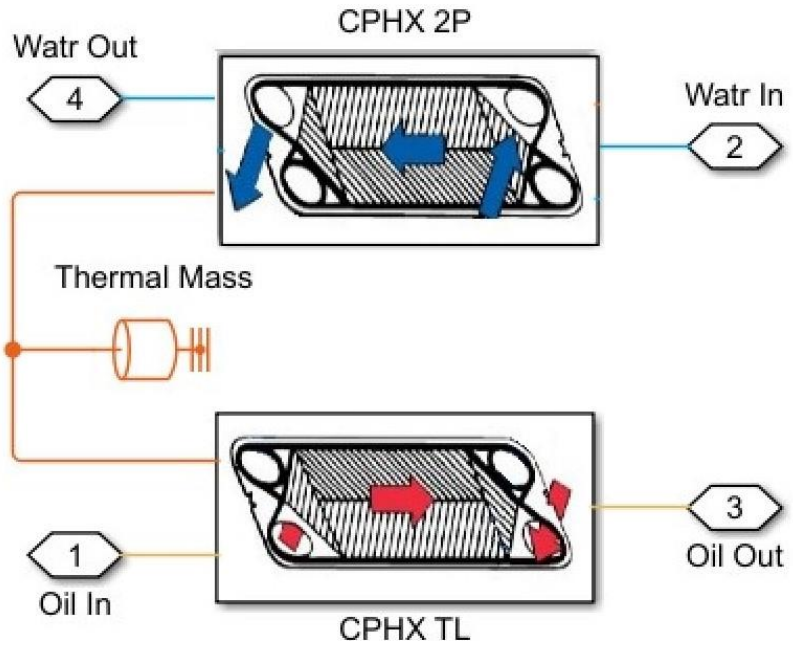

Figure 50: Simscape model showing a single cell of the finite volume CPHX model.

Using a similar process as the TTHX, convective heating correlations developed above were encoding using custom Simscape pipe blocks. This enabled the development of the corrugated plate evaporator model using the finite volume approach. As shown in Figure 50, this model incorporates the thermal mass of the heat exchanger; however, thermal losses and resistance of the inner plate were ignored due to their relative insignificance.

To simplify the model, the geometry of the cross section (perpendicular to the flow path) was modified. Rather than using eight channels, matching the physical evaporator, a single channel was used. This channel was equivalent in total cross-sectional area and depth between plates; however, its width was eight times that of the heat exchanger. Regardless of the geometry the model assumes heat is only transferred normal-to the inner plates; therefore, effects near the side wall are neglected. Thus, this simplification has no effect on performance as the model assumes a channel of infinite width regardless of which approach is used.

The validation of this model consisted of an isolation case where model input parameters (pressures, temperatures, and flow rates) were taken from empirical data; therefore, any errors incurred were only associated with the evaporator model.

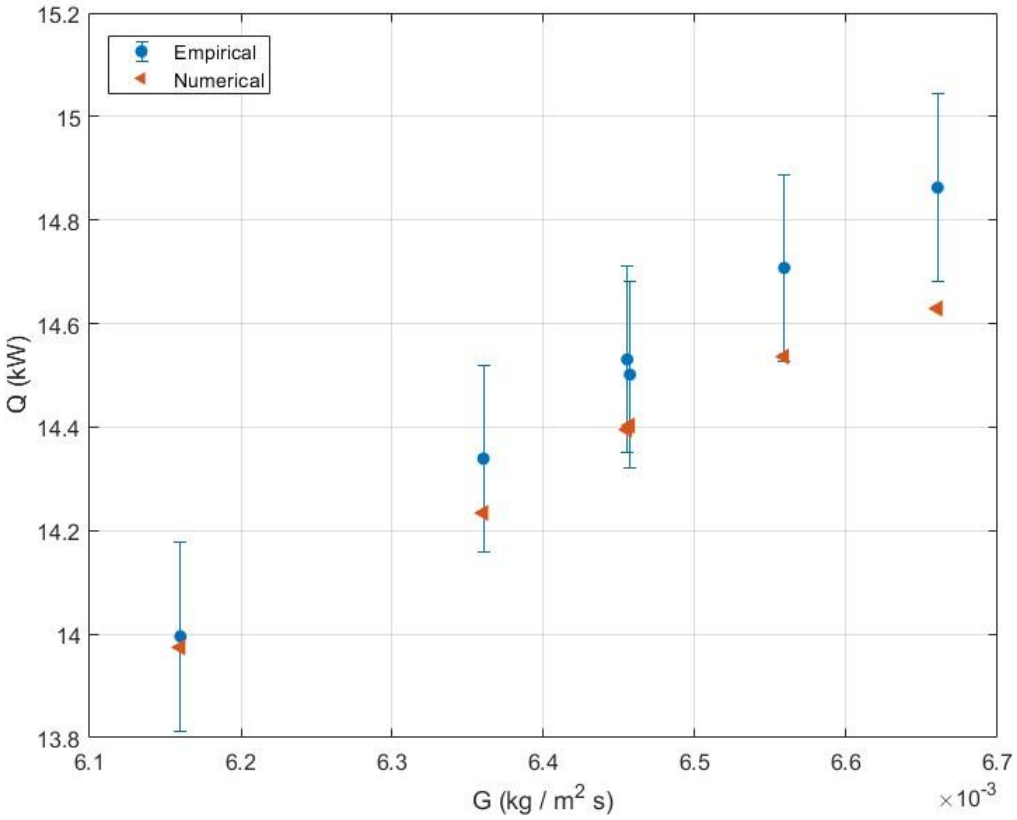

Figure 51: Performance of the corrugated plate evaporator model

The results of the CPHX model are shown above representing the heat absorbed by the steam as a function of mass flux. The range of this evaluation covered Reynolds numbers from $11.5 \rightarrow 12.7$ while the oil flow rate and inlet temperature were held constant, at $6\ l/min$ and $215\ °C$, respectively. From the figure, the numerical results replicate the trend where heating follows directly with mass flux. This follows logic that an increase in flow velocity increases convective heat transfer. Comparing results, most numerical values are within uncertainties of the system. Except at the highest flow rate where it underpredicts by about 1%. Based on the RMSE and maximum error, model performance is 1.01% and 1.62%, respectively. For all cases the model accurately quantifies steam quality, exiting the evaporator as superheated vapor.

4.4 Evaporator Transient Analysis

With steady state heating rates evaluated, the accuracy of the evaporator models was measured during transient events. These predictions are crucial as aircraft requirements become dynamic during changes in flight situations. When this occurs the fuel flow rate and system requirements may change. Therefore, the system response must also be dynamic, meeting new requirements in real time. With system capabilities largely dependent on steam production, transient performance of the evaporator must be accurately modeled. This ensures system parameters are controlled effectively, meeting system requirements continuously through this transition.

The thermal management system (TMS) controls system operations by regulating the fuel temperature, ensuring it remains within enthalpy bounds. The water flow rate is the main driver that regulates this temperature. At higher flow rates cooling capabilities increase; however, the flow rate must be held below a critical value as steam production is limited by the fuel heat source. At lower temperatures, there is a greater possibility of producing low-quality steam that may damage critical components. Therefore, the water flow rate must be controlled appropriately by setting an upper and lower limit. It must be high enough to meet the thermal requirements and low enough to ensure high quality steam. This problem is further compounded as flight transitions are dynamic; thus, so are these bounds.

To evaluate transient performance of the modeled evaporators, step inputs are applied to the water flow rate. These results are then compared with experimental data for both evaporator designs. In the event the aircraft transitions from high-heating to reduced-heating situations the fuel heat sink must be increased. As discussed above, the TMS meets this requirement by increasing the water flow rate. Thus, with oil simulating the fuel, oil heat loss was observed. However, when the aircraft transitions from high-heating to reduced-heating situations the water flow rate must be reduced, ensuring high-quality steam. Its advantageous to monitor the state of the water using temperature readings. These changes in water flow rate were applied using ramp inputs and model response is evaluated.

$$\tau \frac{d\phi(t)}{dt} + \phi(t) = \phi_{ss} \tag{75}$$

System transients are analyzed assuming a first order response; thus, changes in the varied parameter, $\phi(t)$ can be represented by a first order differential equation with a step input equal to the final steady state value, ϕ_{ss} shown by Eqn. 75.

$$\phi(t) = \phi_{ss} + (\phi_0 - \phi_{ss})\mathrm{e}^{-t/\tau} \tag{76}$$

With the initial value ϕ_0, the solution to this differential equation is shown above, where τ is the time constant. This value describes system response when given a stimulus, such as a step function. From Eqn. 76, a larger time constant results in slower response.

$$Z(t) = \ln\left(\frac{\phi(t) - \phi_{ss}}{\phi_0 - \phi_{ss}}\right) = -\frac{t}{\tau} \tag{77}$$

Eqn. 76 can be rearranged isolating the exponent, t/τ. This term is referenced as the variable $Z(t)$, known as the logarithm of the incomplete response or log-incomplete response, Eqn. 77. Using this equation tabulated values of the measured parameter $\phi(t)$ can be used to determine the time constant, τ. This is shown in Figure 52 referencing a generic data set.

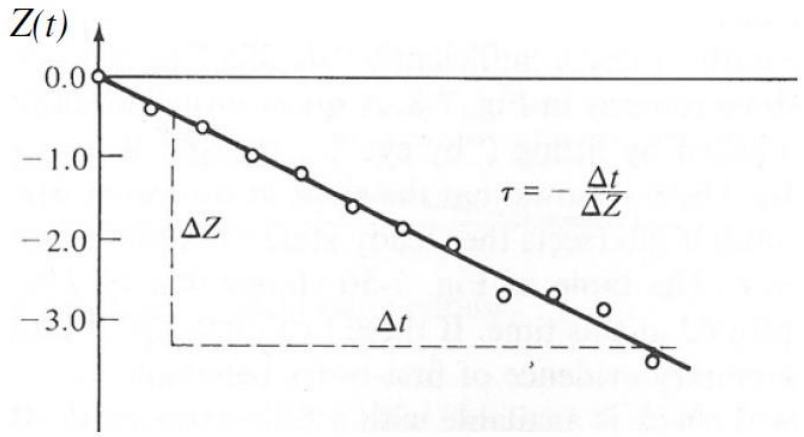

Figure 52: Log-Incomplete response from a generic data set [44].

Assuming a first order response plotting $Z(t)$ will result in a straight line of the form

$$y = mx + b. \tag{78}$$

Confidence in this assumption is based on trend linearity using the coefficient of determination (R^2). However, from Eqn. 77 at $t = 0$, $Z(t) = 0$; thus, the y-intercept drops out. In practice the applied fit will have a y-intercept due to experimental error; thus, it's beneficial to correct this abnormality by forcing it through the origin. This results in Eqn. 79.

$$Z(t) = mt \tag{79}$$

The generic variables, x and y have been reassigned by appropriate terms. This provides an additional equation representing the log-incomplete response where the slope m is defined by a curve fit applied to experimental data. Eqns. 77 and 79 can then be set equal, defining the time constant τ, Eqn. 80.

$$\tau = -\frac{1}{m}. \tag{80}$$

The time constant can be used to plot the resulting trend using Eqn. 76 representing the response of the system. This is shown in Figure 54 overlayed with experimental data.

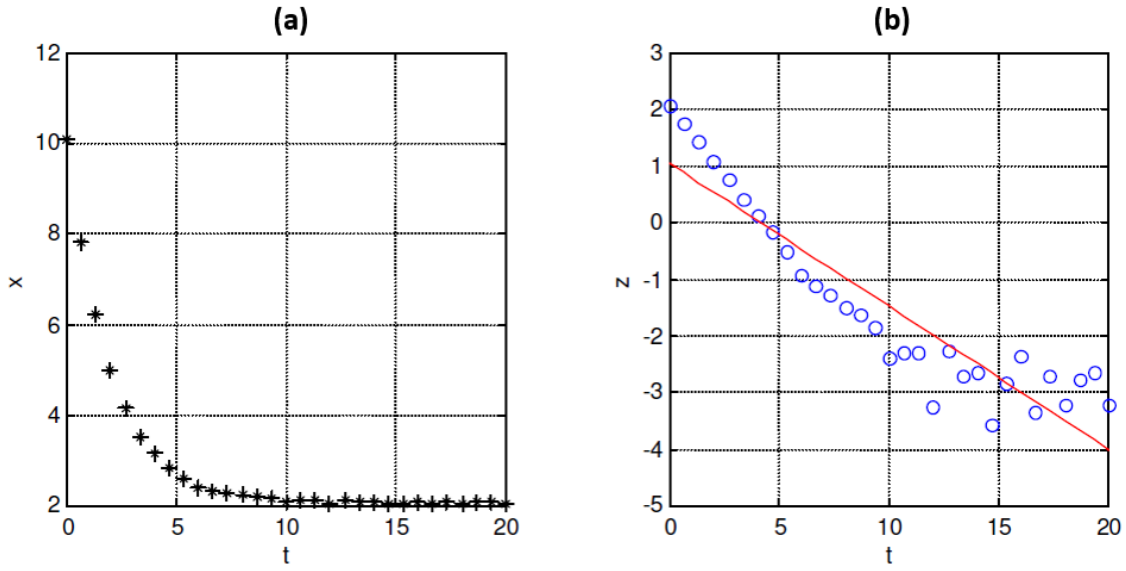

Figure 53: General data set with error (a), and incomplete response with error (b) [44].

The amount of time used to predict the time constant must be selected appropriately. It is dependent on how much noise or random uncertainty is in the data. These fluctuations mask system response, preventing accurate time constant estimates. Therefore, $Z(t)$ is typically plotted until these fluctuations are relative to changes in response. This is shown in Figure 53 (b) at about 10 seconds were the points become inconsistent.

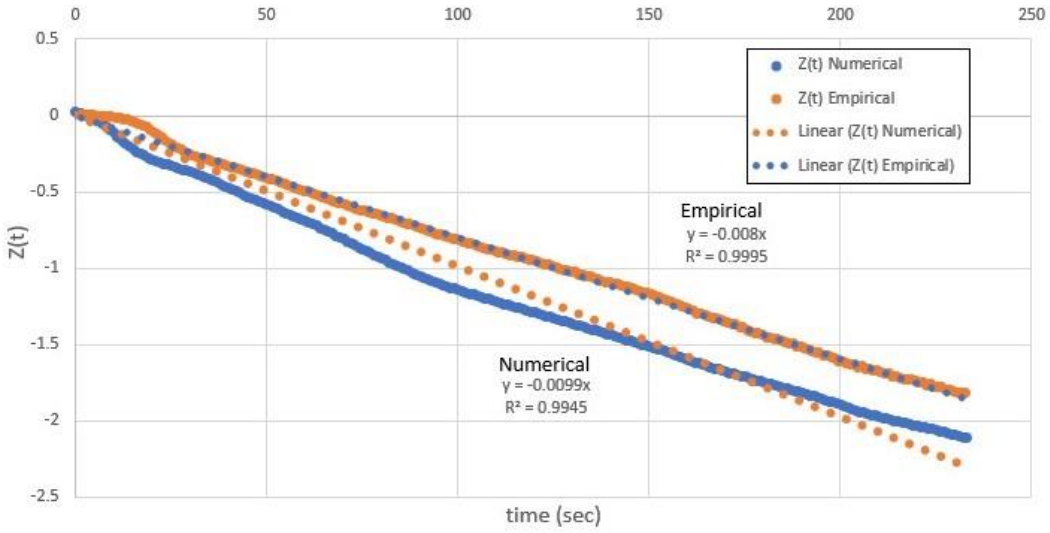

Figure 54: Log-Incomplete response from experimental and numerical results.

Using the procedure discussed above, Eqn. 77 was applied to empirical and numerical results, shown in Figure 54. For both cases the linear fit represents the data well, suggesting a first order response. This log incomplete response was formed using the heat transfer within

the evaporator. Using the slopes from the figure above, Eqn. 80 was used to determine the associated time constants. These defined the empirical and numerical trends shown in Figure 55. These trends can then be compared to evaluate model performance.

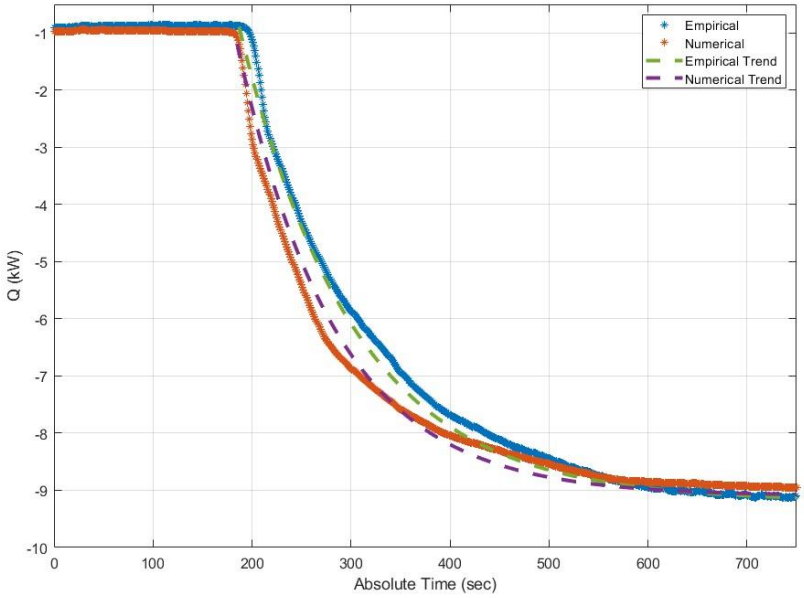

Figure 55: TTHX model transient evaluation using a ramp response.

The model agrees well with experimental data, Figure 55. This experiment was conducted by applying a step input, increasing the water flow rate from $5 \rightarrow 200$ l/min taking about seven seconds to reach steady state. Using an isolated evaporator model, inlet parameters (temperatures, pressures, and flow rates) of the experimental system were directly "fed" into the model. This prevented errors from other modeled components from obscuring the results. To reduce variability a smoothing was applied to the experimental data using a 25-point moving mean. This produced a delay in system response; however, an equivalent moving mean was applied to model input data to provide an accurate comparison. Using the process defined above, time constants for the experimental system and model are 115 and 99 seconds, respectively. This results in the model leading by 9.5%. The representative trends are overlayed in Figure 55 referencing the initial steady state until about 190 seconds when the first order trend begins. This response replicates model performance during an event that requires higher cooling performance. For example, when the aircraft transitions from high-heating to reduced-heating situations. By accurately matching system performance the model can be used to determine system capabilities through more extensive testing determining ideal flow rates during different events.

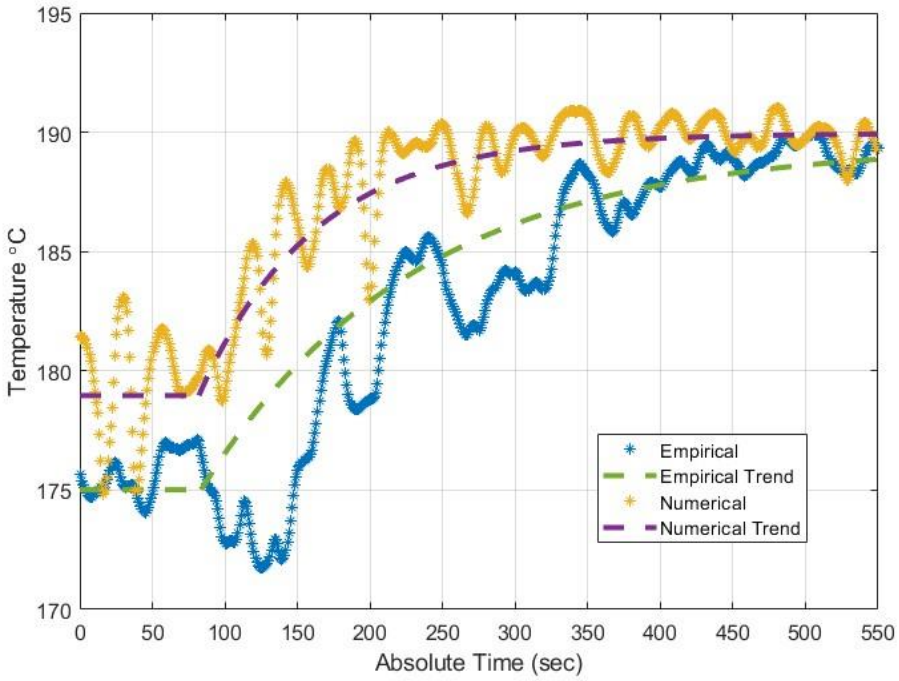

Figure 56: Comparative response of the TTHX by decreasing water flow rate.

The figure above shows a comparison between the experimental system and model in response to step input where the water flow rate was decreased from $265 \rightarrow 260$ ml/min. The time to reach a constant flow rate was about seven seconds. The temperature of the water increases with a decrease in flow rate, primarily because the thermal capacity of the steam decreases. Water flow rate was kept below a critical threshold ensuring superheated vapor at the evaporator exit. This ensures the fluid state was appropriately measured using system sensors. With a saturation temperature of $150\ °C$ the model correctly predicts fluid phase for the entire duration.

The time constants for the system and model are 147 and 121 seconds, respectively. Thus, the model leads the system by about 18%. This is likely due to the assumptions used for model development discussed in Section 4.3.2 Corrugated-Plate Analysis. However, model accuracy is found to be satisfactory, suggesting these approximations are acceptable. Like previously, a 25-point moving mean was applied to the empirical data to assist visual comparison and an equivalent moving mean was applied to the model input parameters ensuring an accurate comparison.

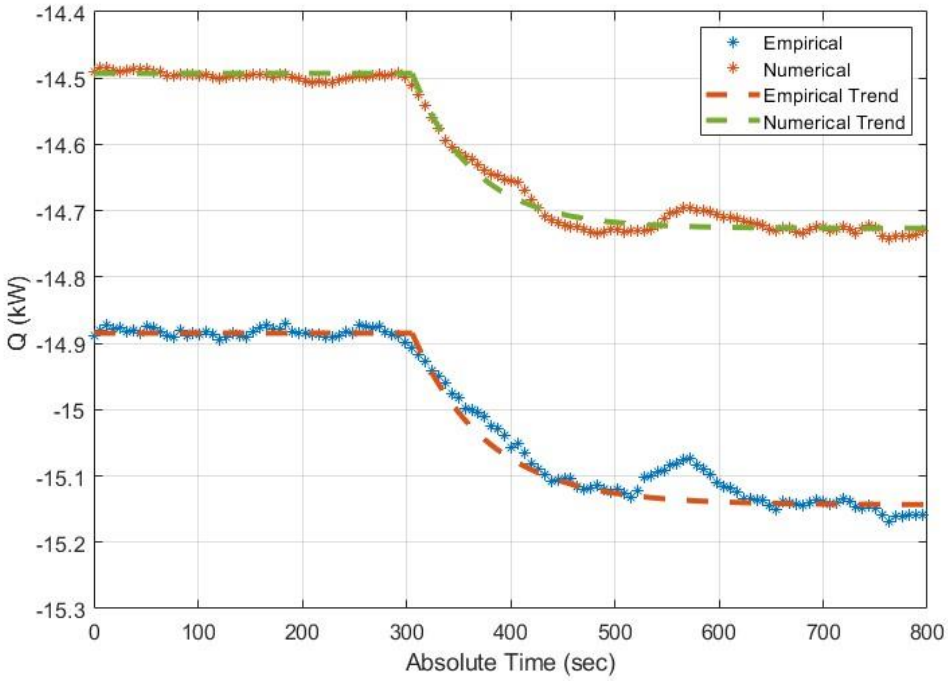

Figure 57: Experimental and numerical response of the CPHX through an increase in water flow rate.

In the figure above, the semi-major axis represents the evaporator performance, or more specifically heat loss of the oil. Changes in performance are again due to changes in water flow rate. This action simulates system response when cooling requirements increase. Comparing experimental and numeral results, time constants are 45 and 72 seconds, respectively. Thus, the model leads by about 36%. As previously mentioned, this likely is due to model simplifications where the correlation developed from oil was used to represent single phase water. Additionally, thermal losses are also not accounted for; thus, the empirical system has greater performance with a discrepancy of 3% in magnitude.

From the process defined above, the evaporator response was assumed first order and the time constants were determined using the log-incomplete response (Eqn. 77). Shown in Figure 57, the trend is initiated at 300 seconds indicating the increase in water flow rate. Experimentally, this took seven seconds, about the same length of time that exists between points. The similarities between results are largely attributed to the experimental data that was used as model inputs, specifically controlling the back pressure and fluid inlet properties (i.e., flow rates, temperatures, and pressures). Furthermore, a 10-point moving mean was applied to the experimental data in the figure to aid the visual comparison. This same moving average was applied to the model input data ensuring the response was comparable.

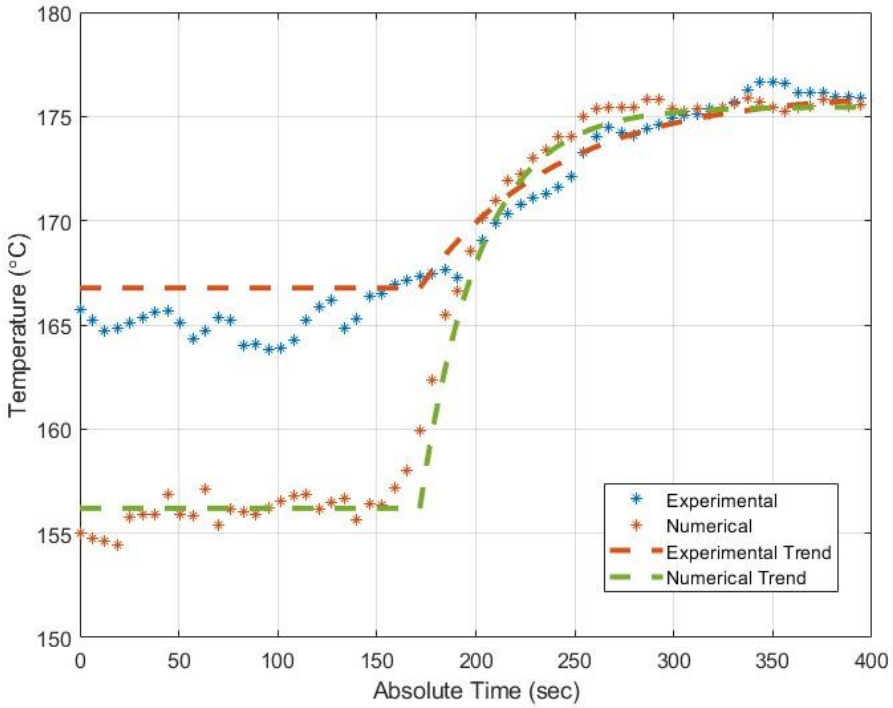

Figure 58: Experimental and numerical results through a decrease in water flow rate.

From Figure 58, the evaporators response shows an increase in steam temperature as the water flow rate is reduced, initiated at about 170 seconds. This ensures high quality steam if the evaporators performance decreases. As discussed previously, this would be during an increase in fuel consumption as the aircrafts transitions from reduced-heating to high-heating operations. Like the case presented above the model leads the experimental results with time constants of 80 and 247 seconds, respectively. This results in a response that is 2.27 times faster. Like the case presented above this is likely due to the correlations used for model development, specifically in representing single-phase convection.

In the event the aircraft flight situation transitions, requirements of the TMS change. These requirements are met by modulating water flow rates, ensuring fuel is within enthalpy bounds and steam is of high-quality. With the evaporator being critical in regulating these parameters, model response is observed, for both heat exchanger designs. Oil heat transfer and water fluid state were monitored ensuring these parameters were within defined limits. With accurate system predictions, ideal water flow rates can be quantified for various transient events. This will provide useful information for system development, specifically quantifying various aspects of the TMS (i.e., power requirements, weight, and ideal control parameters).

4.3 Scroll Modeling

Modeling the scroll expander is crucial in determining power generation and thermal capabilities of the system. The scroll is represented as a generic turbine, an approach that accurately represents the physics within the device and provides a foundation for future applications. The bulk of the model relies on lookup tables based on steady state results where

the following properties are recorded, including isentropic efficiency, mechanical efficiency, and pressure ratio.

$$P_r = f(\omega, \dot{m}) \quad (81)$$

$$\eta_{is} = f(\omega, \dot{m}) \quad (82)$$

$$\eta_{mech} = f(\omega, \dot{m}) \quad (83)$$

Shown by Eqn. 81 through 83 these variables are functions of angular frequency and mass flow rate, resulting in a straightforward data collection procedure because these are controls within the experimental system. Additionally, each variable is a function of the same two parameters; thus, each steady state point collected provides a reference for all three properties.

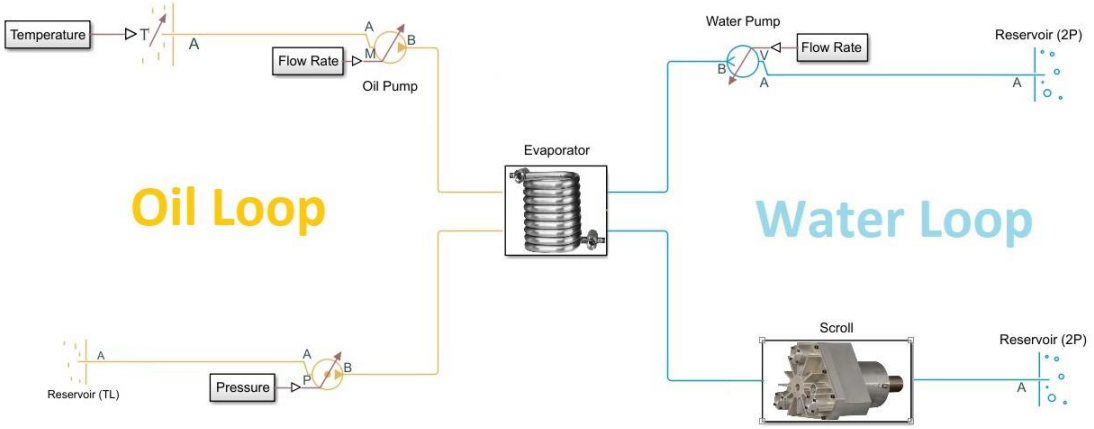

Figure 59: Simulink evaporator and scroll expander evaluation model.

The model used to evaluate the performance of the scroll is shown in Figure 59. This configuration incorporates interactions between the scroll expander and evaporator. Both loops utilize an open configuration where inlet states, flow rates, and back pressures are controlled using empirical values, Fig. 62. This includes the scroll outlet that is set to atmospheric pressure, replicating the open configuration of the system. These configurations simplify the evaluation, presenting an isolated investigation where only the performance of the evaporator and scroll model is considered.

Figure 60: Scroll working process flowchart.

Given controlled inputs of mass flow rate and scroll frequency, all mapped properties are defined; however, recovering the power generated requires a sequence of steps. The workflow process is shown in Figure 60. Using the imposed input parameters $(\omega, \dot{m})$, the pressure ratio can be obtained from tabulated values, specifically referencing the Stodola's constant, a parameter that will be discussed shortly. With pressure ratio defined, and the exit

pressure controlled, scroll inlet pressure is known. This defines the steam inlet state based on evaporator performance. This quantity is then used along with tabulated isentropic efficiencies to determine exit enthalpy. This defines fluid state at the exit and the maximum work potential of the scroll. Mechanical efficiency is then used along with these energetic losses to determine power generated. This sequence of steps provides a conceptual overview of processes that define scroll performance; however, a more detailed description of the theoretical analysis is discussed below.

4.3.1 Scroll Pressure Mapping

As discussed above, the scroll pressure ratio is dependent on angular frequency and mass flow rate, two controls of the experimental system. Thus, pressure ratio can be mapped by varying these parameters through the entire operating range of the device. However, rather than formulating a multi-dimensional look-up table requiring a rather extensive data collection procedure, Stodola's Cone Law was applied. This required varying only one variable (angular frequency). Pressure ratio at different flow rates (off design conditions) were then determined utilizing a proportionality constant, K.

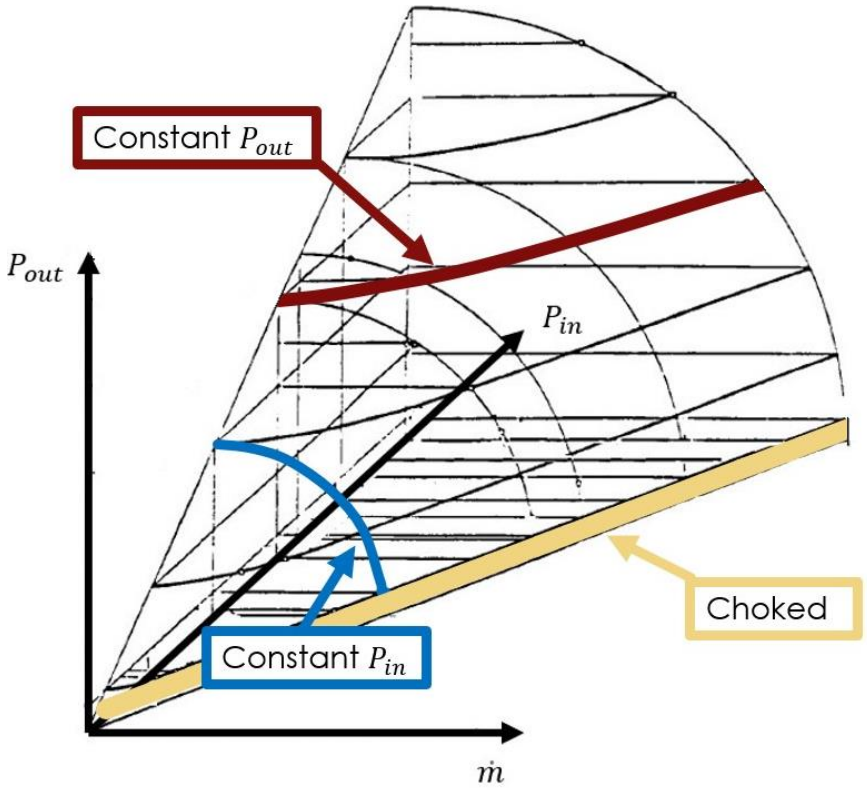

Figure 61: Stodola's cone of steam weights showing property relation contours, adapted from [23].

Stodola's Cone Law relates mass flow rate, inlet pressure, and exit pressure, forming a quadratic surface in the Cartesian coordinate system, Figure 61. With constant exit pressure (P_{out}), mass flow rate $(\dot{m})$ through a turbine evolves based on inlet pressure (P_{in}). This forms

an arc of a hyperbola along the cone surface in planes parallel to $\dot{m}, P_{in}, 0$. The other curved lines form with constant inlet pressure where mass flow rate changes based on exit pressure in the shape of an ellipse. At maximum inlet pressure, this is shown as the cone directrix in Figure 61.

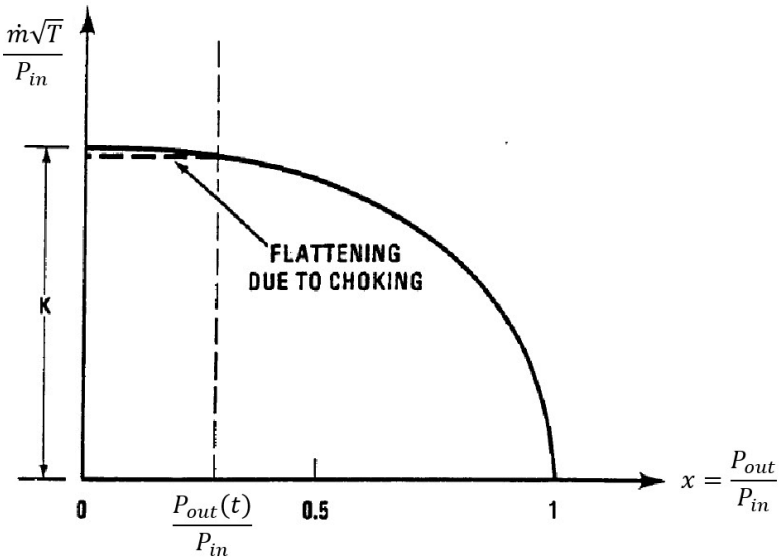

Figure 62: Stodola's ellipse showing relationships between fluid properties for a turbine [24].

Representing Stodola's Cone Law in 2-D form, known as Stodola's ellipse, is achieved by utilizing the flow coefficient, as the semi-major axis, and the inverse pressure ratio as the semi-minor axis, Figure 62. This shows an increasing flow rate until some back pressure $P_{out,t}$ where the flow becomes choked, indicated by the dashed line. This phenomenon is also shown in Figure 61 by the flattened yellow surface. To simplify the modeling approach, the choked condition is ignored, and the elliptical trend is utilized for all simulations. This is due to the Mach number being less than unity for all experimental studies.

$$\frac{\dot{m}\sqrt{T_{in}}}{P_{in}} = K\sqrt{1-\left(\frac{P_{out}}{P_{in}}\right)^2} \tag{84}$$

The curves in Figure 61 and Figure 62 are formed using Eqn. 84 by parametrically varying the independent variable. It was developed experimentally by professor Stodola in 1927 using an eight-stage laboratory turbine. However, it can also be derived theoretically using velocity triangles and flow-work relations [23]. The law of the ellipse originally determined flow properties through a multistage turbine with several flow extractions through its length. These reductions in flow rate cause a decrease in inlet pressure to each subsequent turbine. With flow rate and back pressure known, Eqn. 84 can be used to define the pressure ratio. However, the proportionality constant, K must be predetermined before this can be realized.

$$K = \frac{\dot{m}_d \sqrt{T_{in,d}}}{\sqrt{{P_{in,d}}^2 - {P_{out,d}}^2}} \tag{85}$$

This is defined by rearranging Eqn. 84, shown by Eqn. 85 where all flow properties were obtained at the design flow rate, (one with the most uptime). However, because the properties of the experimental system change with scroll rotational speed, a function was developed based on the operating range of the component.

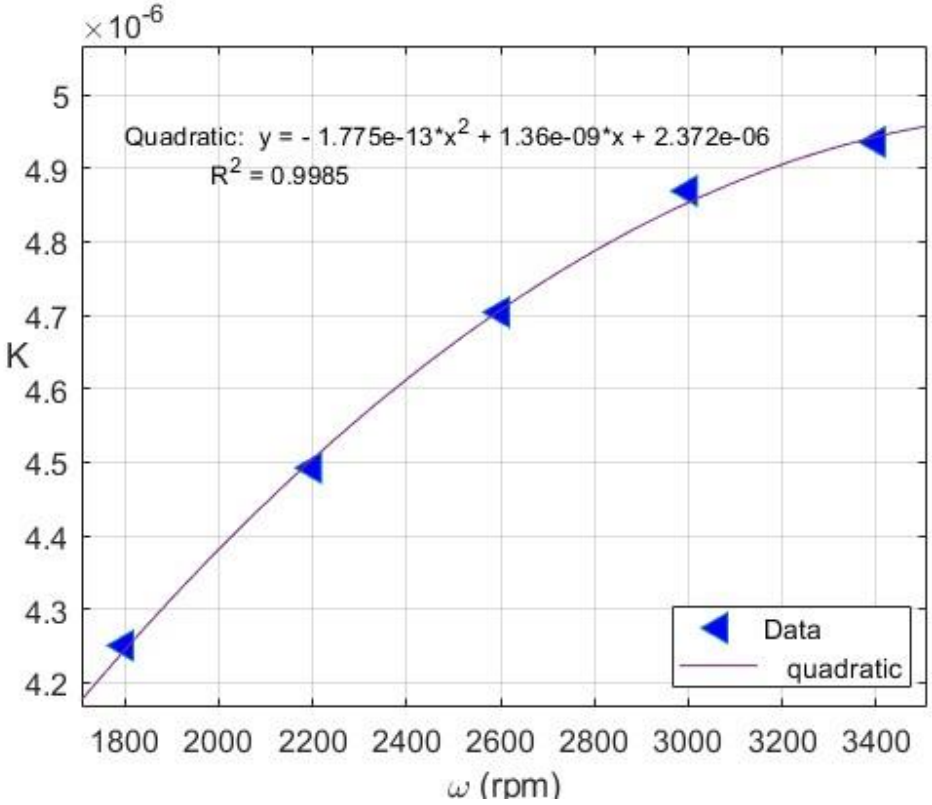

Figure 63: Proportionality constant, K determined for a range of scroll speeds.

By only varying rotational speed the proportionality constant changes in the form of an inverse relationship, Figure 63. This evaluation involved 5 design set points with water flow rate held constant at 260 ml/min, and scroll speed varied from $1800 \rightarrow 3400$ rpm. The quadratic curve fit accurately represents the data based on the coefficient of determination (R^2) . This provides the required lookup table to calculate the appropriate constant for off design flow rates (i.e., $\dot{V} \neq 260$ ml/min).

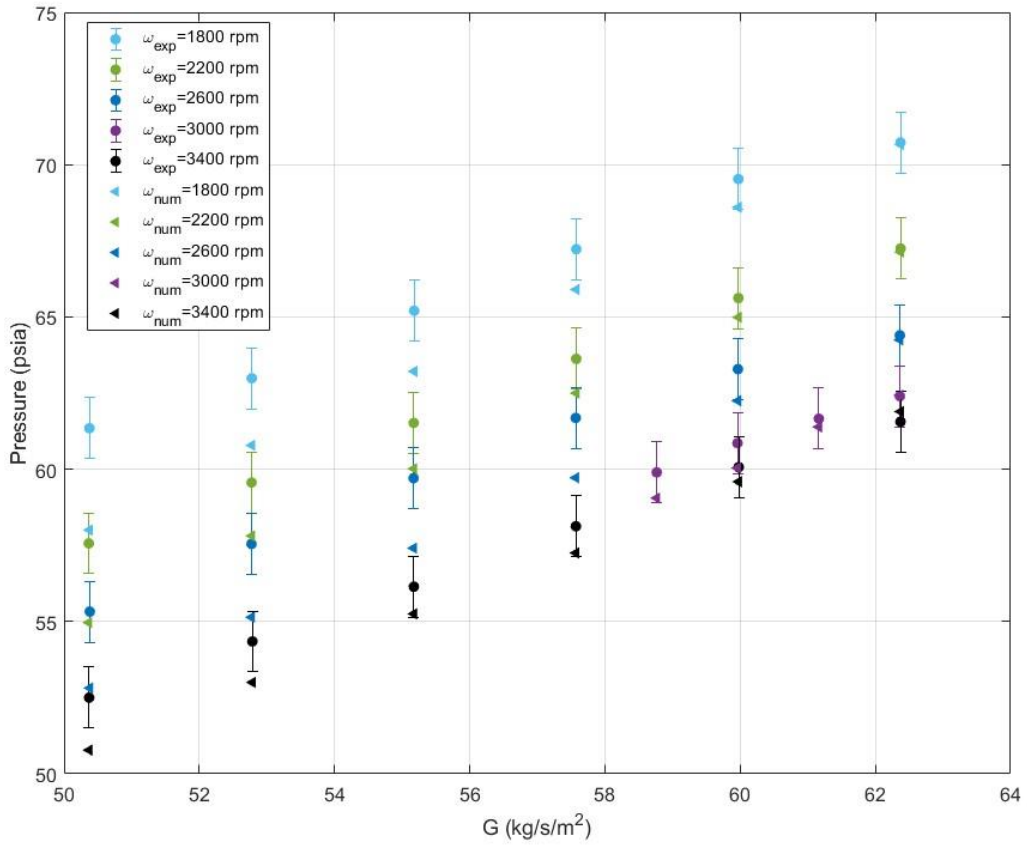

Figure 64: Off design performance evaluation of the Stodola's ellipse relation

With the lookup table empirically derived, the scroll inlet pressure can be calculated for off design flow rates using the Stodola's ellipse relation. The performance of this approach is shown in Figure 64 for 5 different water flow rates and 5 different scroll speeds totaling 25 different steady state points. The results show comparable trends where higher flow rates and lower scroll speed increase pressure. Magnitudes are also comparable showing an RMS and maximum error of about 2% and 5%, respectively. The greatest accuracy is shown at the design flow rate where all points are within the experimental uncertainty of the system. The greatest inaccuracies are at lower flow rates, furthest from design condition.

4.3.2 Isentropic Efficiency Mapping

Due to system configurations, evaporator performance is dependent on back pressure induced by the scroll. Specifically, because pressure influences enthalpy of vaporization. With pressure obtained using Stodola's ellipse relation, temperature downstream of the evaporator is defined based on evaporator performance. Mapped isentropic efficiencies then quantify enthalpy change through the scroll defining fluid state at the exit since pressure is known.

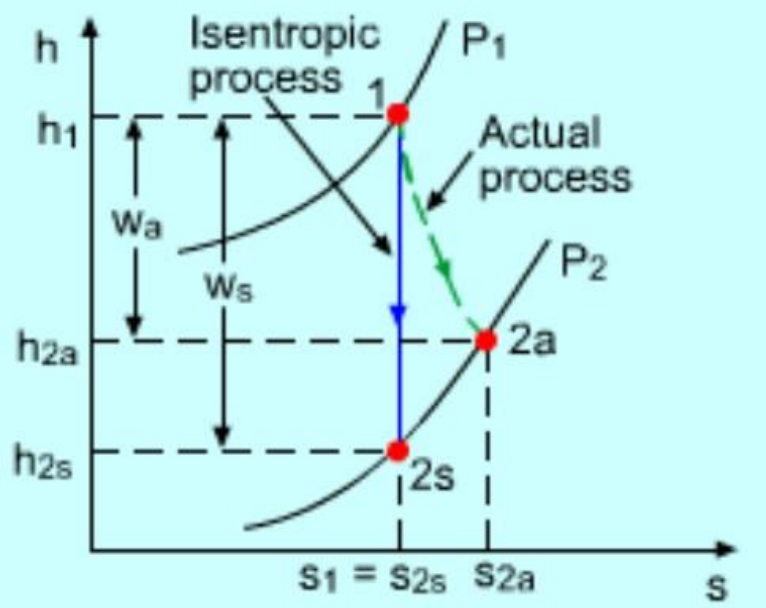

Figure 65: H-S Mollier diagram, comparing the isentropic process with the actual expansion.

Isentropic efficiency is often used in thermodynamic cycles as it relates the actual work potential of a given process with work obtained at isentropic conditions. An isentropic expansion results in greater work compared to the actual process, Figure 65. This idealized thermodynamic cycle assumes all energetic changes are converted into useful work. There is no thermal loss, total pressure loss, nor any energetic conversions to lower forms of energy, such as kinetic to thermal changes due to friction. However, no physical process is without some irreversibility. Thus, the actual work is always less than the theoretical maximum. This is shown in Figure 65 where the actual process shows a lower enthalpy change, presenting the maximum work that can be extracted from the heat engine. For the case of the Rankine cycle system, this not only limits power generated but also cooling capabilities during closed cycle operation. Accurately mapping this parameter is crucial to providing an accurate account of system performance.

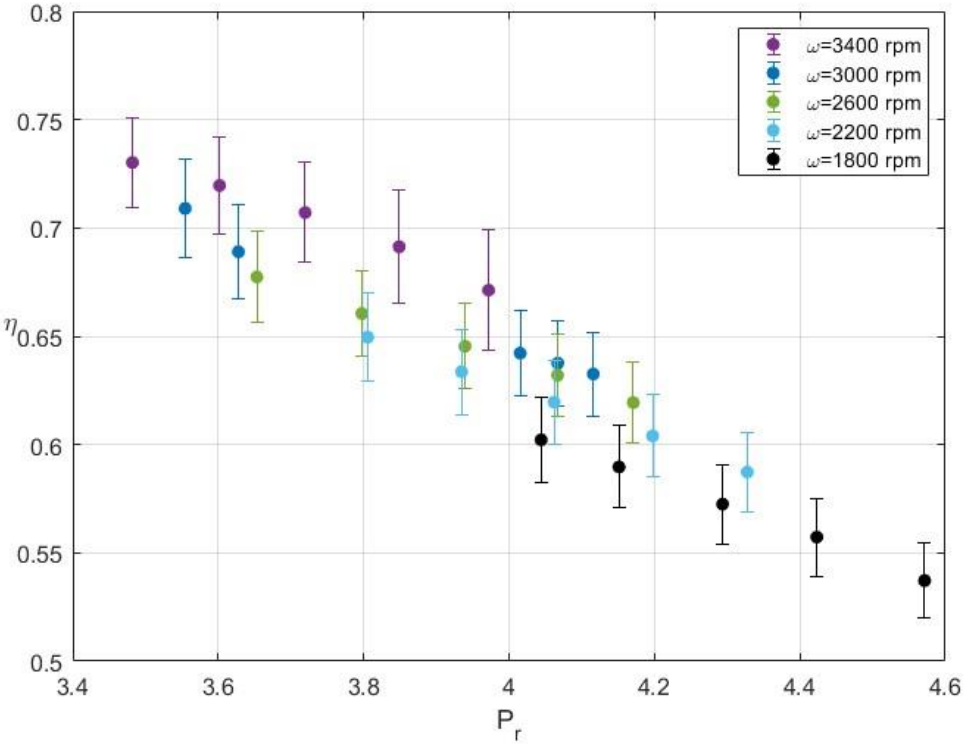

Figure 66: Tabulated isentropic efficiencies for the scroll expander at various speeds.

$$\eta_{iso} = \frac{h_2 - h_1}{h_{2s} - h_1} \tag{86}$$

The isentropic efficiency of the scroll expander was calculated for a variety of steady state points where pressure and temperature readings defined fluid enthalpy, shown by Eqn. 86. Results in Figure 66 were obtained varying scroll speed from $1800 \rightarrow 3400$ rpm, and water flow rate from $210 \rightarrow 260$ ml/min. This encompasses scroll performance during typical operations. From the figure above, all trends show increasing efficiency as scroll speed is increased, and flow rate is reduced. This ultimately decreases pressure ratio, a main "driver" for scroll efficiency. At 3400 RPM and 210 ml/min the pressure ratio was lowest resulting in peak efficiency. This is the minimum pressure needed to turn the scroll, overcoming bearing friction and magnetic forces within the eddy break.

Table 2: Mapped isentropic efficiency as a function of pressure ratio and rotational speed.

Speed (rpm)	Curve Fit	R^2	RMSE
1800	$y = -0.1192x + 1.148$	0.9864	54.2×10^{-3}
2200	$y = -0.1340x + 1.167$	0.9872	7.82×10^{-3}
2600	$y = -0.1107x + 1.082$	0.9995	1.04×10^{-3}
3000	$y = -0.1180x + 1.098$	0.9994	1.21×10^{-3}
3400	$y = -0.1123x + 1.098$	0.9991	1.51×10^{-3}

Scroll efficiency is dependent on pressure ratio and scroll speed. Therefore, mapping isentropic efficiency required the development of a multidimensional table. As Figure 66 presented, at constant scroll speed, data was accurately represented by linear trends. This is based on the coefficient of determination and RMSE, shown in Table 2. The accuracy of this approximation is largely influenced by the narrow operating range of the system, specifically where steam production is limited leaving a narrow range of inlet pressures. If a larger range is utilized this linear approximation must be reevaluated.

Developing trends for a constant pressure ratio; however, is more complex. This is because it is not feasible to collect data at constant inlet pressure because it is not a controlled parameter. Therefore, a linear trend was used to represent isentropic efficiency with constant pressure ratio as this offered a simple representation. Fortunately, due to the narrow scroll performance, this approximation yielded low uncertainty. This provides the second set of constraints required to map isentropic efficiency. Thus, isentropic efficiency was represented by a dual set of linear trends formulating a two-dimensional interpolation table based on pressure ratio and scroll speed.

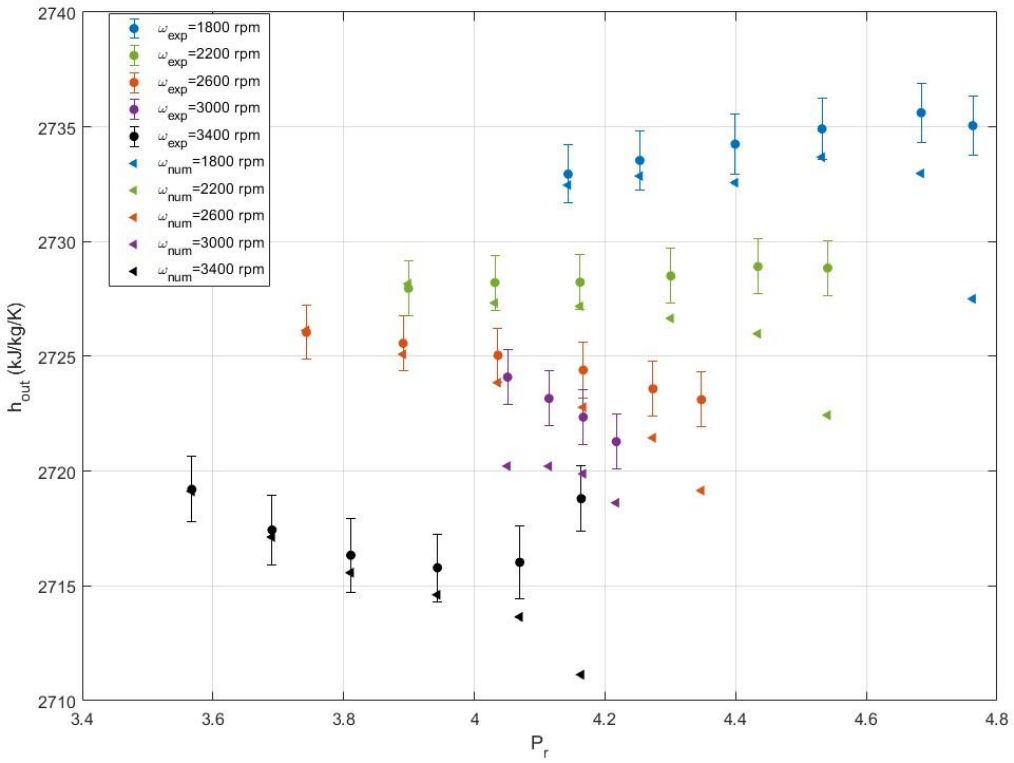

Figure 67: Enthalpy diagram comparing the experimental and numerical results.

With fluid properties defined at the scroll inlet and exit, mapped isentropic efficiencies quantify fluid enthalpy at the scroll exit. Model performance is shown in Figure 67 overlayed with experimental data. These points incorporate the same range of parameters that map scroll efficiency. Empirical uncertainty was developed based on systematic and random error in the derived steady states points, Appendix D. However, errors associated with the model are not

produced by the mapped parameter alone. Additional errors are incurred by misrepresenting pressure ratio with the Stodola's ellipse relation. Furthermore, incorporating the evaporator component also induces error as the predicted inlet fluid state is not exact. This source of error could be excluded if the inlet state was prescribed rather than utilizing the evaporator model. Unfortunately, in practice this results in solving instabilities as the pump model approximates the required pressure needed to pump superheated vapor. Therefore, the evaporator model was included. Despite these sources of error, the model was found to agree well with the empirical results where the RMS and maximum error was $4.2\ \mathrm{kJ/kg\ K}$ and $8.2\ \mathrm{kJ/kg\ K}$, respectively. This suggests the mapped isentropic efficiency accurately predicts exit enthalpy within this operational range.

4.3.3 Mechanical Efficiency Mapping

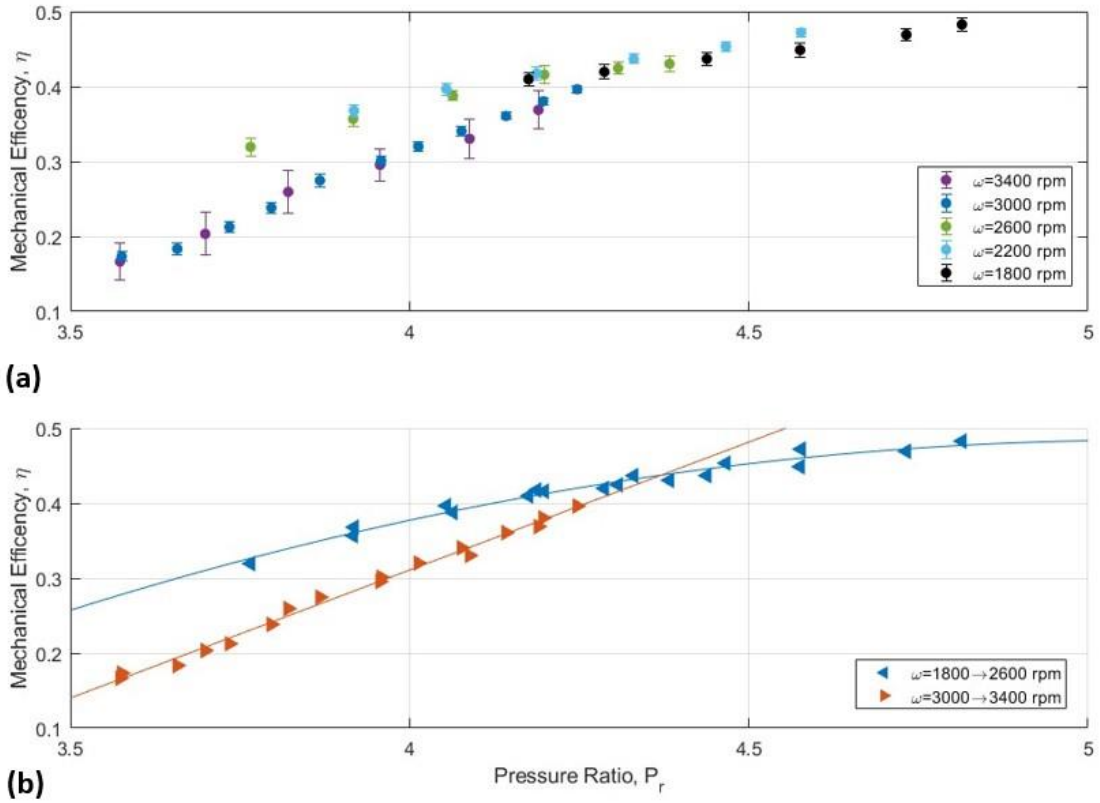

Figure 68: Mechanical efficiencies of the scroll expander (a) and predominate trends (b).

$$\eta_{mech} = \frac{\dot{W}_{shaft}}{\dot{Q}} \tag{87}$$

As shown by Eqn. 87, mechanical efficiency is calculated using energic changes of the steam, $\dot{Q}$ as a normalizing factor. Irreversibility's including friction, uncontrolled vibrations, nonadiabatic effects etc. leading to an efficiency less than unity. The values shown in Figure 68

were formulated by varying the scroll speed and water flow rate from $1800 \rightarrow 3400$ rpm and $210 \rightarrow 260$ ml/min, respectively. The predominate trend shows a direct relationship with pressure ratio regardless of scroll speed. Emphasized in Figure 68 (b) two trends provide a reasonable fit for all speeds, supplying the necessary information to map mechanical efficiency. These minor differences are attributed to variations in irreversibly where at higher speeds greater losses are experienced by the device leading to lower efficiencies, shown in Figure 68.

Table 3: Mapped mechanical efficiency as a function of pressure ratio and scroll speed.

Speed (rpm)	Curve Fit	R^2	RMSE
$1800 \rightarrow 2600$	$y = -0.089x^2 + 0.92x - 1.8$	1.000	2.16×10^{-15}
$3000 \rightarrow 3400$	$y = 0.341x - 1.05$	1.000	4.55×10^{-15}

The equations from Table 3 are used to define mechanical efficiency within the indicated range of speeds. These equations map scroll performance through typical operations of the experimental system. Values that fall between these ranges were interpolated using a cubic function preventing sudden changes in mechanical efficiency, increasing the stability of the solver. The performance of these trends is assessed based on the coefficient of determination and RMSE, found to be near unity and zero, respectively, Table 3. This suggests the chosen curves agree with the experimental data.

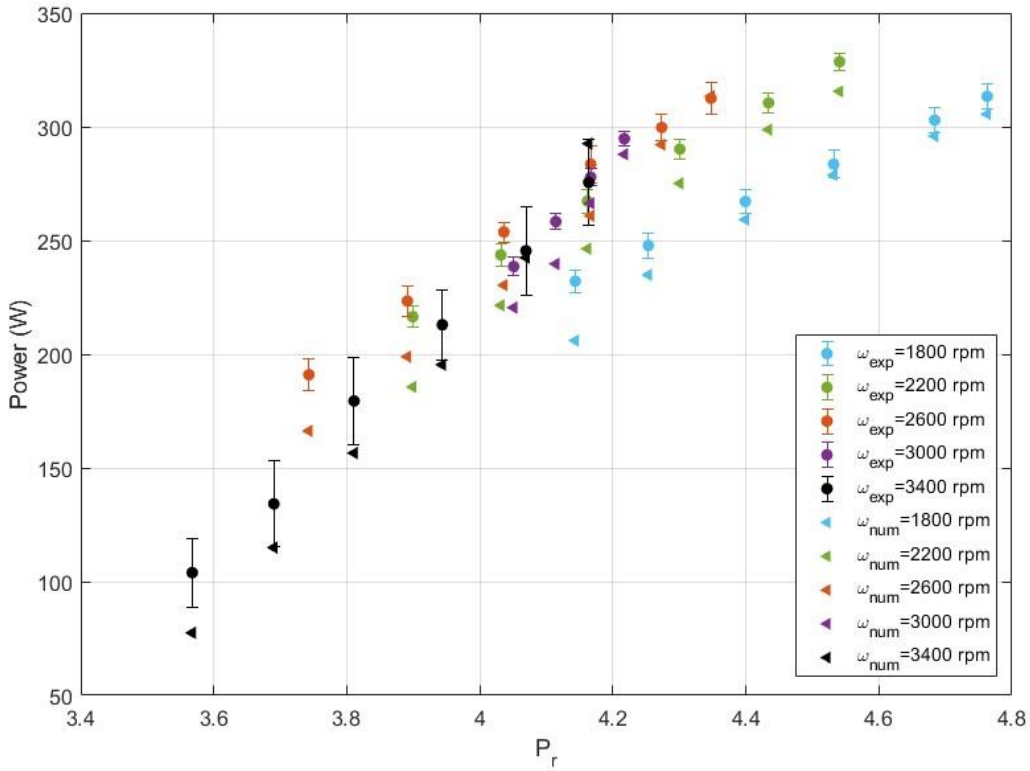

Figure 69: Scroll expander performance comparing numerical and empirical results.

As discussed above, mapped isentropic efficiency defines the energic changes through the scroll expander, representing the maximum shaft power of the device. With this defined Eqn. 87 can be used to calculate the actual power using the mapped mechanical efficiency curve fits, Table 3. The performance of the model is shown in Figure 59 covering a range of scroll speeds and pressure ratios, incorporating 28 steady state points. All trends are found to match empirical results where an increase in power is largely attributed to higher pressure ratios. In magnitude, the model is found to represent the data well, evaluated based on RMSE and maximum error, 10.1% and 25.1%, respectively. However, in representing mechanical efficiency as a function of pressure ratio, any error in the determination of pressure will be met with inaccuracies in power. This is visualized by comparing the performance of pressure from Figure 64 with scroll power in Figure 69 where the largest discrepancies are at off design conditions at lower pressures. This highlights the importance of developing mapped parameters based on the design conditions of the device. Inaccuracies in one mapped parameter can influence another with an amplifying effect.

V. Vehicle Level Modeling

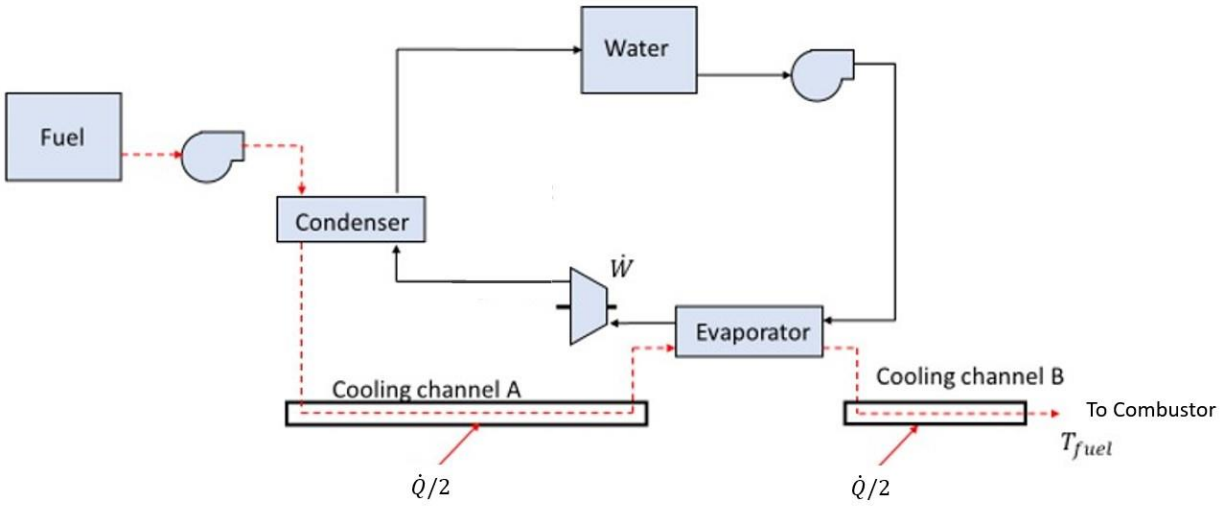

Figure 70: Component diagram of the Rankine cycle system during closed configuration

The components of the Rankine cycle system are shown in Figure 70. The foremost function of this TMS is to provide thermal cooling and power generation for an aircraft. Two primary components used to define system capabilities are the evaporator and scroll expander. Due to their complexity, it was found that these components were not accurately represented using available models. Thus, custom components were developed using experimental data. However, custom models were not developed for the tanks, pumps, condenser, nor the cooling channels. This was primarily because these components were well represented using available models. Specifically for the condenser and cooling channels, these blocks incorporate a variable heat flux where heating rates are applied as input parameters. Built-in pump blocks work the

same way where flow rate is a controlled parameter. The physical water and fuel tanks are modeled using an infinite reservoir with an initially prescribed fluid state. This briefly describes the individual component blocks used to assess system performance during closed cycle operations; however, a more detailed description of the input parameters and results of the implemented model is discussed below.

To evaluate the TMS for aircraft applications a heating profile was generated. To maximize cooling capabilities the overall heat load, $\dot{Q}$ was divided (nonequally) between two cooling channels, ensuring the fuel thermal limit was reached at each outlet. This assumed the system must be designed to maximize cooling capabilities, a governing ideology for high-speed vehicle design [50]. This procedure was specific to reduced-heating operations where a lower flow rate causes the fuel to reach the thermal limit, unlike when the aircraft is the high-heating configuration. Once the overall heat load was determined, the cooling potential at high-heating was calculated using the appropriate scaling equation, as discussed below.

Table 4: High-speed aircraft relations comparing parameters between flight situations.

Fuel Flow rates	$\dot{m}_{hh} = 3\dot{m}_{rh}$
Cooling Requirements	$\dot{Q}_{hh} = \frac{3}{2}\dot{Q}_{rh}$
High-Heating Power	$\dot{W} = \frac{1}{60}\dot{Q}$
Reduced-Heating Power	$\dot{W} = \frac{1}{100}\dot{Q}$

Shown in Table 4, various operating ratios are used to determine input parameters for the vehicle scaled investigation. These equations reflect generic requirements for a high-speed reusable aircraft. From the first two rows, these equations describe the relationship between two different heating profiles. As shown, fuel requirements at high-heating are specifically three times higher. Shown by the third and four row, power requirements, $\dot{W}$ are defined in terms of thermal loads, $\dot{Q}$. These relations define the required system efficiency for the indicated flight situation. Comparing the two requirements, system efficiency must be greater during high-heating operations. This is due to the increase in pump requirements needed to triple the fuel flow rate.

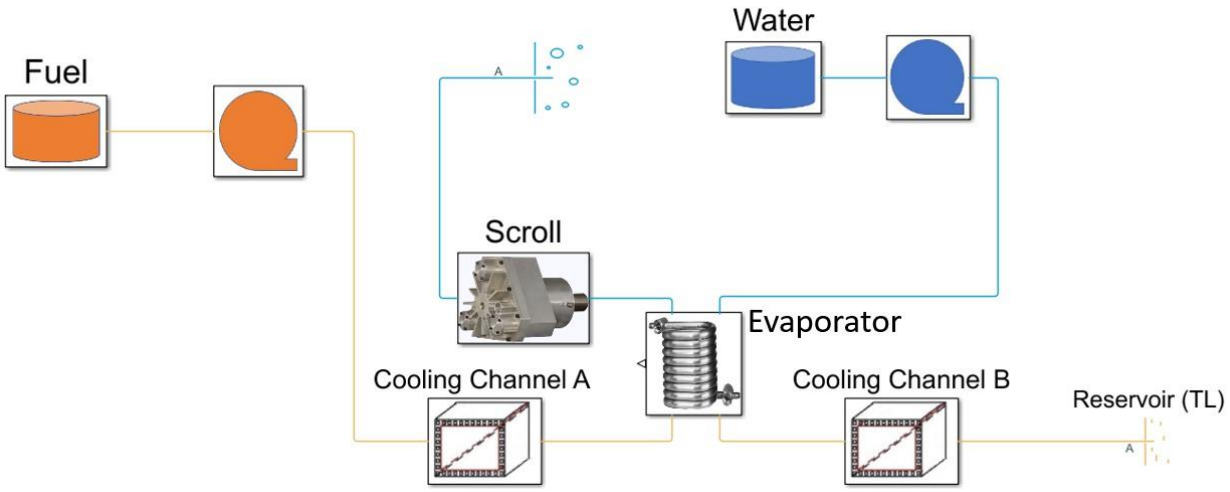

Figure 71: Vehicle level model investigating system performance using scaled input parameters.

From Figure 71, the vehicle level model incorporates two custom components based on the experimental system i.e., the tube-in-tube evaporator and scroll expander. To ensure an accurate prediction of steam production and power generation, model inputs were set within the limits of the development components. For the evaporator, these were flow rates and inlet fluid temperatures. For the scroll, angular velocity and water flow rate are specified. However, utilizing parameters within these ranges was not possible using every component from Figure 70; thus, the scaled model was simplified to ensure this could be achieved.

From Figure 71, the model does not appear to represent the closed configuration where cold fuel drawn from the tank condenses low pressure steam. Instead, the model incorporates an open water loop without the inclusion of a condenser. To replicate the condenser, energetic changes of the steam (specifically between the exit of the scroll and water tank) was added to fuel within the first cooling channel. This not only simplified the model, not requiring a condenser component, but ensured modeled components were within their predefined accuracy.

At the prescribed flow rates (steam and fuel), the fuel was unable to act as a condensing agent. Its capacity rate was insufficient, and the fuel reached saturation temperature preventing condensed steam. This could have been prevented by adjusting model inputs. For example, the fuel flow rate could be increased; however, through a modeled evaluation doing this resulted in flowrates that exceeded the range of the evaporator model. It was also noted that the condensing pressure could be increased thereby increasing the condensing temperature or the temperature difference between fluids. However, this required a back pressure that exceeded the range of the scroll model. Therefore, either of these approaches resulted in flow parameters that were beyond the range of the model and instead inefficiencies in the condenser were removed from the analysis. This discovery suggests the benefits of increasing the range of these components to ensure a complete replication of the Rankine cycle

system. However, further experimental mapping would need to be performed and is not discussed in this thesis but as future research.

Table 5: Input model parameters defined using scaled ratios from Table 4

High-Heating Fuel FR	$\dot{m}_{fuel} = 21 \times 10^{-3}$ kg/s
High-Heating Water FR	$\dot{m}_{watr} = 3.92 \times 10^{-3}$ kg/s
Reduced-Heating Fuel FR	$\dot{m}_{fuel} = 7 \times 10^{-3}$ kg/s
Reduced-Heating Water FR	$\dot{m}_{watr} = 4.33 \times 10^{-3}$ kg/s
High-Heating Thermal Load	$\dot{Q}_{hh} = 21$ kW
Reduced-Heating Thermal Load	$Q_{rh} = 14$ kW

The equalities shown in Table 4 were used to perform the vehicle scaled investigation. However, these did not specify model inputs but rather provided the equations needed to relate the two flight situations. Instead, most of the values from Table 5 were defined based on the operating range of the experimental system, thereby ensuring flow rates and steam temperatures were within range of the scroll model. Thus, to stay within this range and to maximize system cooling the upper range was used with $\dot{m} = 4.33 \times 10^{-3}$ kg/s and $T_{out} = 180$ °C. However, steam temperature (T_{out}) is not a set parameter, it dependents on fuel flow rate and fuel temperature through the evaporator. Thus, these independent parameters were defined producing the desired steam temperature while maximizing system cooling. To do this fuel temperature was set to the thermal limit ($700°C$) allowing the greatest heat transfer within the evaporator during reduced-heating situations. With this set, the fuel flow rate was determined such that the desired steam temperature was achieved resulting in $\dot{m} = 7 \times 10^{-3}$ kg/s, Table 5.

The heating needed to reach the fuel thermal limit was applied within the first cooling channel block, Figure 71. This defined all set quantities during the reduced-heating configuration. As discussed above, model inputs were first developed for this flight rescheme because cooling requirements are higher. This can be inferred using the results from Table 4. When transitioning from high-heating to reduced-heating, channel heating, $\dot{Q}$ is reduced to $1/2$ but the heat capacity rate ($\dot{m}c_p$) is reduced to $1/3$.

$$T_{out} = \frac{\dot{Q}}{\dot{m}c_p} + T_{in} \tag{88}$$

Therefore, fuel temperature (T_{out}), Eqn. 88, will be higher at reduced-heating and maximum cooling capabilities must be first set for this operation to ensure the fuel is below the thermal limit. The scaled equations from Table 4 were used to define parameters during the high-heating configuration, specifically, channel heating and fuel flow rates. This does not include the water flow rate, the only parameter left to be defined. With all fuel-side properties set, water flow rate was controlled to produce the desired steam temperature with $T_{out} = 180°C$. This ensured high quality steam and maximum power production.

The process described above was used to define all input parameters to the vehicle scaled model, except heating within the second cooling channel. This was determined using a similar process as the first cooling channel where the fuel was set to the thermal limit during reduced-heating operations. The scaled ratios from Table 4 was again applied to determine heating during the high-heating configuration. Thus, all steady state input parameters to the model are defined; however, system response must still be quantified to ensure an accurate account of system performance during transient operations.

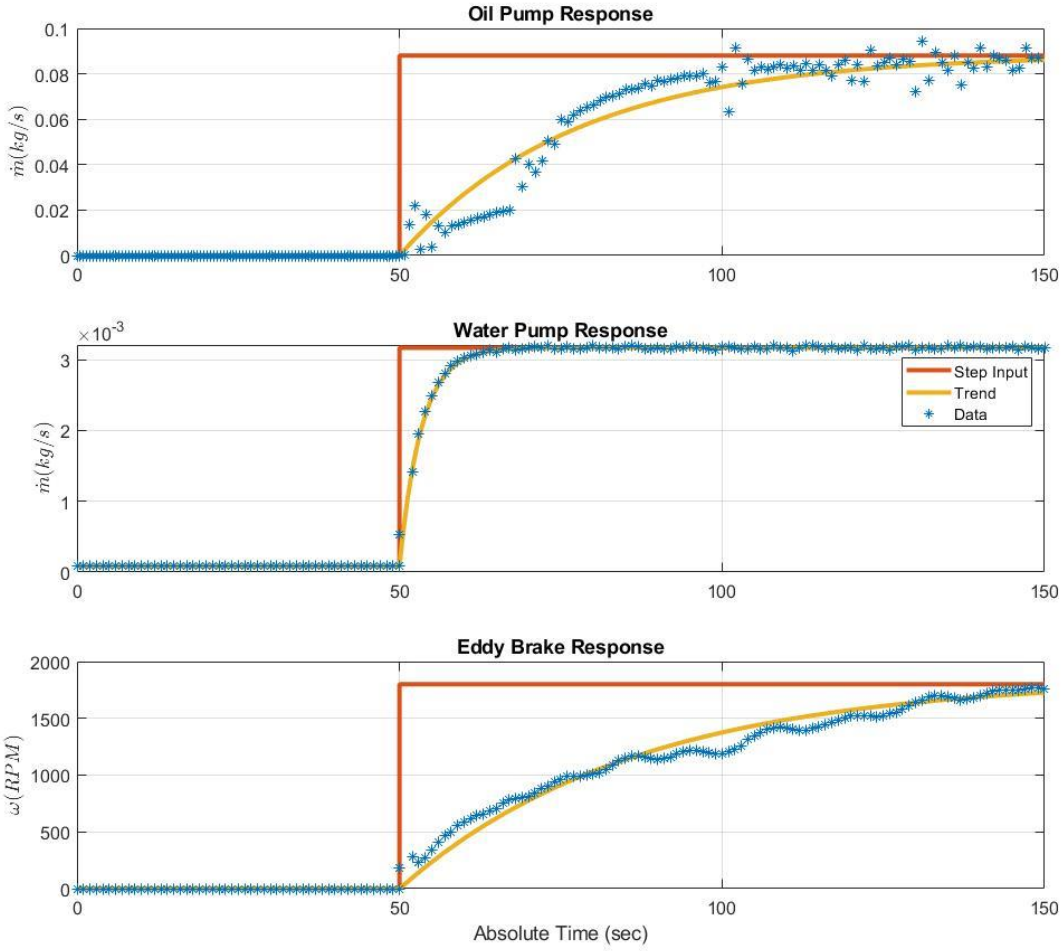

Figure 72: Response of the experimental system to an applied step input overlayed with the representative first-order transfer function.

Predicting capabilities of the system becomes more complex during transient situations. For example, when the aircraft transitions from high to reduced heating operations. Instead of single, steady state values representing system parameters (e.g., fluid states, flow rates, shaft speeds, etc.) each parameter changes with time. In fact, many parameters are dependent on

each other resulting in a complex network of variables. Thus, theoretical models may be insufficient and instead experimental results can be used to assess system response.

Empirical data was used to develop transfer functions, specifically representing the response of the oil and water pumps, as well as the eddy brake in the experimental system, Figure 72. These transfer functions were then used to represent component response of the vehicle scaled investigation. Clearly, these functions do not represent the performance of the final aircraft TMS but instead present a simplistic approach that captures transient effects of the current experimental system. Thus, when modifications and/or improvements are made system capabilities can be quickly assessed using this approach.

Table 6: Transfer functions developed based on empirical data, Figure 72

Component Response	Transfer Function	R^2
Oil Pump	$\frac{0.03667}{s + 0.03652}$	0.8981
Water Pump	$\frac{0.293}{s + 0.2929}$	0.9874
Eddy Brake	$\frac{0.02802}{s + 0.02731}$	0.9202

The trends representing transient performance of the oil pump, water pump, and eddy break were developed using MATLAB's system identification toolbox. This application develops transfer functions based on user defined input functions and resulting response of the system. All inputs are step functions, and the response of the experimental system is delayed, Figure 72. The empirical trends are primarily dependent on component capabilities, managed by parametrically tuned PID controllers. For simplicity, these trends were assumed first order and performance of this assumption was based on coefficient of determination (R^2) , shown in Table 6. From these results the transfer functions adequately describe system transients, representing more than 89% of variance (σ^2) in the semimajor axis for each case. This means most of the changes in the dependent variable can be predicted by the independent variable using this first-order relationship.

With these transfer functions developed the scaled parameters from Table 6 were used as step inputs, thereby providing the required delay to replicate system response. The resulting arrays were then utilized as input parameter to the vehicle scaled model, simulating transient performance of the experimental system. Mission duration was taken to be 20 minutes to ensure enough time to reach steady state after transitioning from high to reduced heat loads.

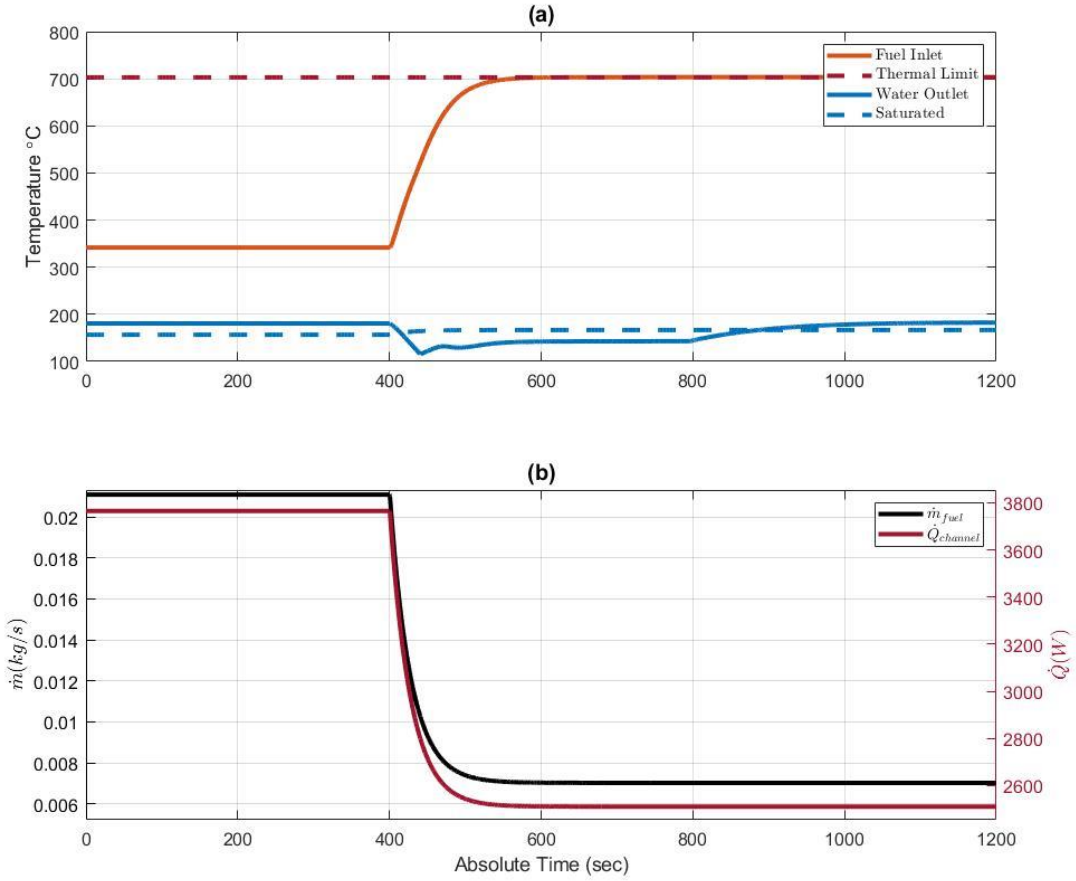

Figure 73: Evaporator inlet properties and temperature limits (a) and fuel flow rate and heating within the first cooling channel.

Shown in Figure 73 (b) two model input parameters change at 400 sec. In fact, at this instance all input parameters change including, fuel and water flow rates, channel heating, and scroll speed using the developed transfer functions from Table 6. However, to simplify the analysis a transfer function was not developed for channel heating. Instead, it was assumed to be related to the fuel flow rate, as this controls combustion rate and or combustion temperature influencing the total heat load. Thus, for discussion purposes the oil transfer function was used to represent channel heating as well. This can be visualized by comparing trends between the fuel flow rate and channel heating during the transition in Figure 73 (b).

Steady state results defined optimal water flow rates, maximizing power, and ensuring high quality steam. However, from Figure 73 (a) during the transition steam dips below the saturation temperature indicating subcooled water is entering the turbine. This clearly violates system requirements as this can damage critical components and produce a loss of power. This occurs because overall heating is insufficient. The film coefficient within the evaporator decreases due to a sudden change in flow rate but the increase in fuel temperature is delayed.

As discussed in section 4.3.2 Corrugated-Plate Analysis), the film coefficient is a function of the Reynolds number, a dimensionless parameter directly dependent on flow rate. Thus, when flow rate is reduced, heat transfer immediately decreases. To offset this the fuel temperature is increased but because there is a fluid volume within the evaporator there is a delay in reaching the desired mean temperature. Thus, the mean fuel temperature is too low to overcome the immediate convective deficit and the water fails to evaporate. However, once the mean fuel temperature reaches steady state, superheated steam is produced. This is shown in Figure 73 (a) when the water temperature dips below the saturation temperature.

Prior steady state analysis was used to determine ideal water flow rates for the system; however, these input parameters are insufficient during transient operations. There are various ways of preventing the steam from becoming saturated. Most methods include adjusting input parameters to the vehicle scaled model, such as, using a ramp function to provide a more gradual transition for all input parameters, and or increasing channel heating to raise fuel temperature. However, the given inputs have been imposed purposively to simulate aircraft operations, except the water flow rate. Another words, fuel flow rates, channel heating and system response have all been formulated to replicate the properties of the scaled vehicle, but the water flow rate is left as a control of the TMS. Therefore, this is the only input parameter that should be augmented to produce high quality steam.

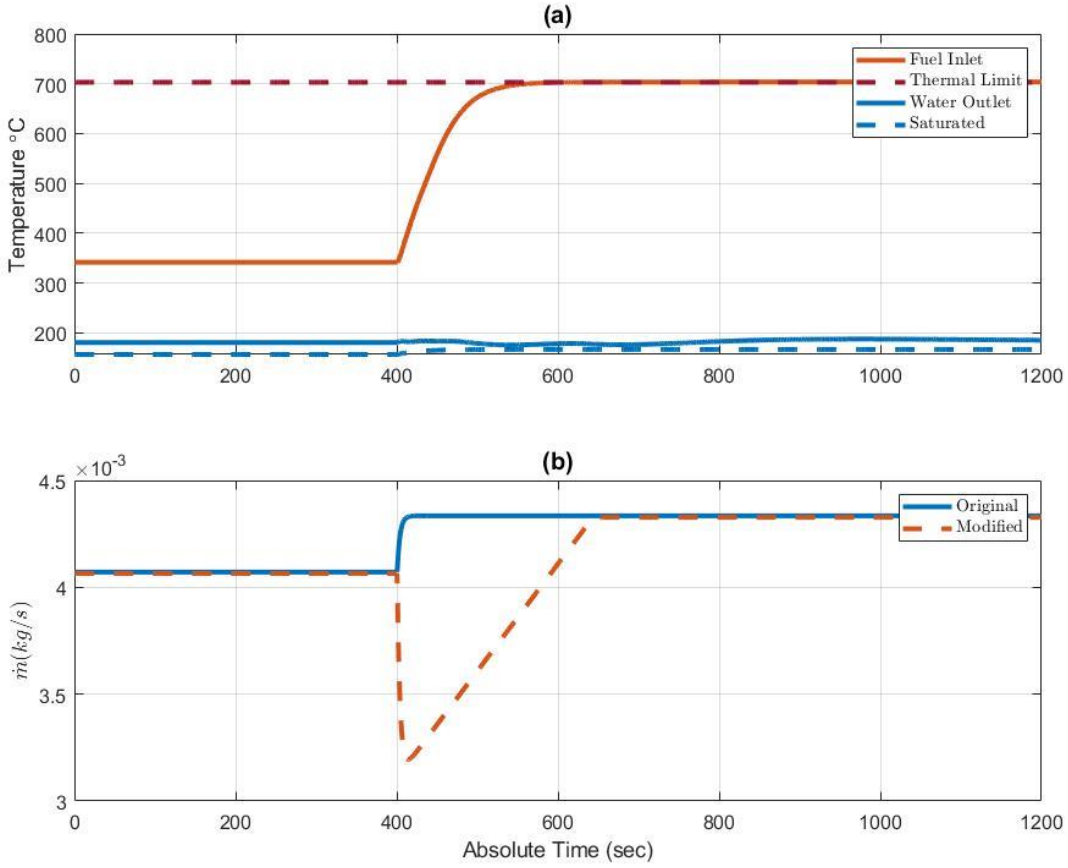

Figure 74: Evaporator inlet temperatures and thermal limits (a) water flow rates before and after modifications (b).

The water flow rates generated using steady state results failed to meet system requirements, resulting in subcooled water entering the scroll model. Therefore, modifications were made to produce consistent superheated steam. Using a parametric evaluation, it was determined that a step input, followed by a ramp function produced the desired steam quality, Figure 74 (b). From Figure 74 (a) this produced a steam temperature near the desirable limit of $180°C$, with a variation of $\pm 5\ °C$. This refined water flow rate was developed based on the analysis discussed above where initially heat transfer is significantly reduced but gradually increases until steady state is achieved. Therefore, the imposed water flow rate follows a similar trend, reduced significantly at the transition onset, and gradually increasing until about 640 seconds, Figure 74 (b). This offered a simplistic solution that agreed well with the analysis presented. This analysis coincides with the fact that steady state results alone are insufficient to optimize system inputs and transient performance must be examined to ensure all parameters are within system tolerances.

Through transient analysis the water flow rate was found to be insufficient for system operations; thus, the water flow rate was modified to ensure these requirements were met.

However, through basic steady state analysis power production was found to be insufficient and regardless of the system modifications performed these requirements could not be achieved using the given model. System performance is shown in Figure 75 (a) where scroll speed has been configured to maximize, power production during reduced-heating operations, and cooling capabilities during high-heating operations. This is discussed in more detail below.

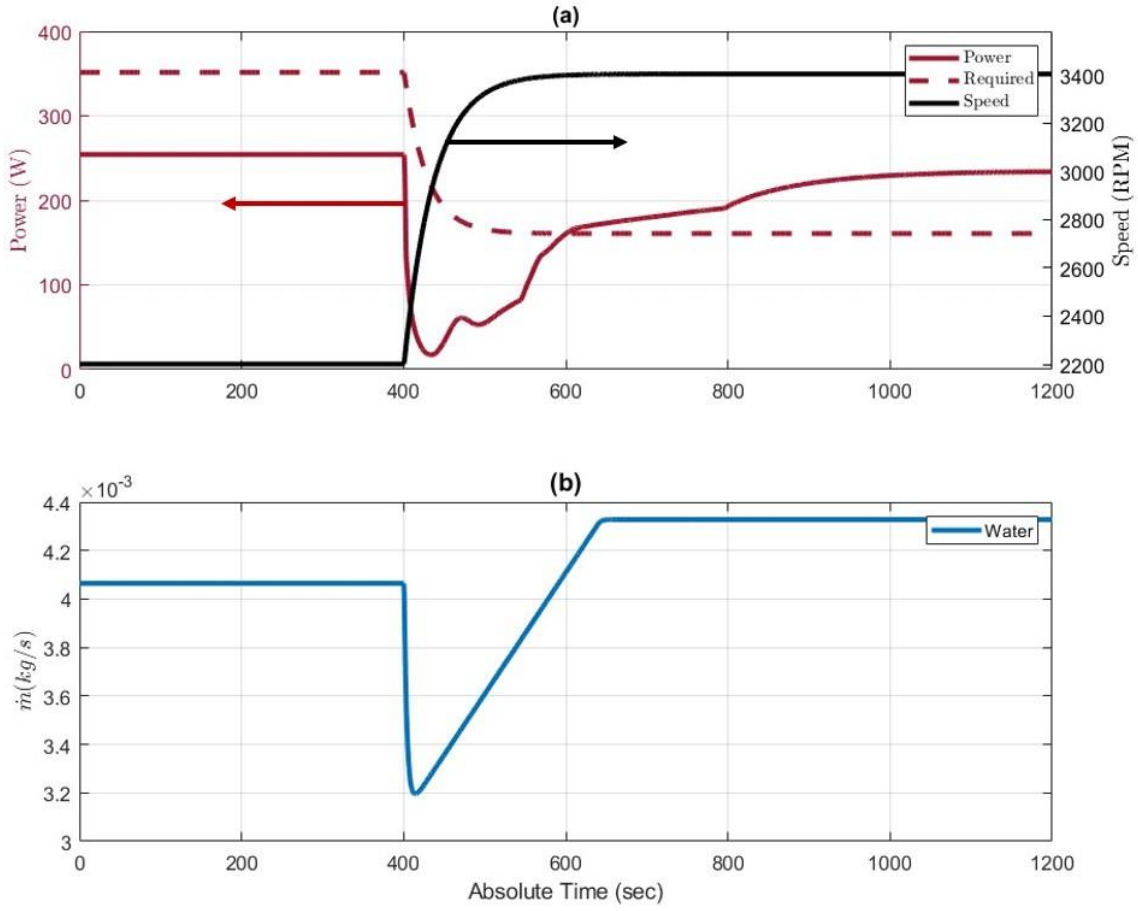

Figure 75: Scroll properties and power scaled requirements (a) and water flow rate (b)

As shown in Figure 75 (a), throughout the mission, scroll speed changes, more specifically it increases during the transition at 400 seconds. These speeds were tuned to meet the governing requirements, producing more power during the first segment of the mission and more cooling during the second segment. This takes advantage of scroll properties derived from experimental results discussed in Section 4.3 Scroll Modeling). Prior analysis determined that power production was insufficient at the high-heating mode; thus, scroll speed was set to 2200 RPM, producing maximum power. Despite this optimization, the power was still insufficient, shown in Figure 75 (a) from $0 \rightarrow 600$ seconds. This contributes to the notion that power requirements govern system design at the imposed high-heating configuration.

Two main “drivers” of steam production are fuel temperature and convective heating. With a substantial increase in fuel flow, fuel temperature drops, and the convection coefficient increases. However, it was determined that fuel temperature has a greater effect on heat transfer; thus, steam production and/or power generation is less during the high-heating operation. When heating is reduced, power production surpasses system requirements due to the very same reason, where a higher fuel temperature produces more steam. This coincides with the concept that there is less difficulty in meeting power requirements during reduced-heating situations. Unfortunately, a low fuel flow rate also reduces heat capacity; thus, the fuel thermal limit is reached during reduced-heating but not at the high-heating mode. Suggesting thermal requirements govern system when reduced-heating is investigated.

The capabilities of the Rankine cycle are measured based on system efficiencies, specifically the second law and thermal efficiencies, Table 7. With greater isentropic efficiency more energy can be extracted from the fluid, increasing overall cooling and the power generated, assuming the mechanical efficiency of the steam engine remains constant.

Table 7: Isentropic and thermal efficiencies of the system using a vehicle scaled evaluation.

Operation	η_{iso}	$\eta_{thermal}$
High-Heating	63.7	6.51
Reduced-Heating	68.8	8.92

$$\eta_{thermal} = \dot{W}_{net}/\dot{Q} \tag{89}$$

Shown by Eqn. 89 thermal efficiency is simply the ratio of the net mechanical work over the heat supplied to the fuel heat sink. Thus, thermal efficiency is directly related to the efficiency of the steam engine, specifically representing how much heat energy is converted into useful work. Performance is also related to the flight situation where there is greater thermal efficiency during the reduced-heating situation, Table 7. This is attributed to a higher fuel temperature “driving” steam production and leading to a higher power output. Scroll speed has been configured to maximize cooling capabilities during reduced-heating and maximize power production during high-heating. Thus, isentropic efficiency is higher to ensure maximum cooling through the scroll expander.

Power requirements are not met during high-heating despite the optimized scroll speed. However, this investigation was conducted using modeled components of the system, specifically the tube-in-tube evaporator and scroll expander. If different components were utilized power generation could be increased, possibly meeting vehicle requirements for all flight situations. Thus, it may be advantageous to characterize different heat exchangers and or steam engines that offer greater performance. In section 4.3.2 Corrugated-Plate Analysis), this

was performed where a corrugated plate evaporator was introduced into the system and a model was developed. Therefore, another vehicle scaled investigation can be conducted to reassess TMS performance. This research presents opportunities for future work.

The results from this analysis suggest power requirements govern system operations during the imposed high-heating condition and cooling requirements govern during at the reduced heating configuration. In fact, it was determined that during high-heating, power requirements were not met for the given model architecture. Thus, more efficient components should be incorporated to validate the system for aircraft applications. Additionally, it was determined that steam becomes saturated during the flight transition when configured purely based on steady state results. This indicates steady state analysis alone is insufficient for TMS design and system response must be observed to ensure ideal system operations and component reliability. It was also discerned that there are potential problems utilizing hydrocarbon fuel, specifically as the condensing medium. Methods were discussed to overcome these challenges, but components with a larger range and applicability would be needed to perform the required simulations for TMS validation. Lastly, the given examples show the benefit of employing the Rankine cycle system for a high-speed aircraft, high thermal loads enable the production of large quantities of steam removing heat from the vehicle while generating necessary power.

VI. Conclusion

Thermal based power systems offer advantages for high-speed applications due to the extreme heat loads available. Waste heat from the aircraft can be converted to electrical power with the dual benefit of removing heat. However, because thermal loads are very prominent, traditional thermal based power systems may be insufficient. As such, a dual mode Rankine cycle system is being investigated. Because this system incorporates two operational modes, system cooling can be enhanced making it particularly useful for a high-speed TMS. This research was both experimental and computational where results from the experimental system was used to develop component computational models which were utilized to analyze system performance.

Using steady state experimental results, critical system components were modeled using MATLAB Simulink software. These included single-phase and two-phase heat exchanger models based on the physical oil-cooler and evaporators. Performance of these components was based on steady state results where the oil cooler had the greatest accuracy with an RMS error of 0.8%. The corrugated plate evaporator had an RMSE of 1.0% and tube-in-tube evaporator had the greatest RMSE at 14.2%. Additionally, transient performance of the evaporators was assessed using a ramp response by changing the water flow rate. Results showed the modeled response led the experimental data for both designs, specifically, by 13.8% for the tube-in-tube evaporator and 82% for the corrugated plate evaporator. To

capture power capabilities, a scroll expander model was developed. Performance was assessed based on steady state results where power estimates resulted in an RMSE of 10.1% and a second law efficiency of 0.15%.

Using these components, a scaled integrated vehicle model was constructed assessing the TMS performance. This was performed for two different operational modes where scaled ratios defined model input parameters. The overall performance was assessed based on system efficiency. At high-heating operations, the system produced a thermal efficiency of 6.5% and a second law efficiency of 63.7%. During reduced-heating operations, the system produced a thermal efficiency of 8.9% and a second law efficiency of 68.8%. Additionally, through this investigation, key findings showed that power requirements define the system during high-heating operations and cooling requirements define the system at the reduced-heating operation. Thus, improving these components, specifically the evaporator and scroll expander models, will increase confidence in the scaled vehicle investigation, presenting a path for future efforts.

Developing component models with greater accuracy and range would increase confidence in the vehicle scaled model. This would require improvements and or modifications made to the experimental system. Such as, introducing a preheater to develop more accurate water-side convective correlations. This would isolate the two-phase and superheated steam within the evaporator producing more precise predictions for the individual phases. Additionally, higher water flow rates could be imposed to increase the range of the scroll model. This would require greater busbar amperage to produce higher rates of steam. Lastly, additional steady state points could be collected for all component models. This wouldn't extend the range of these models but would increase confidence in existing correlations and mapped parameters.

The previous recommendations are intended to improve accuracy of the individual components, increasing confidence in the vehicle scaled model. However, more work can still be accomplished using the current model. This includes incorporating the newly developed corrugated plate evaporator block. Due to its enhanced heat transfer, more steam is produced leading to greater power. These results may dismiss previous claims that power requirements are not met during high-heating situations. Additionally, various fuels can be evaluated, assessing their heat transfer characteristics as well as their heat sink capabilities, determining applicable fuels for the system. This capability of testing various system configurations is what led to the development of the vehicle scaled model. Backed by experimental results component interactions provide an accurate account of system performance that is used to validate the dual-mode Rankine cycle for high-speed applications.

References

1 Heppenheimer, T. A, “Facing the Heat Barrier: A History of Hypersonics” Washington D. C.: AIAA, 2007

2 Dirscherl, Kevin. “Hypersonic Speed Through Scramjet Technology”. University of Colorado at Boulder, Boulder, Colorado December 17, 2015

3 S. J. Scotti, C. J. Martin and S. H. Lucas, "Active Cooling Design for Scramjet Engines using Optimization Methods," NASA Langley Research Center, Hampton, VA, 1988.

4 J. Zuo, S. Zhang, J. Qin, W. Bao and N. Cui, "Performance evaluation of regenerative cooling/film cooling for hydrocarbon fueled scramjet engine," *Acta Astronautica,* vol. 148, pp. 57-68, 2018.

5 H. Li, J. Qin, Y. Jiang, D. Zhang, K. Cheng, W. Bao and H. Huang, "Experimental and theoretical investigation of power generation scheme driven by thermal cracked gaseous hydrocarbon fuel for hypersonic vehicle," *Energy and Conservation Management,* pp. 334-343, 2018.

6 V. S. Reddy, S. C. Kaushik, S. K. Tyagi and N. L. Panwar, "An Approach to Analyse Energy and Exergy Analysis of Thermal Power Plants: A Review," *Smart Grid and Renewable Energy,* vol. 1, 2010.

7 A. Desideri, B. Dechesne, J. Wronski, M. v. d. Broek, S. Gusev, V. Lemort and S. Quoilin, "Comparison of Moving Boundary and Finite-Volume Heat Exchanger Models in the Modelica Language," *Energies,* vol. 9, no. 339, 2016.

8 E. Rodriguez and B. Rasmussen, "A comparison of modeling paradigms for dynamic evaporator simulations with variable fluid phases," *Applied Thermal Engineering,* vol. 112, pp. 1326-1342, 2017.

9 Payne, Nathaniel “Development of a Combined Thermal Management and Power Generation System using a Multi-Mode Rankine Cycle”. Wright State University, Dayton, OH. 2021

10 Kays, W.M.,and A.L. London, Compact Heat Exchangers, 3rd ed., McGraw-Hill, New York, 1984

11 Incropera, Frank. DeWitt, David. “Fundamentals of Heat and Mass Transfer” 1996, *John Wiley and Sons*

12 Alahmad, Malik I. “Analysis of Heat Transfer in Two-Phase Two-Component Mixtures” King Saud University, Saudi Arabia 6/10/1991

13 Brkić, Dejan. “Can pipes be actually really that smooth?” *Hal Open Science.* September 13 2017.

14 Zhao, Houjian. Li, Xiaowei. “Friction factor and Nusselt number correlations for forced convection in helical tubes” *International Journal of Heat and Mass Transfer*. 2020

15 M.S. El-Genk , T.M. Schriener , A review and correlations for convection heat transfer and pressure losses in toroidal and helically coiled tubes, Heat Transf. Eng. 38 (5) (2017) 447–474 .

16 Seban, R.A., McLaughlint, E.F. “Heat Transfer in Tube Coils with Laminar and Turbulent Flow” International Heat Mass Transfer. Vol. 6, pp. 387-395. Pergamon Press 1963

17 Rennie, Timothy. Raghavan, Vijaya. “Numerical studies of a double-pipe helical heat exchanger” *Applied Thermal Engineering* 26 (2006) 1266–1273

18 Pritchard. J, Philip. “Fox and McDonald’s Introduction to Fluid Mechanics”. 8th Ed. John Wiley and Sons. 2011

19 *Liaqat, Nouman. Muhammad, Awan.* “EXPERIMENTAL VALIDATION OF PRANDTL NUMBER EXPONENT IN CORRELATION WITH NUSSELT NUMBER FOR DIFFERENT PLATE ORIENTATIONS OF THE SINGLE-PHASE FLOW PLATE HEAT EXCHANGER” July, 2018

20 Khartabil, Hussam “A Modified Wilson Plot Technique for Determining Heat Transfer Correlations” Ohio State University. 1987

21 Lee, Jonghyeok Lee, Kwan-Soo “Friction and Colburn factor correlations and shape optimization of chevron-type plate heat exchangers” 2014

22 Zheng, Dan Wang, Jin “Performance analysis of a plate heat exchanger using various nanofluids”. Elseveir. *International Journal of Heat and Mass Transfer* 158. 2020

23 Stodola, A. Lowenstein, L.C., “Steam and Gas Turbines”, McGraw-Hill, New York, 1927, Vol. 1, pp. 316

24 Cooke, David. “Modeling of Off-Design Multistage Turbine Pressures by Stodola’s Ellipse” Bechtel Power Corporation. Richmond, Virginia. 1983

25 Riccio, Aniello. Raimondo, Francesco. “Optimum design of ablative thermal protection systems for atmospheric entry vehicles” *Applied Thermal Engineering.* March 2017.

26 Zhang, Tiantian. Wang, Zhen-guo “A comparison of impulse performance among different engines” Elsevier. 2014

27 Zheng, Dan. Wang, Jin. “Performance Analysis of a Plate Heat Exchanger Using Various Nanofluids” *International Journal of Heat and Mass Transfer*. Sep. 2020

28 D. G. Bogard, "Airfoil Film Cooling," in *Gas Turbine Handbook*, 2007.

29 Xi, Huan. Li, Ming-Jia “Experimental studies of organic Rankine cycle systems using scroll expanders with different suction volumes”. *Applied Energy: Journal of cleaner production.* Jan. 2019

30 Ayachi, Fadhel. Ksayer, Elias. “Experimental investigation and modeling of a hermetic scroll expander”. *Applied Energy.* Aug. 2016

31 Emhardt, Simon. Tian, Guohong. “A review of scroll expander geometries and their performance”. *Applied Thermal Engineering.* Feb. 2018

32 Sanders, Bobby. Weir, Lois. “Highlights From a Mach 4 Experimental Demonstration of Inlet Mode Transition for Turbine-Based Combined Cycle Hypersonic Propulsion” National Aeronautics and Space Administration Glenn Research Center. Dec. 2012

33 D.R. Clarke, M. Oechsner, N.P. Padture, Thermal-barrier coatings for more efficient gas-turbine engines, MRS Bulletin. 2012

34 Krishna, Anand. “Thermal barrier coated surface modifications for gas turbine film cooling” *Journal of thermal analysis and Calorimetry.* July 2020. Available at: https://link.springer.com/article/10.1007/s10973-020-10032-2 (Accessed: March 10, 2023).

35 Bogard, D. G. Thole, K. A. “Gas turbine film cooling”. *Journal of propulsion and Power*. Dec. 2005 Available at: https://arc.aiaa.org/doi/abs/10.2514/1.18034 (Accessed: March 10, 2023).

36 Zhang, Silong. Qin, Jiang. “Numerical Analysis of Supersonic Film Cooling in Supersonic Flow in Hypersonic Inlet with Isolator”. February 2014. Available at: https://journals.sagepub.com/doi/abs/10.1155/2014/468790 (Accessed: March 12, 2023).

37 A. Ulas and E. Boysan, “Numerical analysis of regenerative cooling in liquid propellant rocket engines” *Aerospace Science and Technology*, November 2011, Available at: *https://www.sciencedirectcom.ezproxy.libraries.wright.edu/science/article/pii/S1270963811001 91X?via%3Dihub* (Accessed: March 12, 2023).

38 T. Myers, “The upper limit of specific impulse for various rocket fuels”, July 2016 Available at: https://thephysicsofspacex.files.wordpress.com/2016/07/isp-upper-limits.pdf (Accessed: March 12, 2023).

39 L. Marshall, C. Bahm, “Overview with Results and Lessons Learned of the X-43A Mach 10 Flight” American Institute of Aeronautics and Astronautics. June 2012 (Accessed: March 12, 2023).

40 Kethleen Zona. “Liquid Hydrogen--the Fuel of Choice for Space Exploration” July 2010. Available at: https://www.nasa.gov/topics/technology/hydrogen/hydrogen_fuel_of_choice.html (Accessed:March 29, 2023)

41 John D. Anderson, “Hypersonic and High-Gas Dynamics”, 2006 American Institute of Aeronautics and Astronautics

42 J.J. Killackey, E.A. Katinszky, “Thermal-Structural Design Study of an Airframe-Integrated Scramjet Final Report”, May 1980 NASA

43 T.A. Pimenta, J.B.L.M. Campos, “Heat transfer coefficients from Newtonian and non-Newtonian fluids flowing in laminar regime in a helical coil”, October 2012, *International Journal of Heat and Mass Transfer*

44 “Determining the time constant of an RC circuit” Summer 2014, Rose-Hulman Institute of Technology, Available at: https://www.rose-hulman.edu/ES205/PDFs/s12_lab_5.pdf (Accessed: March 10, 2023)

45 “Brazed plate and Gasketed Heat Exchangers” 2017, Xylem Inc., Dublin, Available at: https://www.xylem.com/siteassets/brand/lowara/resources/brochure/lowara-heat-exchangers_uk_en.pdf (Accessed: March 12, 2023)

46 Roberts, Kristen. “ANALYSIS AND DESIGN OF A HYPERSONIC SCRAMJET ENGINE WITH A STARTING MACH NUMBER OF 4.00”, The University of Texas at Arlington, 2008, Available at: https://arc.uta.edu/publications/td_files/Kristen%20Roberts%20MS.pdf (Accessed: May 23, 2023)

47 S. D. Kasen, "Thermal Management at Hypersonic Leading Edges," *University of Virginia,* 2013.

48 Siddiqi, Asif A. Beyond Earth: A Chronicle of Deep Space Exploration, 1958-2016. NASA History Program Office, 2018.

Appendix A

Temperature (K)	Density (kg/m^3)	Specific Heat Capacity	Thermal Conductivity
20	878	1.82	0.1155
30	872	1.86	0.1148
40	866	1.91	0.1141
50	859	1.96	0.1133
60	853	2.00	0.1125
70	847	2.05	0.1118
80	840	2.10	0.1109
90	834	2.14	0.1101
100	827	2.18	0.1093
110	821	2.23	0.1084
120	814	2.27	0.1075
130	808	2.31	0.1065
140	801	2.36	0.1056
150	795	2.40	0.1046
160	788	2.44	0.1036
170	782	2.48	0.1025
180	775	2.52	0.1015
190	768	2.56	0.1004
200	731	2.60	0.0993
210	755	2.63	0.0982
220	748	2.67	0.0970
230	741	2.71	0.0959
240	734	2.75	0.0947
250	727	2.78	0.0934
260	720	2.82	0.0922
270	712	2.85	0.0909
280	705	2.89	0.0896
290	698	2.92	0.0883
300	690	2.95	0.0869
310	682	2.99	0.0856
320	675	3.02	0.0842
330	667	3.05	0.0828

Appendix B

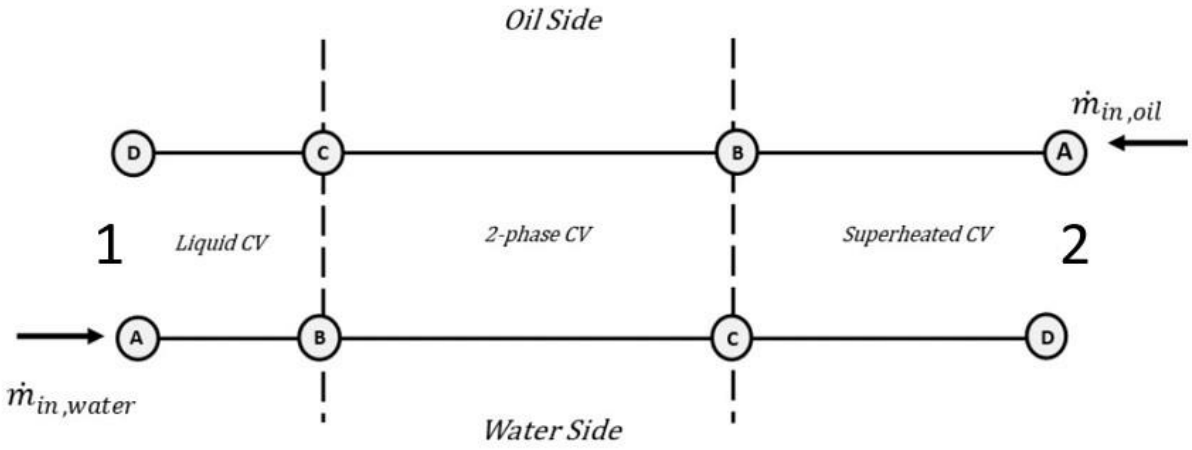

Subcooled Liquid Control Volume

Predict $T_{oil,D}$

With

$$T_{oil,D} < T_{oil,A} - \frac{\dot{Q}_{sl} + \dot{Q}_{2p}}{C_{oil}}$$

$$\dot{Q}_{sl} = C_{water}\left(T_{water,A} - T_{water,B}\right)$$

$$\dot{Q}_{2p} = \dot{m}_{water} h_{fg}$$

$$C_{water} = \dot{m}_{water} C_{p,water}$$

$$C_{oil} = \dot{m}_{oil} C_{p,oil}$$

$$C_{min} = \min(C_{oil}, C_{water})$$

$$Q_{max,sl} = C_{min}\left(T_{oil,C} - T_{water,A}\right)$$

$$\varepsilon_{sl} = \frac{\dot{Q}_{sl}}{Q_{max,sl}}$$

$$\mathrm{NTU_{sl}} = \frac{1}{C_r - 1} \ln\left(\frac{\varepsilon_{sl} - 1}{\varepsilon_{sl} C_r - 1}\right)$$

$$\frac{\mathrm{NTU_{sl}} C_{min}}{\pi D U_{sl}} = \mathrm{L_{sl}}$$

Two-Phase Control Volume

$$T_{oil,C} = \frac{\dot{Q}_{sl} + \dot{Q}_{loss,CD}}{C_{oil}} + T_{oil,D}$$

$$Q_{max,2p} = C_{min}\left(T_{oil,B} - T_{water,B}\right)$$

$$\varepsilon_{2p} = \frac{\dot{Q}_{2p}}{Q_{max,2p}}$$

$$\mathrm{NTU}_{2p} = \frac{1}{C_r - 1}\ln\left(\frac{\varepsilon_{2p} - 1}{\varepsilon_{2p} C_r - 1}\right)$$

$$\frac{\mathrm{NTU_{2p}} C_{min}}{\mathrm{U_{2p}}\pi \mathrm{D}} = \mathrm{L}_{2p}$$

$$T_{oil,B} = \frac{\dot{Q}_{2p} + \dot{Q}_{loss,BC}}{C_{oil}} + T_{oil,C}$$

Superheated Control Volume

$$\dot{Q}_{sh} = \dot{Q}_{oil,AB} - \dot{Q}_{loss,AB}$$

$$T_{water,D} = T_{sv} + \frac{\dot{Q}_{sh}}{C_{water,sh}}$$

$$Q_{max,sh} = C_{min}\left(T_{oil,A} - T_{water,C}\right)$$

$$\varepsilon_{2p} = \frac{\dot{Q}_{sh}}{Q_{max,sh}}$$

$$\mathrm{NTU}_{sh} = \frac{1}{C_r - 1}\ln\left(\frac{\varepsilon_{sh} - 1}{\varepsilon_{sh} C_r - 1}\right)$$

$$\frac{\mathrm{NTU}_{sh} C_{min}}{\mathrm{U}_{sh}\pi \mathrm{D}} = \mathrm{L}_{sh}$$

Does

$$L_{sl} + L_{2p} + L_{sh} = L$$

If not, repeat the process.

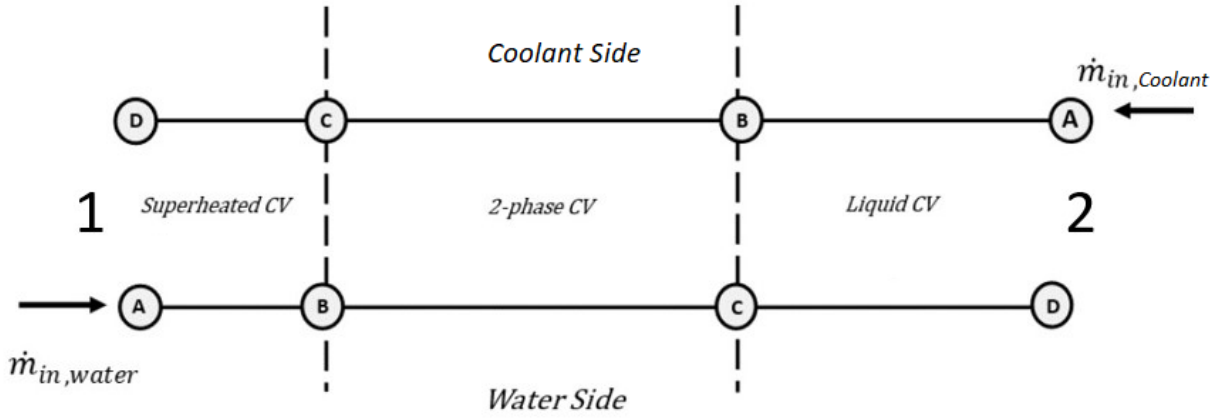

Superheated Control Volume

Predict $T_{cool,D}$

With

$$T_{cool,D} < T_{cool,A} + \frac{\dot{Q}_{sh} + \dot{Q}_{2p}}{C_{cool}}$$

$$\dot{Q}_{sh} = C_{water}\left(T_{water,A} - T_{water,B}\right)$$

$$\dot{Q}_{2p} = \dot{m}_{water} h_{fg}$$

$$C_{water} = \dot{m}_{water} C_{p,water}$$

$$C_{cool} = \dot{m}_{cool} C_{p,cool}$$

$$C_{min} = \min(C_{cool}, C_{water})$$

$$T_{cool,C} = T_{cool,D} - \frac{\dot{Q}_{sh} + \dot{Q}_{gain,CD}}{C_{cool}}$$

$$Q_{max,sh} = C_{min}\left(T_{water,A} - T_{cool,C}\right)$$

$$\varepsilon_{sh} = \frac{\dot{Q}_{sh}}{Q_{max,sh}}$$

$$\mathrm{NTU}_{sh} = \frac{1}{C_r - 1} \ln\left(\frac{\varepsilon_{sh} - 1}{\varepsilon_{sh} C_r - 1}\right)$$

$$\frac{\mathrm{NTU}_{\mathrm{sh}} C_{min}}{\pi D U_{sh}} = \mathrm{L}_{\mathrm{sh}}$$

Two-Phase Control Volume

$$Q_{max,2p} = C_{min}\left(T_{water,B} - T_{cool,B}\right)$$

$$\varepsilon_{2p} = \frac{\dot{Q}_{2p}}{Q_{max,2p}}$$

$$\mathrm{NTU}_{2p} = \frac{1}{C_r - 1}\ln\left(\frac{\varepsilon_{2p} - 1}{\varepsilon_{2p} C_r - 1}\right)$$

$$\frac{\mathrm{NTU}_{2p} C_{min}}{\mathrm{U}_{2p}\pi\mathrm{D}} = \mathrm{L}_{2p}$$

Subcooled Liquid Control Volume

$$T_{cool,B} = T_{cool,C} - \frac{\dot{Q}_{2p} + \dot{Q}_{gain,BC}}{C_{cool}}$$

$$\dot{Q}_{sl} = \dot{Q}_{cool,AB} - \dot{Q}_{gain,AB}$$

$$T_{water,D} = T_{water,C} - \frac{\dot{Q}_{sl}}{C_{water}}$$

$$Q_{max,sl} = C_{min}\left(T_{water,C} - T_{cool,A}\right)$$

$$\varepsilon_{2p} = \frac{\dot{Q}_{sh}}{Q_{max,sh}}$$

$$\mathrm{NTU}_{sh} = \frac{1}{C_r - 1}\ln\left(\frac{\varepsilon_{sh} - 1}{\varepsilon_{sh} C_r - 1}\right)$$

$$\frac{\mathrm{NTU}_{sh} C_{min}}{\mathrm{U}_{sh}\pi\mathrm{D}} = \mathrm{L}_{sh}$$

Does

$$L_{sl} + L_{2p} + L_{sh} = L$$

If not, repeat the process.

Appendix C

Scroll Performance Data from Manufacture

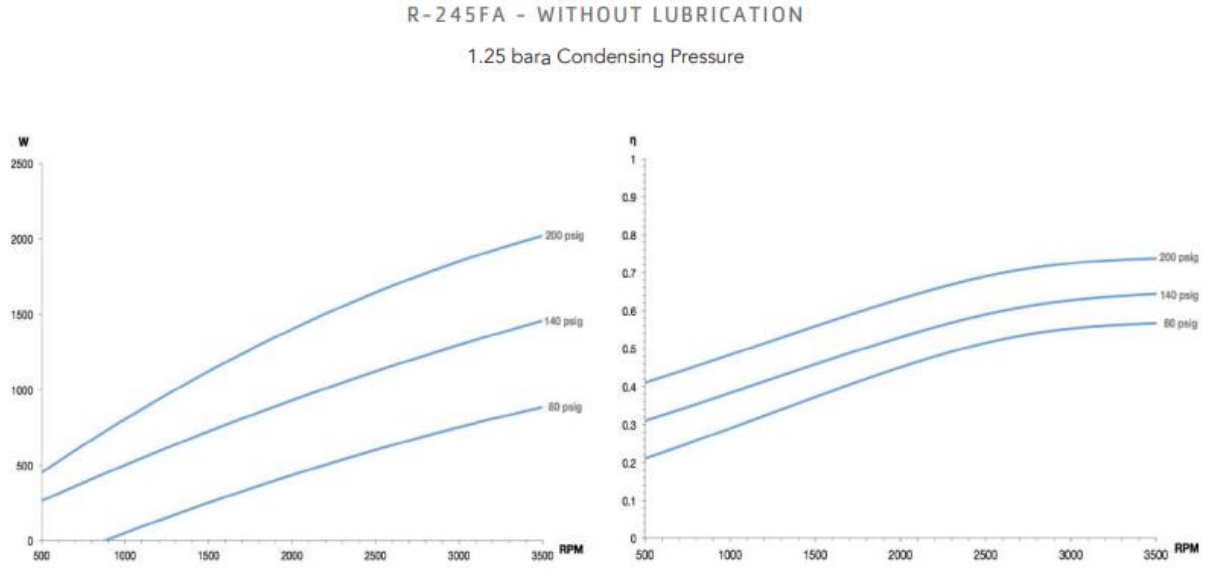

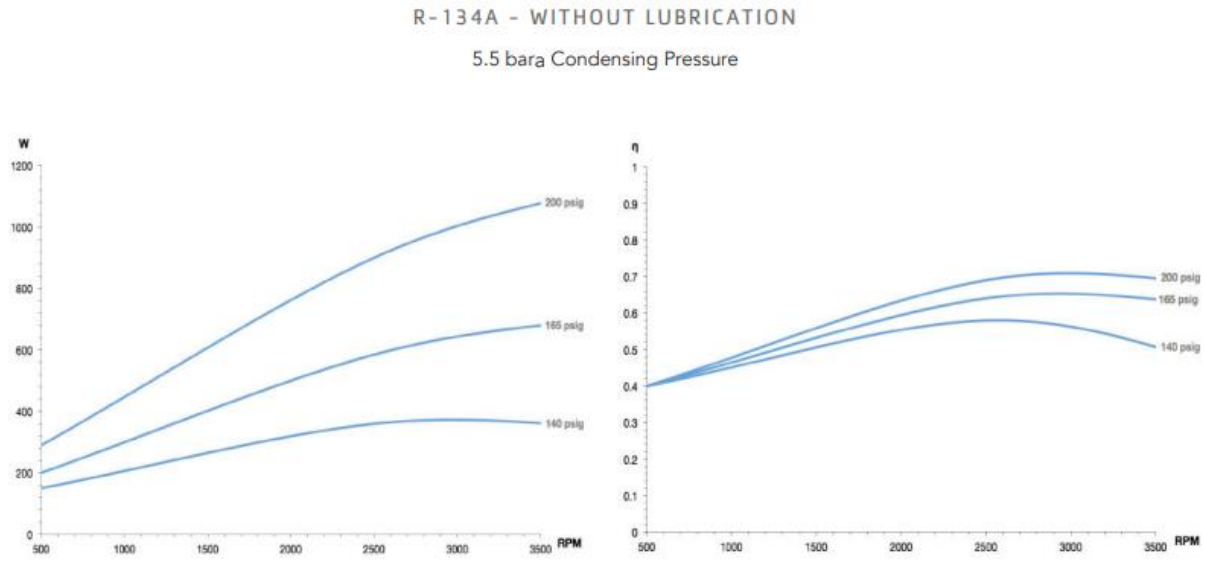

Appendix D

Uncertainty Analysis for Overall Resistance

$$R_{ov} = R_h + R_w + R_c = \frac{\Delta T_{\mathrm{lm}}}{\dot{Q}}$$

$$\Delta T_{\mathrm{lm}} = \frac{(T_{h,in} - T_{c,out}) - (T_{h,out} - T_{c,in})}{\ln\left(\frac{T_{h,in} - T_{c,out}}{T_{h,out} - T_{c,in}}\right)}$$

Here the subscripts h represents the hot side (oil side) of the heat exchanger and c represents the cold side (water side) of the heat exchanger.

$$\dot{Q} = \dot{m}_h C_{p,h}(T_{h,in} - T_{h,out})$$

The thermal resistance of the hot side is an order of magnitude greater than the cold side; thus,

$$R_{ov} \approx R_h + R_w$$

and the uncertainty in R_{ov} is used to quantify the uncertainty in $R_h + R_w$.

$$\sigma_\phi = \sqrt{\frac{1}{N-1}\sum_{i=1}^{N}(\phi_i - \bar{\phi})^2}$$

The variable ϕ represents all independent variables, with attributed random error, used to calculate R_{ov} (i.e., $T_{h,in}, T_{h,out}, T_{c,in}, T_{c,out}$ and $\dot{m}$)

$$S_{P,\phi} = \frac{\sigma_\phi}{\sqrt{N}}$$

$$S_{B,\phi} = \frac{1}{t_{v,c}} u(\phi)$$

It is assumed instrumental uncertainty (systematic error) was quantified with a confidence $c = 95\%$ and degrees of freedom $v_B > 30$; thus, $t_{v,c} \approx 2$.

$$B_{\Delta T_{\mathrm{lm}}} = t_{v,c}\sqrt{\left[\frac{\partial \Delta T_{\mathrm{lm}}}{\partial T_{h_{in}}} S_{B,T_{h_{in}}}\right]^2 + \left[\frac{\partial \Delta T_{\mathrm{lm}}}{\partial T_{h_{out}}} S_{B,T_{h_{out}}}\right]^2 + \left[\frac{\partial \Delta T_{\mathrm{lm}}}{\partial T_{c_{in}}} S_{B,T_{c_{in}}}\right]^2 + \left[\frac{\partial \Delta T_{\mathrm{lm}}}{\partial T_{c_{out}}} S_{B,T_{c_{out}}}\right]^2}$$

$$P_{\Delta T_{\mathrm{lm}}} = t_{v,c}\sqrt{\left[\frac{\partial \Delta T_{\mathrm{lm}}}{\partial T_{h_{in}}} S_{P,T_{h_{in}}}\right]^2 + \left[\frac{\partial \Delta T_{\mathrm{lm}}}{\partial T_{h_{out}}} S_{P,T_{h_{out}}}\right]^2 + \left[\frac{\partial \Delta T_{\mathrm{lm}}}{\partial T_{c_{in}}} S_{P,T_{c_{in}}}\right]^2 + \left[\frac{\partial \Delta T_{\mathrm{lm}}}{\partial T_{c_{out}}} S_{P,T_{c_{out}}}\right]^2}$$

Assuming the degrees of freedom for both systematic and random errors are large (i.e., $v_B > 30$ and $v_P > 30$) the student-t value is again approximated with $t_{v,c} \approx 2$.

$$u(\Delta T_{\mathrm{lm}}) = \sqrt{B_{\Delta T_{\mathrm{lm}}}^2 + P_{\Delta T_{\mathrm{lm}}}^2}$$

$$B_{\dot{Q}} = t_{v,c}\sqrt{\left[\frac{\partial \dot{Q}}{\partial \dot{m}} S_{B,\dot{m}}\right]^2 + \left[\frac{\partial \dot{Q}}{\partial T_{h,in}} S_{B,T_{h,in}}\right]^2 + \left[\frac{\partial \dot{Q}}{\partial T_{h,out}} S_{B,T_{h,out}}\right]^2}$$

$$P_{\dot{Q}} = t_{v,c}\sqrt{\left[\frac{\partial \dot{Q}}{\partial \dot{m}} S_{P,\dot{m}}\right]^2 + \left[\frac{\partial \dot{Q}}{\partial T_{h,in}} S_{P,T_{h,in}}\right]^2 + \left[\frac{\partial \dot{Q}}{\partial T_{h,out}} S_{P,T_{h,out}}\right]^2}$$

$$u(\dot{Q}) = \sqrt{B_{\dot{Q}}^2 + P_{\dot{Q}}^2}$$

$$\boldsymbol{u(R_{ov})} = \sqrt{u(\dot{Q})^2 + u(\Delta T_{\mathrm{lm}})^2}$$

Uncertainty Analysis for Isentropic Efficiency

$$\eta_{iso} = \frac{h_1 - h_2}{h_1 - h_{2,s}}$$

$$h_1, h_2 = f(p, T)$$

Enthalpy at the inlet and outlet is dependent on the fluid state determined using pressure and temperature readings. Uncertainties in these predictions create quantifiable uncertainty in enthalpy.

$$h_{2,s} = f(s_1, p_2)$$

$$s_{in} = f(p_1, T_1)$$

Isentropic enthalpy, $h_{2,s}$, is dependent on fluid properties at the inlet and exit; thus, uncertainty in $h_{2,s}$ will be attributed to these properties (i.e., $p_1, T_1, \text{and } p_2$).

$$S_{P,\varphi} = \frac{\sigma_\varphi}{\sqrt{N}}$$

Random error is only attributed to pressure and temperature; thus, the place holder variable, φ represents pressure, p and temperature, T.

$$P_\varphi = t_{v,c} S_{B,\varphi}$$

It is assumed instrumental error was calculated with a confidence $c = 95\%$ and degrees of freedom $v_B > 30$; thus, $t_{v,c} \approx 2$ and

$$B_\varphi = u_\varphi$$

$$u(\varphi) = \sqrt{B_\varphi^2 + P_\varphi^2}$$

$$u(h_1) = \sqrt{\left[\frac{\partial h_1}{\partial p} u(p_1)\right]^2 + \left[\frac{\partial h_1}{\partial T} u(T_1)\right]^2}$$

$$u(h_2) = \sqrt{\left[\frac{\partial h_2}{\partial p}u(p_2)\right]^2 + \left[\frac{\partial h_2}{\partial T}u(T_2)\right]^2}$$

$$u(h_{2,s}) = \sqrt{\left[\frac{\partial h_{2,s}}{\partial s}u(s_1)\right]^2 + \left[\frac{\partial h_{2,s}}{\partial p}u(p_2)\right]^2}$$

$$u(s_1) = \sqrt{\left[\frac{\partial s}{\partial p}u(p_1)\right]^2 + \left[\frac{\partial s}{\partial T}u(T_1)\right]^2}$$

All sensitivity coefficient (i.e., $\frac{\partial h_1}{\partial p}, \frac{\partial h_1}{\partial T}, \frac{\partial h_2}{\partial p}, \frac{\partial h_2}{\partial T}, \frac{\partial s}{\partial p}$ and $\frac{\partial s}{\partial T}$) were calculated used steam NBS tables.

$$\boldsymbol{u(\eta_{iso})} = \sqrt{\left[\frac{\partial \eta_{iso}}{\partial h_1}u(h_1)\right]^2 + \left[\frac{\partial \eta_{iso}}{\partial h_2}u(h_2)\right]^2 + \left[\frac{\partial \eta_{iso}}{\partial h_{2,s}}u(h_{2,s})\right]^2}$$

Uncertainty Analysis for Shaft Work (Power Output) and Mechanical Efficiency

$$\eta_{mech} = \frac{\dot{W}_s}{\dot{Q}}$$

$$\dot{W}_s = \omega L F_s$$

$$\dot{Q} = \dot{m}(h_2 - h_1)$$

$$S_{P,\varphi} = \frac{\sigma_\varphi}{\sqrt{N}}$$

Random error is only attributed to pressure and temperature; thus, the place holder variable, $\varphi = p$ and T.

$$P_\varphi = t_{v,c} S_{B,\varphi}$$

It is assumed quantization of the instrumental error utilized a confidence $c = 95\%$ and degrees of freedom $v_B > 30$; thus, $t_{v,c} \approx 2$ and

$$B_\varphi = u_\varphi$$

$$u(\varphi) = \sqrt{B_\varphi^2 + P_\varphi^2}$$

$$u(h_1) = \sqrt{\left[\frac{\partial h_1}{\partial p}u(p_1)\right]^2 + \left[\frac{\partial h_1}{\partial T}u(T_1)\right]^2}$$

$$u(h_2) = \sqrt{\left[\frac{\partial h_2}{\partial p} u(p_2)\right]^2 + \left[\frac{\partial h_2}{\partial T} u(T_2)\right]^2}$$

$$P_{F_s} = t_{c,v} S_{P,F}$$

$$B_{F_s} = U_{F_s}$$

Here U_{F_s} is the provided systematic uncertainty of the load cell. Uncertainty in the lever arm length, L and angular velocity, ω was not included.

$$u(F_s) = \sqrt{B_{F_s}^2 + P_{F_s}^2}$$

$$\boldsymbol{u(\dot{W}_s)} = \sqrt{\frac{\partial \dot{W}_s}{\partial F_s} u(F_s) + \frac{\partial \dot{W}_s}{\partial h_1} u(h_1) + \frac{\partial \dot{W}_s}{\partial h_2} u(h_2)}$$

$$\boldsymbol{u(\eta_{mech})} = \sqrt{\left[\frac{\partial \eta_{mech}}{\partial \dot{W}_s} u(\dot{W}_s)\right]^2 + \left[\frac{\partial \eta_{mech}}{\partial \dot{Q}} u(\dot{Q})\right]^2}$$